

POLITECNICO DI TORINO
Master's Degree in Civil Engineering

Structural Health Monitoring using low cost sensors: experimental and numerical study

Master's Thesis
October 2018



Supervisor:
Prof. Francesco Tondolo

Co-supervisor:
Prof. Donato Sabia

Candidate:
Francesco Nerio Battistoni

Table of contents

Abstract	1
Riassunto	3
Introduction	5
1. Smart technologies in Structural Health Monitoring	7
1.1 Monitoring in Civil Engineering	7
1.2 Importance of SHM.....	8
1.3 Conventional monitoring systems for concrete structures	10
1.4 Conventional strain measurement system: Metallic Strain Gauge.....	11
1.4.1 Quarter-Bridge Strain Gauge	13
1.4.2 Half-Bridge Strain Gauge	14
1.4.3 Full-Bridge Strain Gauge	15
1.5 Innovative strain monitoring systems.....	16
1.5.1 Passive Wireless RFID Strain Sensors	16
1.5.2 Passive Wireless Strain Sensors with Magnetoelastic Beam Elements ..	17
1.5.3 Skin-like sensors	18
1.5.4 Wireless Smart Sensors platform.....	19
1.5.5 Frictional strain gage in WSS platform.....	20
1.5.6 Strain-sensing antenna	21
1.6 Innovative strain monitoring system: Fibre Optic.....	22
1.6.1 Fibre Bragg Grating Sensor (FBGS).....	23
1.6.2 Distributed Fibre Optic Strain (FOS) sensors.....	25
1.6.3 Fabry-Perot cavities sensors.....	28
1.6.4 Multicore Fibre (MCF) based on helical structures.....	29
1.7 Innovative strain monitoring technology: S3 system	30
2. Numerical study	33
2.1 Parametric generation of 3D elements.....	34
2.2 Constitutive Law of B450C steel.....	36

2.3 Whole Steel Bar F.E.M. model.....	38
2.3.1 Model definition.....	38
2.3.2 Deformed shape	40
2.3.3 Constitutive law and FEM model behaviour	42
2.4 One-eighth of Smart Steel Bar FEM model.....	43
2.4.1 Cavity geometry	43
2.4.2 Steel bar definition	46
2.4.3 Air cavity definition	47
2.4.4 Complete model definition.....	49
2.4.5 Deformed shape	49
2.4.6 Pressure-Volume in-depth analysis	51
2.5 One-quarter of Smart Steel Bar FEM model.....	53
2.5.1 Steel bar definition	54
2.5.2 Air cavity definition	56
2.5.3 Complete model definition.....	57
2.5.4 Deformed shape	57
3. Comparison with previous studies	61
3.1 Previous experimental campaign on S3 system.....	61
3.1.1 Theoretical basis.....	61
3.1.2 Thermal calibration tests.....	62
3.1.3 Axial tensile tests	63
3.1.4 Axial tensile test until rupture	65
3.2 Comparison with numerical results.....	68
3.2.1 Models description.....	68
3.2.2 Force-Displacement relations comparison.....	69
3.2.3 Force-Deformation relations comparison	72
4. Experimental study	79
4.1 Instrumented bars tensile test	79
4.1.1 Axial tensile test staging	79
4.1.2 Sensors numeration and CB settings	81

4.1.3 Load path applied	82
4.2 The 4-point bending test	84
4.2.1 Strain gages installation	85
4.2.2 Reinforcement cage realisation	88
4.2.3 Instrumented reinforcement bars assembly	89
4.3.4 Strain gages and sensors numeration.....	93
4.3.5 Concrete mix design	94
4.3.6 Concrete mechanical characterisation	98
4.3.7 Bending test staging.....	99
4.3.8 Expected moment-curvature behaviour.....	104
4.3.9 Load cases	107
4.3.10 Crack pattern	109
4.3.11 Results and discussion	113
Conclusions	123
Bibliography.....	125

List of Figures

Fig. 1: List of non-destructive techniques for concrete structures monitoring.....	11
Fig. 2: HBM Strain Gauge 1-LY41-6/120.....	12
Fig. 3: Wheatstone Bridge circuit.....	12
Fig. 4: Quarter-Bridge Strain Gauge configuration Type 1.....	13
Fig. 5: Quarter-Bridge Strain Gauge configuration Type 2.....	14
Fig. 6: Half-Bridge Strain Gauge configuration Types.....	15
Fig. 7: Full-Bridge Strain Gauge configuration Types.....	16
Fig. 8: RFID Strain Sensor configuration.....	17
Fig. 9: Wireless Passive Strain Sensor configuration.....	18
Fig. 10: Skin-like sensor configuration.....	19
Fig. 11: Xnode platform linked to WSS.....	20
Fig. 12: Xnode platform operation.....	20
Fig. 13: Frictional Strain Gauge with a cylindrical magnet.....	21
Fig. 14: Strain sensing antenna operation.....	22
Fig. 15: Bragg wavelength shift in FBG Sensor.....	23
Fig. 16: Fibre Bragg Grating Sensors interrogation and acquisition system.....	24
Fig. 17: BOTDR configuration (Galindez-Jamioy, 2012).....	26
Fig. 18: BOTDA configuration (Galindez-Jamioy, 2012).....	27
Fig. 19: Strain transducer.....	29
Fig. 20: Multicore Fibre Optic operation.....	29
Fig. 21: Longitudinal section of the smart steel bar.....	30
Fig. 22: 8-nodes 3D elements.....	34
Fig. 23: 6-nodes 3D element.....	35
Fig. 24: 4-nodes 3D element.....	35
Fig. 25: Engineering stress-strain B450C.....	36
Fig. 26: True stress-strain B450C.....	38
Fig. 27: Whole steel bar geometry.....	39
Fig. 28: Whole steel bar - applied displacement.....	40
Fig. 29: Deformed whole steel bar axonometric projection.....	41
Fig. 30: Deformed whole steel bar orthogonal projection (XY).....	41
Fig. 31: Deformed whole steel bar orthogonal projection (XZ).....	41
Fig. 32: Constitutive law and FEM behaviour.....	42
Fig. 33: Constitutive law and FEM behaviour - focus on elastic branch.....	43
Fig. 34: $\Phi 20$ Smart Steel Bar 10 cm long.....	44
Fig. 35: Half of $\Phi 20$ Smart Steel Bar.....	45

Fig. 36: An eighth of $\Phi 20$ Smart Steel Bar (lower part).....	45
Fig. 37: One-eighth steel bar (EG1) geometry.....	46
Fig. 38: One-eighth steel bar (EG1) geometry - detail	47
Fig. 39: One-eighth steel bar (complete model) geometry - detail.....	48
Fig. 40: One-eighth steel bar (complete model) geometry	48
Fig. 41: One-eighth steel bar - applied displacement.....	49
Fig. 42: Deformed one-eighth steel bar (EG1) axonometric projection.....	50
Fig. 43: Deformed one-eighth steel bar (EG1) orthogonal projection (XY)	50
Fig. 44: Deformed one-eighth steel bar (EG1) orthogonal projection (XZ)	50
Fig. 45: Deformed one-eighth air volume (EG2) axonometric projection.....	51
Fig. 46: One-eighth steel bar (case a) - air cavity pressure (last time step)	52
Fig. 47: One-eighth steel bar (case b) - air cavity pressure (last time step)	53
Fig. 48: A quarter of $\Phi 20$ Smart Steel Bar.....	54
Fig. 49: One-quarter steel bar (EG1) geometry.....	55
Fig. 50: One-quarter steel bar (EG1) geometry - detail.....	55
Fig. 51: One-quarter steel bar (complete model) geometry - detail	56
Fig. 52: One-quarter steel bar - applied displacement	57
Fig. 53: Deformed one-quarter steel bar (EG1) axonometric projection	58
Fig. 54: Deformed one-quarter steel bar (EG1) orthogonal projection (XZ).....	58
Fig. 55: Deformed one-quarter steel bar (EG1) orthogonal projection (XY)	59
Fig. 56: Deformed one-quarter steel bar (EG1) axonometric projection - detail...59	
Fig. 57: Deformed one-quarter air volume (EG2) axonometric projection.....	60
Fig. 58: Thermal compensation: determination of the $f(\cdot)$ relation between ΔT^* and $(\Delta V/V_0)\Delta T^*$, through fitting the experimental data obtained in a temperature controlled environment, for the three sensors	63
Fig. 59: Axial load test: (a) applied force; (b) measured pressure; (c) measured temperature; (d) reconstructed force-dependent volume variation	64
Fig. 60: Axial load test: (e) volume-to-force calibration for sensor S1; (f) volume-to-force calibration for sensor S2; (g) volume-to-force calibration for sensor S3; (h) applied v estimated force	65
Fig. 61: Monotonic tensile test until rupture: force-displacement relations for the three displacement transducers	66
Fig. 62: Monotonic tensile test until rupture: (a) measured pressure; (b) measured temperature; (c) reconstructed force-dependent volume; (d) applied v estimated force	67
Fig. 63: Monotonic tensile test until rupture: experimental correlations between cavity volume variations and applied force	67
Fig. 64: Force-Displacement comparison	69

Fig. 65: Force-Displacement comparison - focus on first models.....	70
Fig. 66: Force-Displacement comparison - focus on elastic branch	71
Fig. 67: Force-Deformation comparison.....	73
Fig. 68: Force-Deformation comparison - focus on first models	74
Fig. 69: Force-Deformation comparison - focus on elastic branch.....	75
Fig. 70: Force-Deformation comparison - 8 mm ³ n.d.	76
Fig. 71: Force-Deformation comparison - 8 mm ³ n.d. - focus on first models	77
Fig. 72: Force-Deformation comparison - 8 mm ³ n.d. - focus on elastic branch...	77
Fig. 73: Axial tensile test scheme	80
Fig. 74: Axial tensile test configuration (a) and a zoomed view (b)	81
Fig. 75: S3 system numeration: bars from B1 to B5 from figures (a) to (e).....	82
Fig. 76: Time history of applied load.....	82
Fig. 77: Mechanical calibration test for the S2 unit: (a) applied force; (b) measured pressure; (c) measured temperature; (d) reconstructed force-dependent volume variation; (e) volume-to-force calibration; (f) applied v estimated force (Tondolo, 2018)	84
Fig. 78: Longitudinal profile of the RC beam	85
Fig. 79: Transversal section of the RC beam.....	85
Fig. 80: S3 sensors and strain gauges placement in bar B2.....	86
Fig. 81: Sanding off bar's surface.....	87
Fig. 82: Strain gauges glued to bar's surface	87
Fig. 83: Strain gauges final configuration	88
Fig. 84: Reinforcement cage's longitudinal profile	88
Fig. 85: Steel reinforcement's transversal section.....	89
Fig. 86: Reinforcement cage.....	89
Fig. 87: Instrumented reinforcement longitudinal profile.....	90
Fig. 88: Steel bars bending	91
Fig. 89: Reinforcement cage assembled with instrumented reinforcement	91
Fig. 90: Cables organisation and numeration.....	92
Fig. 91: Formworks assembly	92
Fig. 92: Reinforcement placed inside the formworks for Beam1 and Beam2.....	93
Fig. 93: Beam1 (a) and Beam2 (b) measurement units numeration	94
Fig. 94: Granulometric curve for mix design.....	95
Fig. 95: Concrete poured in the formworks for Beam1 and Beam2	97
Fig. 96: Cylindrical concrete specimens	97
Fig. 97: Compressive strength test.....	98
Fig. 98: Indirect tensile strength test.....	99
Fig. 99: Strain gauge installation (G01C).....	100

Fig. 100: Complete sensors numeration	101
Fig. 101: LVDT installation (LVDT-left)	101
Fig. 102: S3 system sensors linked to CBs.....	102
Fig. 103: Bending test final configuration.....	103
Fig. 104: Moment-Curvature graph.....	107
Fig. 105: Fracture - Test 18 - Collapse (Max. Load: 88.45 kN).....	108
Fig. 106: Fracture detail - Test 18 - Collapse (Max. Load: 88.45 kN).....	109
Fig. 107: Crack pattern - Test 5 (Max. Load: 18 kN)	110
Fig. 108: Crack pattern - Test 8 (Max. Load: 25 kN)	110
Fig. 109: Crack pattern - Test 12 (Max. Load: 35 kN)	110
Fig. 110: Crack pattern - Test 14 (Max. Load: 45 kN)	110
Fig. 111: Crack pattern - Test 15 (Max. Load: 55 kN)	111
Fig. 112: Crack pattern - Test 16 (Max. Load: 65 kN)	111
Fig. 113: Crack pattern - Test 18 - Collapse (Max. Load: 88.45 kN)	111
Fig. 114: Crack pattern picture - Test 8 (Max. Load: 25 kN)	112
Fig. 115: Crack pattern picture - Test 9 (Max. Load: 25 kN)	112
Fig. 116: Crack pattern picture - Test 15 (Max. Load: 55 kN)	113
Fig. 117: Load cycle 02: (a) applied load; (b) load-deflection curve; (c) S3 measured pressure; (d) S3 measured temperature; (e) S3 strain; (f) S3 load-strain curves; (g) G strain; (h) G load-strain curves. (Tondolo, 2018)	115
Fig. 118: Load cycle 12: (a) applied load; (b) load-deflection curve; (c) S3 measured pressure; (d) S3 measured temperature; (e) S3 strain; (f) S3 load-strain curves; (g) G strain; (h) G load-strain curves. (Tondolo, 2018)	116
Fig. 119: Load cycle 17: (a) applied load; (b) load-deflection curve; (c) S3 measured pressure; (d) S3 measured temperature; (e) S3 strain; (f) S3 load-strain curves; (g) G strain; (h) G load-strain curves.(Tondolo, 2018)	118
Fig. 120: Load cycle 18: (a) applied load; (b) load-deflection curve; (c) S3 measured pressure; (d) S3 measured temperature; (e) S3 strain (full view); (f) S3 load-strain curves (full view); (g) S3 strain (zoomed view); (h) S3 load-strain curves (zoomed view); (i) G strain; (j) G load-strain curves. (Tondolo, 2018)...	121

Abstract

Structural Health Monitoring is drawing more and more attention in Civil Engineering applications thanks to its big advantages, like safety level increase and costs reduction. Nowadays some innovative systems are focusing on strain measurements in order to detect "inner" behaviour of structures and determine directly internal actions. One of these smart technologies is the "S3 system" (Tondolo, 2016), which is currently under study: along this master's thesis, numerical models and experimental tests are carried out in order to step forward in its development. The smart steel bar equipped with this technology is modelled with a F.E.M. software in order to investigate the S3 system functioning and the behaviour of the reinforcement bar integrated with the measurement unit. Numerical results are compared with the experimental data obtained by previous testing campaign carried out on smart steel bars, i.e. axial tensile load tests realised after a thermal calibration. The results show that the numerical model is capable to describe in a good way the elastic behaviour and the yielding of a smart steel bar. An experimental campaign is carried out on these smart steel bars, instrumented with S3 system sensors. A mechanical characterization of these bars is conducted with axial tensile tests within their elastic behaviour range. They are embedded as part of a reinforcement cage in a RC beam with some additional conventional monitoring systems. Then, the beam is tested in a classical 4-point bending test configuration with different load cases. A good matching between smart and traditional strain measurements is highlighted until the bar under tension works completely with an elastic behaviour: this is a very important result, which confirms the validity of this innovative technology for SHM purposes, at least within elastic range of steel.

Riassunto

Il Monitoraggio Strutturale sta attirando sempre più attenzione nelle applicazioni dell'Ingegneria Civile grazie ai suoi grandi vantaggi, quali l'aumento del livello di sicurezza e la riduzione dei costi. In questi anni alcuni sistemi innovativi si stanno focalizzando sulla misura delle deformazioni al fine di rilevare il comportamento "interiore" delle strutture e determinare direttamente le sollecitazioni. Una di queste nuove tecnologie è il "Sistema S3" (Tondolo, 2016), che è attualmente sotto studio: lungo questa tesi magistrale, sono stati realizzati modelli numerici e prove sperimentali al fine di progredire nel suo sviluppo. La barra d'acciaio "smart" attrezzata con questa tecnologia è modellata on un software agli elementi finiti al fine di investigare il funzionamento del sistema S3 ed il comportamento della barra d'armatura integrata con lo strumento di misura. I risultati dei modelli numerici sono confrontati con i data sperimentali ottenuti dalla precedente campagna di prove effettuata sulle barre d'acciaio "smart", ossia prove a trazione diretta realizzate dopo una calibrazione termica. I risultati mostrano che il modello numerico è in grado di descrivere bene il comportamento elastico e lo snervamento della barra "smart". E' stata realizzata una campagna di prove su queste barre "smart", strumentate con i sensori del sistema S3. E' stata condotta una caratterizzazione meccanica di queste barre prove a trazione diretta, rimanendo entro il loro comportamento elastico. Sono state inserite come parte della gabbia di armatura di una trave in CA in aggiunta a strumenti di monitoraggio convenzionali. Quindi la trave è stata testata in una tipica configurazione di prova a flessione su 4 punti, secondo diversi livelli di carico. E' stato evidenziato un buon accoppiamento tra le misure di deformazione innovative e tradizionali fino a quando la barra tesa rimane in campo elastico; questo è un ottimo risultato, che conferma, la validità di questa nuova tecnologia per gli scopi del Monitoraggio Strutturale, almeno all'interno del campo elastico dell'acciaio.

Introduction

Structural Health Monitoring is a fundamental concept, that is drawing more and more attention in Civil Engineering applications thanks to its big advantages, like safety level increase and costs reduction. It includes all the techniques, which are involved to the process of giving a significant contribution to detect damages in civil structures; damage is intended more in general as a change in a structural configuration, that modify considerably the safety or the performance of a construction. In the past years, there was no much consciousness about the importance of this conceptual tool and the damage detection was mostly carried out by means of visual inspections, but catastrophic events of unexpected collapses started to sensitize the civil engineering world about this theme.

SHM is generally implemented as a periodical control of the main parameters influencing the construction performance, but with the passage of the time and with the development of technology, the needs are changing. Currently, the monitoring system should aim to be a technology with the capability to collect nearly real time information in a large number of significant points distributed for all the structure. The data are recorded and processed by a central acquisition system connected to internet and this could make the measurements available for people not physically present in situ, with advantages in prevention of damages.

Nowadays some innovative systems are focusing on strain measurements in order to detect "inner" behaviour of structures and determine directly internal actions. One of these smart technologies is the "S3 system" (Tondolo, 2016), which is currently under development and it is object of the studies along this thesis. The measurement units are integrated inside reinforcement bars and they have the capability to detect deformations of steel.

The smart steel bar is modelled with a F.E.M. software in order to investigate the S3 system functioning and the behaviour of the reinforcement bar integrated with the measurement unit. Different models are realised, starting from a whole steel bar and then adding gradually more details. The bars are loaded under force or displacement control in order to induce an axial tension in the steel.

Numerical results are compared with the experimental data obtained by previous testing campaign carried out on steel bars equipped with S3 system, i.e. axial tensile load tests realised after a thermal calibration. This is interesting to understand if the F.E.M. models are effective to interpret with good approximation the smart steel bar behaviour, although some more complex thermo-mechanical phenomena could have relevant influence on it.

Finally an experimental campaign is carried out on these smart steel bars, instrumented with S3 system sensors. A mechanical characterization of these bars is conducted with axial tensile tests within their elastic behaviour range. They are embedded as part of a reinforcement cage in a RC beam with some additional conventional monitoring systems. Then, the beam is tested in a classical 4-point bending test configuration with different load cases. Results obtained by this campaign are finally exposed and discussed.

Chapter 1

1. Smart technologies in Structural Health Monitoring

1.1 Monitoring in Civil Engineering

Failure in civil engineering is such an obsession: it is not allowed to happen, but nobody can ever know how far from it we are, until we reach that point, the failure point. We have pages of codes and publications at our back, but we can't feel so safe in relation to collapse and all kinds of failure without any other help. This is due to the fact, that we have to face with a lot of uncertainties, involving the building materials' characteristics, the soil's mechanical behaviour, the static modelling and so on. Concepts like plasticity, capacity design and robustness are straight on the right direction to avoid sudden collapse and to have the control during the critical moments; they are important steps, but they're not enough to have a deep consciousness of the construction behaviour throughout the whole service life of a structure, including the construction phases.

In the early '40s engineers started to have a control of the poured concrete with non-destructive techniques (i.e. rebound hammer, pull out test) in order to be able to know the best moment to remove formworks: these were ones of the first documented monitoring tests in civil engineering applications and they are based on the measurement of the surface hardness of the concrete. As the years go by, there was the need to find tools allowing the estimation of the materials' mechanical properties in existing structures, in order to detect and predict defects during the service life. Many non-destructive techniques were developed just to satisfy this request from the 70s, for example electro-magnetic fields methods, X-ray, thermal fields methods, acoustic emission, ultrasonic methods, Doebling. The concept of *Structural Health Monitoring* (SHM) was finally born and since then any engineer couldn't really think to work without it.

SHM is a strong conceptual instrument with an active function inside the risk management cycle, which usually follows these steps: identifying the possible risk source, assessing the likelihood and the consequences related to each risk, planning the strategies to minimize the risk likelihood and to control consequences, *monitoring* by measuring quantities that can indicate a better knowledge of the risk, evaluating results and updating risk assessment, controlling by taking real actions in order to reduce risk, finally reassessing with periodical reviews and updates. During monitoring process, evaluation and interpretation are two distinguished parts: firstly data should be validate, verifying also that they are enough, and then they should be interpreted, understanding their meaning in relation to the monitoring situation. (Marr, 2017)

Structural Health Monitoring methods are improving nowadays thanks to technological development, but also because of a higher consciousness in civil engineering world, even if it's still not enough. We are going to explain in detail about how much SHM is important, then we will talk about conventional and innovative technologies to monitor structures, focusing on those that have a direct look at the internal structural behaviour by means of *strain* measurements.

1.2 Importance of SHM

It's really essential to monitor the performance of a construction project and there are several reasons to say that. First of all, the monitoring system is able to indicate the impending failure of the structure and this is probably the strongest need that pushed the SHM development; the most crucial aim for a civil engineer is to avoid structural collapse and this is a fundamental tool straight on this direction. It is also important to have a good SHM, in order to provide a warning of unacceptable performance. Indeed, this is the second duty for an engineer: the construction should not only be alive, but it must work correctly too, in relation to functional parameters given by client's requests and codes' specifications. A good SHM is used since the very first construction phases, providing a full real-time control over the building operations in order to have a strictly monitoring of the construction performance since the beginning.(Marr, 2017)

The power of the SHM is to reveal unknowns in some different shapes, giving additional information than there were available before; if all these data are well interpreted, they provide a great advance in the state-of-knowledge, allowing for example the critical design assumptions evaluation, the performance change detection for assessing and allocating damages or the performance improvement

to meet desired goals. Having a deeper consciousness of the health state of the structure gives the ability to devise remedial measures to fix problems in a more precise and faster way; if this happens during the construction phases, it represents a big advantage, because it avoids bigger problems later during the service life of the structure. Shortly, SHM is really a powerful instrument to reduce uncertainties in a world full of them and, at least just because of this, all of us should be convinced that it is really fundamental in civil engineering; but there are some more reasons. (Marr, 2017)

A good monitoring helps also to communicate in a better way with everybody. It assesses the contractor's means and methods of construction, allowing a strict control over them in order to let the contractor understand that the design should be respect as much rigidly as possible under the design specifications and the engineer directions; if contractor's methods of construction are wrong in some aspects, it is easier to demonstrate the mistake and to ask him to solve the problem. Having detailed information about the state of the construction helps also to be a good neighbour, informing stakeholders about the complete situation and the updated effects on the near environment. Indeed, it is very important to check the situation next to the construction site, in order to do not create serious damages in existing structures or facilities. At the same time, SHM is very useful to reduce litigation associated with claims and failure and to comply with regulatory and governance guidelines. (Marr, 2017)

It's necessary to communicate to clients the advantages of managing risk through monitoring systems; a good way to let them understand how useful SHM could be is just talking about money. Risk is defined as the probability of failure times consequences or the likelihood of some undesirable events times the impact; some kinds of consequences are loss of life, loss of facility, damage to other property, costs to mitigate and repair, delays (very costly), cost of litigation, damage to reputation. If these values are expressed in terms of money, the risk is defined as well, so it represents the potential loss of money that it is reasonable to expect in certain construction works. Monitoring system is a cost, but it has also the capability to reduce costs, lowering probability of failure and consequences and this could lead clients to a potential big save of money. (Marr, 2017)

An interesting example is given by the monitoring system provided on 150 existing structures next to excavation sites during Big Dig works in Boston. The global risk was calculated taking into account collapse, major damage and disruption, construction delays for unexpected performance and architectural-structural damage: the total estimated value of risk was 550 M\$, plus the risk of losses of life and injuries. At the end of construction, the total amount paid for repairs was 9 millions \$ and the overall costs for monitoring systems was 60 millions \$. This means that there was a potential save of money of almost 500 millions \$ and this is mostly due to the state-of-knowledge provided by the Structural Health Monitoring system. (Marr, 2017)

Thanks to the electronic technology development, right now there is the possibility to collect a lot of data wireless and real time; the challenge for further improvement is related to maintenance issues of the instrumentation. Real time monitoring is really important, because every single little warning could help to take decisions in order to avoid failure and to reduce consequences, before they could rapidly occur and it allows also a better knowledge of the cause-effect connection. (Marr, 2017)

At the end, some key concepts to guarantee an effective performance monitoring in a risk management cycle are shown: it is necessary to have a strong champion, an organizational structure, a dedicated planning, a training for workers, an appropriate technology, a systematic approach, a response preparedness, a good maintenance, detailed documentation, complete reports and messages.

1.3 Conventional monitoring systems for concrete structures

Throughout the years, some different Non-Destructive Evaluation (NDE) techniques were developed and here below some of the conventional monitoring systems for existing concrete structures are listed; each one of them has its own advantages and disadvantages and this is why civil engineer commonly combine two or more methods for the same structural evaluation. (Abdo, 2014)

Items	Type of damage	Method(s) to detect damage	Comments
Appearance	Defects (surface)	Digital still camera, Thermograph	Including honeycomb, cold joints
	Defects (inside)	Sonic, Thermograph, Radar Ultra-sonic, X-ray, Impact echo	Voids inside and at the back of the structure
Strength and stiffness	Concrete strength	Rebound hammer	Problem in accuracy
	Modulus of elasticity	Ultra-sonic velocity	-----
	Distribution	Digital still camera, Thermograph	-----
Cracks and spalling	Crack width	Digital still camera, Thermograph	Direct measurement
	Crack depth	Ultra sonic	Effects of bars
	Cracking	Acoustic emission	Continuous measurements
Steel corrosion	Location	Natural potential	Location at that time
	Corrosion degree	Natural potential, Electric-current analysis	Periodic measurements required

Fig. 1: List of non-destructive techniques for concrete structures monitoring

There are some limitations in these NDE techniques: the quality of the measurement is dependent on the operator experience, local results in one area doesn't necessarily represent the global behaviour of the structure and so it is important to have a large number of measurement points to have a significant result about structural conditions. Thus these techniques are used only for localized evaluations and they fail when used for a complete structural analysis; this is why the most innovative monitoring systems has the aim to analyze the dynamic-static characteristics of a structure, by monitoring dynamic-static responses real-time and in a large number of points with an automatic system of data acquisition and processing. (Abdo, 2014)

1.4 Conventional strain measurement system: Metallic Strain Gauge

Now we are going to focus on a more specific sector in the world of Structural Health Monitoring, the strain measurement, which indirectly bring to the internal actions' distribution knowledge. Strain gauge is the conventional instrument, which is able to measure strain in specimens for laboratory test or in structural elements for Structural Health Monitoring. It can be realized in different kinds, but one of the most common solution is with a metallic foil or a very fine wire, arranged in a grid pattern and parallel to the direction of the strain. The grid is bonded to a thin carrier, attached to the element; the strain is transferred directly to the instrument, which responds with a linear change in electrical resistance.

An important parameter is the sensitivity to strain, expressed by the gauge factor GF, that is the ratio of the fractional change in electrical resistance to the fractional change in strain; this value is usually around 2. (National Instruments)

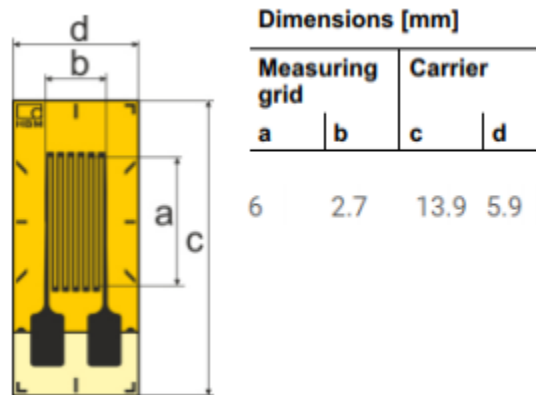


Fig. 2: HBM Strain Gauge 1-LY41-6/120

This is an HBM Strain Gauge is shown as example and this gauge will be applied on steel bars during the experimental study, presented in Chapter 2. The instrument is made of steel foil and it has a nominal resistance of 120 Ohm with a maximum permissible effective supply voltage of 8 V. Gauge factor is $2.04 \pm 1.00\%$, transverse sensitivity is -0.1% and maximum longitudinal deformation is equal to 5% ($50,000 \mu\epsilon$).

To measure small changes in resistance, strain gage configurations are based on the concept of a Wheatstone bridge. The general Wheatstone bridge is a network of four resistive arms with an excitation voltage V_{EX} , that is applied across the bridge.

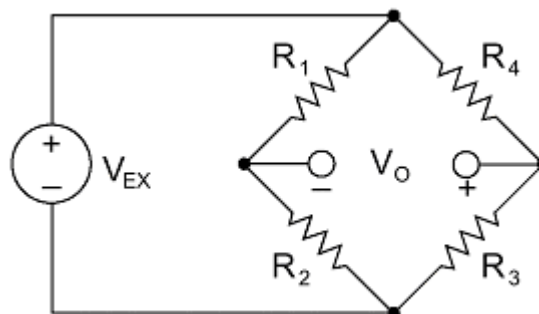


Fig. 3: Wheatstone Bridge circuit

The Wheatstone bridge is the electrical equivalent of two parallel voltage divider circuits. R_1 and R_2 compose one voltage divider circuit, and R_4 and R_3 compose the second voltage divider circuit. The output of a Wheatstone bridge, V_o , is measured between the middle nodes of the two voltage dividers.

$$V_0 = \left[\frac{R_3}{R_3 + R_4} - \frac{R_2}{R_1 + R_2} \right] \times V_{EX}$$

From this equation, when $R_1 / R_2 = R_4 / R_3$, the voltage output V_0 is zero. Under these conditions, the bridge is said to be balanced. Any change in resistance in any arm of the bridge results in a nonzero output voltage. Therefore, replacing R_4 with an active strain gage, any changes in the strain gage resistance unbalance the bridge and produce a nonzero output voltage that is a function of strain.

There are 3 types of strain gage configurations, depending on the number of active elements in the Wheatstone bridge, the orientation of the strain gages and the type of measured strain: quarter-bridge strain gauge, half-bridge strain gauge and full-bridge strain gauge.

1.4.1 Quarter-Bridge Strain Gauge

Configuration type I allows axial or bending strain measurement, requiring a passive quarter-bridge completion resistor known as a dummy resistor and half-bridge completion resistors to complete the Wheatstone bridge. R_4 is an active strain gage measuring the tensile strain ($+\epsilon$), while R_3 is a passive dummy resistor, usually placed on another specimen made of same material under same temperature conditions, but without load applied.

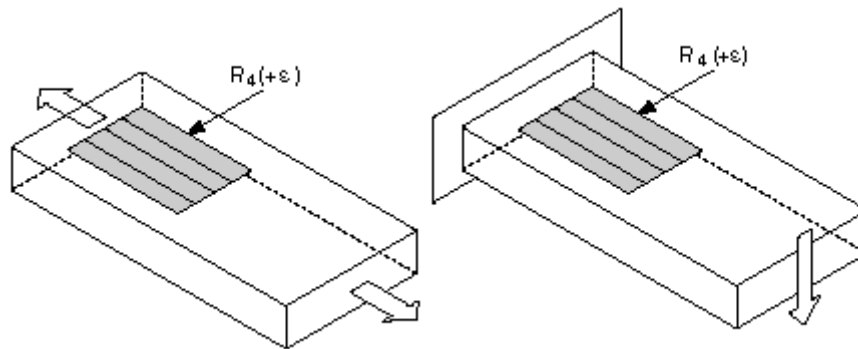


Fig. 4: Quarter-Bridge Strain Gauge configuration Type 1

The resistance of the strain gage should change ideally in response to applied strain. However, strain gage material also responds to changes in temperature, as well as the specimen material which the gage is applied to. The quarter-bridge strain gage configuration type II helps to minimize the effect of temperature by using two strain gages in the bridge.

Typically one strain gage (R_4) is active and the second strain gage (R_3) is mounted in close thermal contact, but not bonded to the specimen and placed transverse to the principal axis of strain. Therefore the strain has little effect on this dummy gage, but any temperature changes affect both gages in the same way. Because the temperature changes are identical in the two strain gages, the ratio of their resistance does not change, so the output voltage (V_o) almost does not change because of temperature effects.

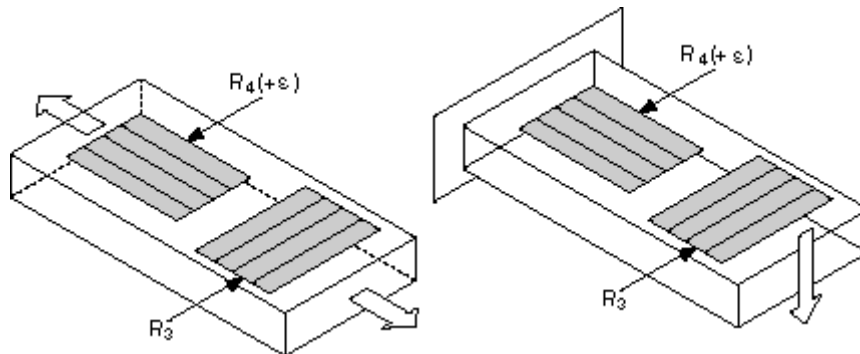


Fig. 5: Quarter-Bridge Strain Gauge configuration Type 2

1.4.2 Half-Bridge Strain Gauge

The bridge's sensitivity to strain can be doubled by making both strain gages active in a half-bridge configuration. Configuration type I allows axial or bending strain measurement, requiring half-bridge completion resistors to complete the Wheatstone bridge. R_4 is an active strain gage measuring the tensile strain ($+\epsilon$) and R_3 is an active strain gage compensating for Poisson's effect ($-\nu\epsilon$).

This configuration is commonly confused with the quarter-bridge type II configuration, but type I has an active R_3 element that is bonded to the strain specimen.

Configuration type I allows bending strain measurement only, requiring half-bridge completion resistors to complete the Wheatstone bridge. R_4 is an active strain gage measuring the tensile strain ($+\epsilon$) and R_3 is an active strain gage measuring the compressive strain ($-\epsilon$).

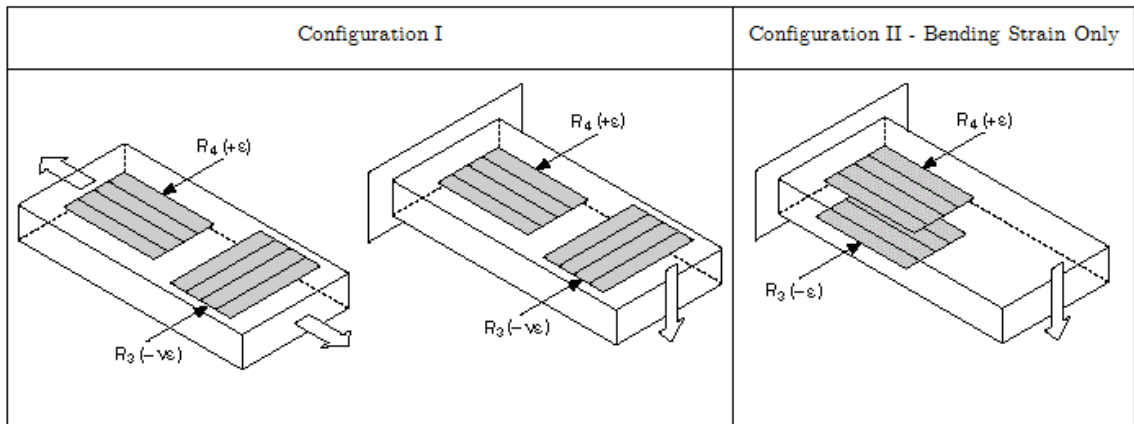


Fig. 6: Half-Bridge Strain Gauge configuration Types

1.4.3 Full-Bridge Strain Gauge

A full-bridge strain gage configuration has four active strain gages and it is available in three different types. Types 1 and 2 measure bending strain, type 3 measures axial strain; types 2 and 3 compensate for the Poisson effect, but all three types minimize the effects of temperature.

Configuration Type 1 is highly sensitive to bending strain only; R1 and R3 are active strain gages measuring compressive strain ($-\epsilon$), while R2 and R4 are active strain gages measuring tensile strain ($+\epsilon$). Configuration Type II is sensitive to bending strain only; R1 is an active strain gage measuring the compressive Poisson effect ($-\nu\epsilon$), R2 is an active strain gage measuring the tensile Poisson effect ($+\nu\epsilon$), R3 is an active strain gage measuring the compressive strain ($-\epsilon$) and R4 is an active strain gage measuring the tensile strain ($+\epsilon$). Configuration Type III allows axial strain measurement; R1 and R3 are active strain gages measuring the compressive Poisson effect ($-\nu\epsilon$), while R2 and R4 are active strain gages measuring the tensile strain ($+\epsilon$).

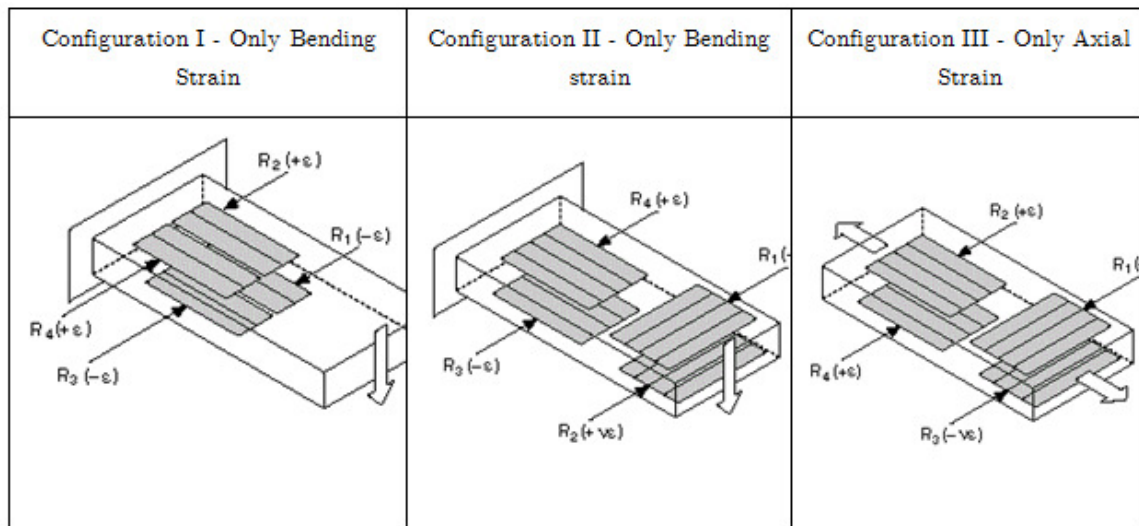


Fig. 7: Full-Bridge Strain Gauge configuration Types

1.5 Innovative strain monitoring systems

In this chapter, some of the most innovative strain measurement technologies are shown; the description of these systems are mostly taken from their developers' articles written during the last 10 years and some of them are currently in research phase. This means that strain measurements are getting always more attention in the world of Structural Health Monitoring, because of the power of these results, which are explicitly talking about the internal behaviour of the structure; indeed, they allow a direct control over stresses and internal actions distribution, while the traditional SHM systems were often looking only at the external part, e.g. checking displacements and cracks, but without a real possibility to predict them. These smart technologies are also focused on having high precision real-time measurement system with a powerful acquisition system, where all data are collected together simultaneously.

1.5.1 Passive Wireless RFID Strain Sensors

This first technology is a passive wireless radio frequency-identification (RFID) sensor: stress produces a change of magnetic field thank to an amorphous metal ribbon. This change is detected by a giant magnetoresistance magnetic field sensor and then a digital value is obtained with a RFID chip for wireless access. Because of easy signal analysis and low power consumption, this monitoring system is a good choice for long term strain measurements in narrow places, difficult to reach. (Windl, 2016)

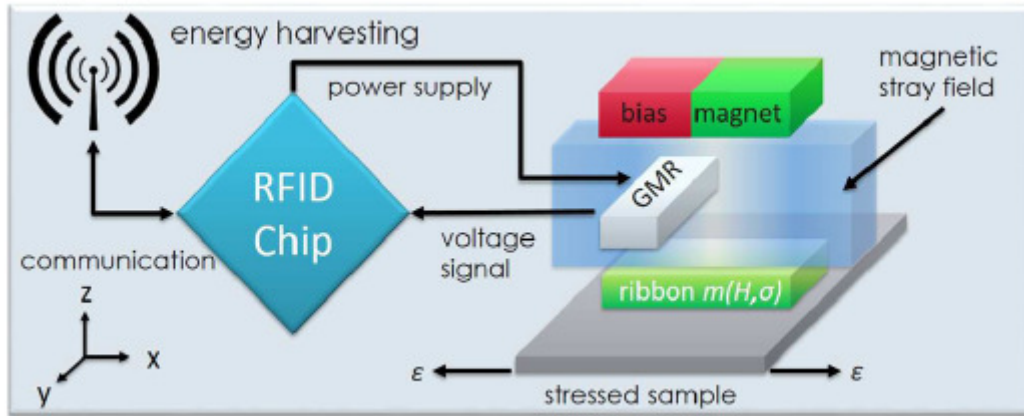


Fig. 8: RFID Strain Sensor configuration

The system is composed by three parts: "a radio frequency-identification (RFID) tag, a giant magnetoresistance (GMR) magnetic field sensor and a transducer". Starting from the measured change of a magnetic stray field, it is possible to determine the physical quantities under observation. The amorphous metal ribbon is magnetized by a bias field, generated by a bias magnet: these two elements are part of the transducer. Villari effect says that amorphous metals' magnetization varies in relation to an applied magnetic field and stress. Giant magnetoresistance magnetic field sensor detects the change of magnetic stray field and it allows the determination of stress, by considering the Villari effect. The radio frequency-identification tag allows a wireless access to GMR sensor output and it also supplies the sensor by means of the energy harvesting feature. (Windl, 2016)

1.5.2 Passive Wireless Strain Sensors with Magnetoelastic Beam Elements

"Resonant wireless strain sensors fabricated from magnetoelastic alloys" work with the ΔE effect, which relates change in stiffness of magnetoelastic materials to an applied strain or magnetic field; this change is obtained by measuring a shift in the resonant frequency. A peak in frequency spectrum of interrogation coils' voltage is detected wirelessly in order to determine resonant response in the structure. The sensor dynamic range is increased thanks to a strain-attenuating spring structure and it prevents magnetic saturation at low levels of strain. There are two types of sensors, single and differential: the latter has an additional cantilever with strain-independent resonant response, while they both have doubly-anchored resonant strips. (Pepakayala, 2014)

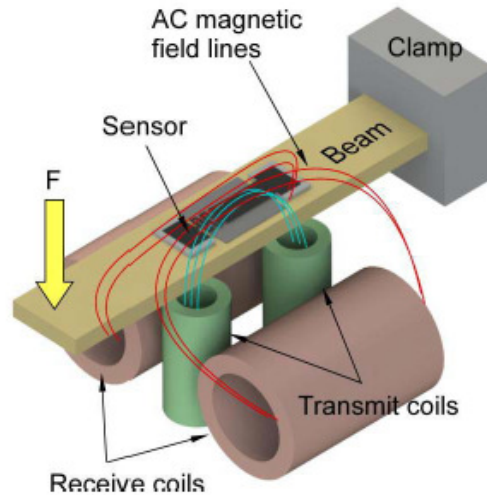


Fig. 9: Wireless Passive Strain Sensor configuration

Total strain is due to elastic strain and Villari effect in a magnetoelastic material, where a state of stress is applied: the second component represents a magnetic moment rotation. A system of coils is realised in order to catch the sensor response: the transmit coils are used to understand the range of frequency, where resonance is expected to be. Then an elevated response in receive coils allows the detection of resonant frequency. (Pepakayala, 2014)

1.5.3 Skin-like sensors

The following smart technologies are currently in research phase. This first one is a *"dielectric-elastomer and micro-electronics-based sensor, formed from a large highly extensible capacitance sensing membrane supported by advanced microelectronic circuitry"*. The sensor is realised around a thin silicone elastomer membrane and it is coated with compliant electrodes on both sides. This component is integrated with data acquisition module, communication module and power electronics into a compact unit: there are some advantages related to this device, like energy efficiency and ease of installation over different kinds of surface. (Loupos, 2017)

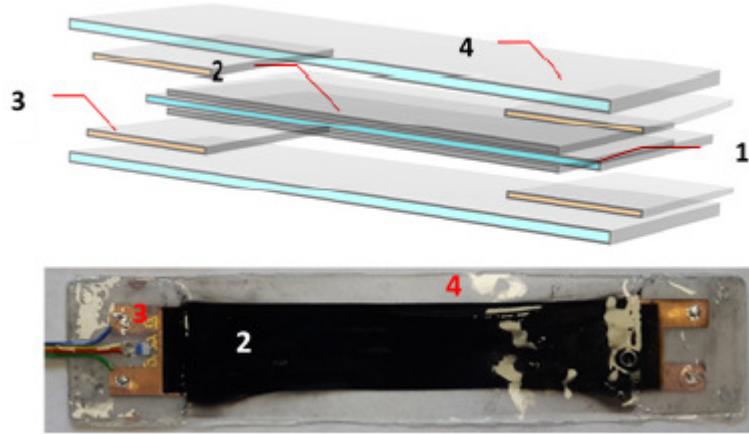


Fig. 10: Skin-like sensor configuration

The skin-like sensors measure continuously capacitance variations due to sensor deformation in order to determine the state of strain in that point. Between this stretchable elastomeric material sensor and the microcontroller, there is a complex sensor which allows data acquisition. The whole integrated system is briefly composed of these parts: a skin-like sensor measures strains over the surface, the data acquisition system converts into digital values the measurements, then the communication module receives and transmits all the data implementing the communications operational logic and finally the processing module computes all the data to realise a global monitoring of the structure by means of the information given by all the sensors applied. [6] (Loupos, 2017)

1.5.4 Wireless Smart Sensors platform

A new modular hardware platform for Structural Health Monitoring is here presented: this is able to sense not only strain and temperature, but also 3-axis acceleration and high-level voltage signals, producing a multi-scale advanced monitoring. Wireless smart sensors are a good choice in order to allow nodes communication without useless costs for cabling; each node is provided with an *"on-board microprocessor that can be used for digital signal processing, self-diagnosis, self-calibration, self-identification and self-adaption functions"*. It's really easy to place or remove these sensors after the system's instrumentation and this is another advantage, because it means an high flexibility of the monitoring system during all its phases. The platform *"addresses critical SHM needs, enabling tightly synchronized sensing, addressing data loss and efficiently implementing the demanding numerical algorithm required, with limited resources"*. (Spencer, 2016)

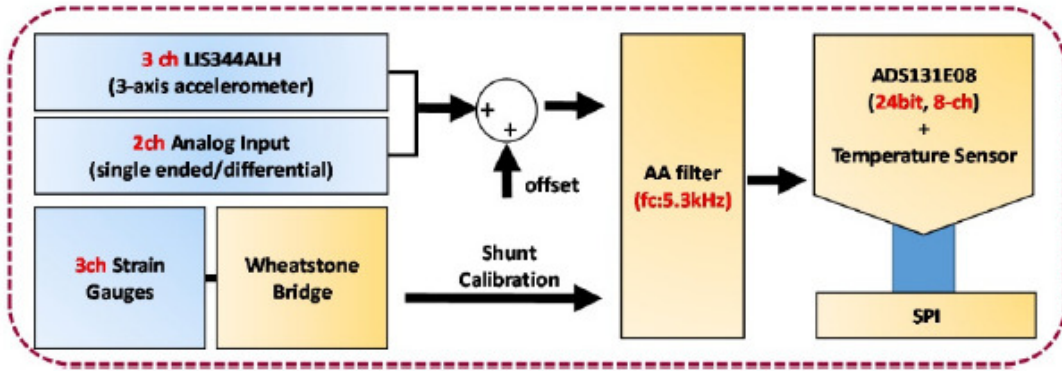


Fig. 11: Xnode platform linked to WSS

The board uses a 24-bit analogue-to-digital converter (ADC) with 8 channels: three channels are taken by 3-axis accelerometer and other three by the strain gauge circuit, where electrical signals are converted into strain measurements by means of embedded shunt calibration. The strain gauges are linked to the sensor board by external connectors and the signal is supplied through the ADC. The platform provides synchronized distributed data in order to realise a real-time remote monitoring system; the Wireless Smart Sensors network is constantly under control and it gives information about a lot of points distributed all over the structure. (Spencer, 2016)

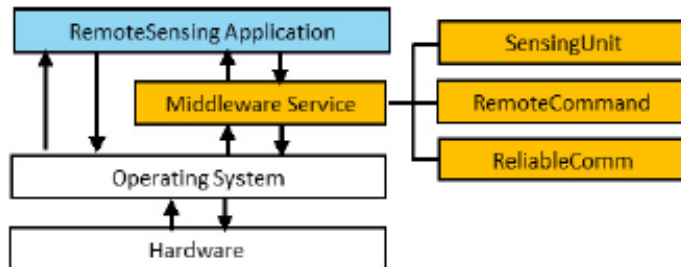


Fig. 12: Xnode platform operation

1.5.5 Frictional strain gage in WSS platform

The field of Structural Health Monitoring applications for this last smart technology concerns steel structures. The metal foil strain gauges give problems during the installation, because it requires a lot of time and it could be not so easy to realise. An alternative is *"a strain checker, a non-destructive-type strain sensor composed of a frictional strain gauge and magnet attachment"*, developed by Tokyo Sokki Kenkyujo. (Spencer, 2013)

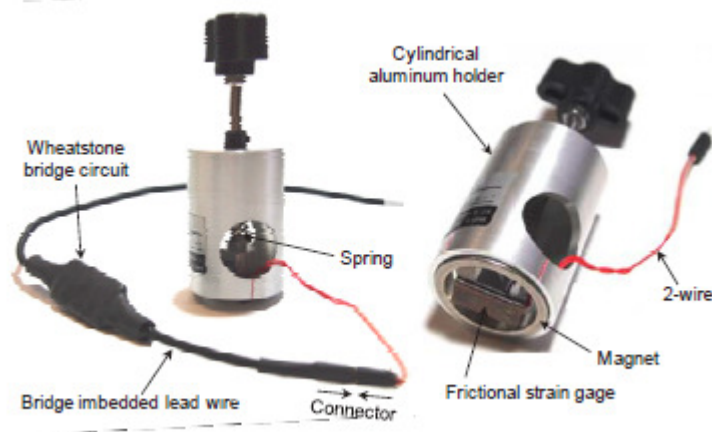


Fig. 13: Frictional Strain Gauge with a cylindrical magnet

Traditional metal foil strain gauges detect strain through adhesive; this innovative instrument uses a cylindrical magnet in order to attach the aluminium to a structure made of steel, while an inner spring is pushing the frictional strain gauge. The gauge is embedded in a base plate in direct contact with the surface and this is coated by emery powder: therefore the sensing system works by friction, so that adhesives are not necessary and the measurements can occur without removing any painting layer from structure. The gauge is linked to Wheatstone-bridge embedded lead wire, thus *"the differential voltage signals from the strain checker system needs to be fed to the amplifier directly"*. Combining this instrument with the Wireless Smart Sensors platform, it is possible to obtain a very interesting real-time remote integrated system, which is able to monitor the performance of steel structures. (Spencer, 2013)

1.5.6 Strain-sensing antenna

Another passive wireless strain sensor solution for Structural Health Monitoring applications is a quarter-wavelength folded patch antenna. According to theoretical and experimental studies, there is a linear relation between strain and normalized resonance frequency shift; there is a better sensitivity for longitudinal strain than for transversal one. (Chen, 2017)

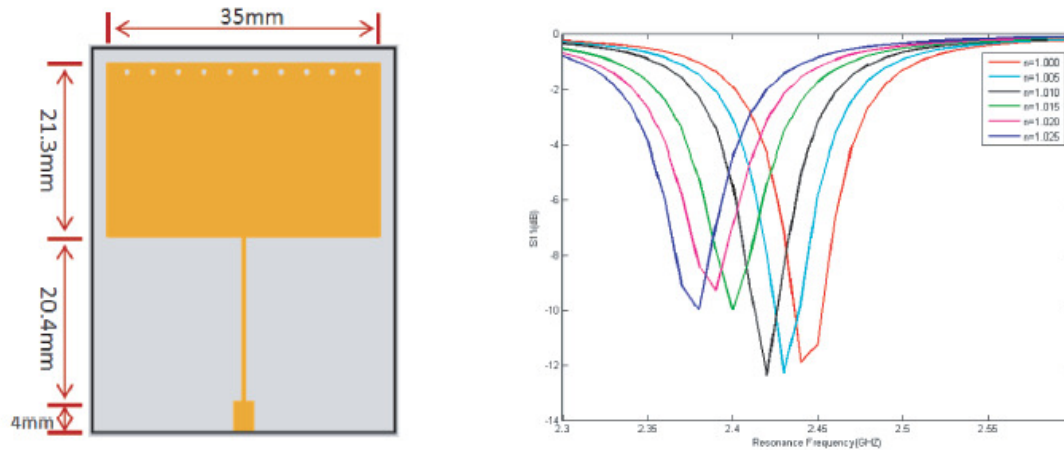


Fig. 14: Strain sensing antenna operation

Electromagnetic resonance frequency of the antenna is related to its physical dimensions, therefore when strain is applied, these dimensions change and the resonance frequency as well. Moreover bigger antenna has an higher resonance frequency and this has a better influence on the strain sensitivity. Bonding the antenna to the structure, it is possible to detect strain by considering the relation between deformation of the element and resonance frequency shift. (Chen, 2017)

1.6 Innovative strain monitoring system: Fibre Optic

The main technology among all strain monitoring systems right now is represented by Fibre Optic. This innovative material is really spread nowadays in multiple applications, especially in telecommunications world. In the last years, it started to be adopted for Structural Health Monitoring uses too, getting a big breakthrough in several aspects. The innovation consists on the fact that typical optical fibres become full-fledged sensors and thus very long cables can be sensed in order to get an effective measurement of strain and temperature along a big distance and on a great number of points. Basically there are two main different approaches for Fibre Optic applications in SHM: quasi-distributed (i.e. Fibre Bragg Grating) and distributed Fibre Optic sensors. For both of them a bulleted list with pros and cons will be presented at the end of respective subchapter. Here below there is a synthetic table showing some different Fibre Optic technologies and their capabilities to measure strain and/or temperature.

Fibre Optic Sensors	Strain sensing	Temperature sensing
Distributed FOS		
Based on Brillouin scattering	x	x
Based on Rayleigh scattering	x	
Based on Raman scattering		x
Quasi-distributed FOS		
Fiber Bragg Grating sensors	x	x
Short-gauge FOS		
Based on extrinsic Fabry-Perot interferometry	x	x
Long-gauge FOS		
Based on Michelson and Mach-Zender interferometry	x	

1.6.1 Fibre Bragg Grating Sensor (FBGS)

This technology works with a particular fibre optic, realized by exposing some portions of the core to a periodic pattern of intense ultraviolet light, that produces a permanent increase of the fibre's core refractive index with a fixed index modulation, called grating: each portion of the core is usually long 1 cm, containing around 20,000 of refractive index changes and this Bragg grating is able to reflect a specific wavelength. When the light propagates through the grating with a negligible attenuation, only these Bragg wavelengths are strongly back-reflected. Comparing the reflected signal in the FBG between the unstrained and the strained configuration, it is possible to measure the axial strain in that point and consequentially the stress too. (FBGS)

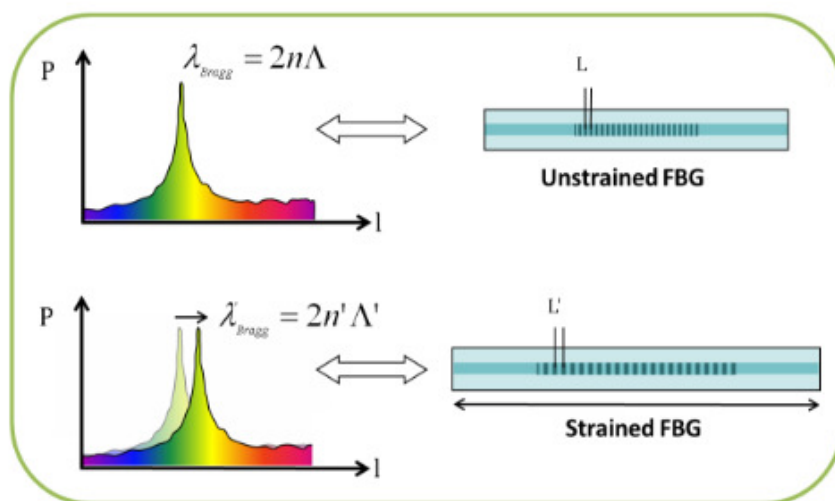


Fig. 15: Bragg wavelength shift in FBG Sensor

The fibre optic is usually glued to the structural element or sometimes it is embedded inside. There are several advantages in relation to the traditional strain gages, like compactness, immunity to electromagnetic interference, multiplex capability and glass inertness. The signal variation is depending also on the temperature, so it's important to calibrate the instrument in relation to this variable. (Park, 2017)

An innovative way to interrogate the FBG is by using a Fourier-domain mode locked (FDML) wavelength-swept laser (WSL), which is an high speed and a wide band optical source; the main advantage of this dynamic sensor interrogation is that it allows a real-time high speed measurement in temporal domain. (Park, 2017)

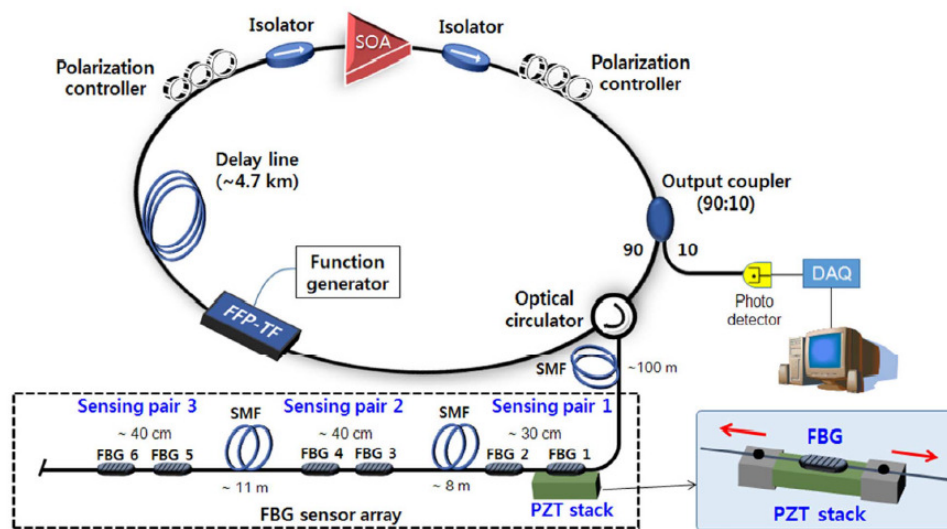


Fig. 16: Fibre Bragg Grating Sensors interrogation and acquisition system

Advantages:

- High strain resolution (best performance $<1 \mu\epsilon$)
- High strain accuracy (best performance $\pm 2 \mu\epsilon$)
- Low size and weight of the fibres
- High resistance to degradation (good behaviour in harsh environment)
- Real-time measurements
- Possibility to realise a wireless monitoring
- Embeddable capability
- Inherent immunity to electromagnetic and radiofrequency interference
- Long-term reliability (good signal stability and system durability)
- Large distance between sensors and interrogator (several km)

- High multiplexing capability (having several sensors connected to a single optical fibre)
- Measurement independence of interrogator or acquisition system power fluctuations
- Cost-effective solution for medium/large projects
- High fatigue limits
- Single ended cabling

Disadvantages:

- Need for thermal compensation
- Complexity of cabling
- Difficulties in replacing/maintenance (when embedded)
- High cost of sensing system
- Problems of the network in case of single failure
- Difficulties in sensor validation in relation to the real behaviour of the structure

1.6.2 Distributed Fibre Optic Strain (FOS) sensors

The other main application of fibre optic in Structural Health Monitoring concerns *distributed* strain and temperature *sensing*. When light is pulsed through the cable, a part of it is backscattered because of some imperfections. There are many technologies, which have the capability to catch backscattering components and to transform them in strain or temperature measurements: optical time domain reflectometry and optical time domain analysis are the most common sensing technologies and they are commonly based on Brillouin scattering (BOTDR and BOTDA) or on Rayleigh scattering (OTDR), while Raman scattering can be used only for temperature measurements. (Güemes, 2010)

The principle is quite simple: strain or temperature variations provoke density variations in the cable and this entails a change in acoustic velocity and in refractive index; the consequence is a linear proportion between strain or temperature variation and backscattered light frequency shift. (Soga, 2014)

$$v_b = v_{b0} + M\Delta\varepsilon + N\Delta T$$

In this formulation, we can see how peak frequency under observation ν_b shifts depending linearly on strain and/or temperature variations by means of two proportionality constants: M is around 0.5 GHz per 0.01 ϵ and N is around 1 MHz per $^{\circ}\text{C}$. This shift is measured in order to determine these physical quantities in a certain position, where the backscattered light comes from: the location of that measurement point is calculated starting from time elapsed since light is pumped into the cable until it comes back to the analyzer. (Soga, 2014)

BOTDR system has a two-ways configuration, because the light is pumped from the same end of the cable, where the backscattered light goes back. The reflectometer detects the frequency component under interest with an high spectral resolution analysis and the position with a time domain analysis. It is better to have longer pulse, in order to read a signal with a good resolution, but at the same time the gauge could be very long along the whole length of the cable, so a compromise should be reached. (Soga, 2014)

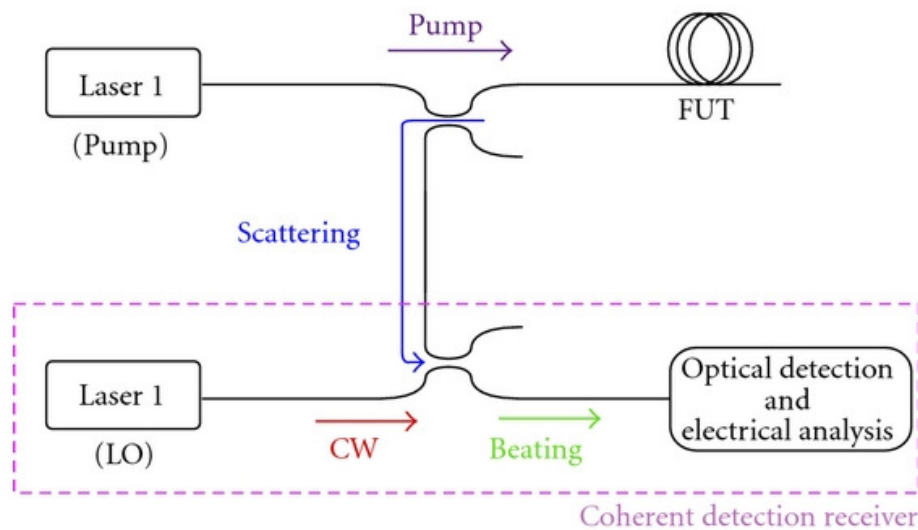


Fig. 17: BOTDR configuration (Galindez-Jamioy, 2012)

Instead BOTDA system has a different configuration, because one light wave is pumped from one edge into the fibre, while another one goes in from the opposite edge of the fibre; the first wave is called "pump" and the second one "probe". In this case the configuration is a loop and light has access from both the extremities of the cable; the position is determined by looking at local coupling on counter-propagated wave and the backscattered signal detection is enhanced. This solution is less practical because of the loop configuration, but it has generally a better strain resolution than the previous solution. (Soga, 2014)

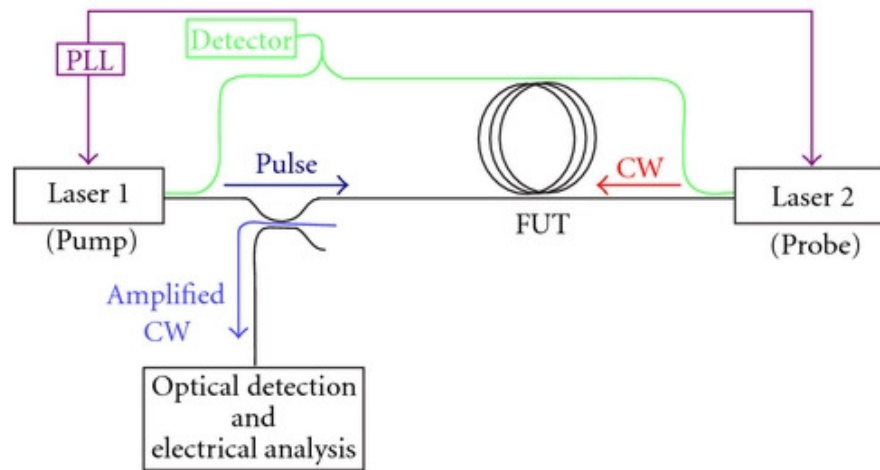


Fig. 18: BOTDA configuration (Galindez-Jamioy, 2012)

It is necessary to compensate temperature, in order to understand Brillouin frequency shift contribution due to strain. An idea is installing fibre optic in a gel filled loose tube in order to avoid any mechanical strain transfer from the jacket to the core: this cable runs alongside the strain sensing cable and it detects frequency shift only related to thermal deformations. (Soga, 2014)

Another technology for distributed sensing measurements with fibre optic is optical frequency domain reflectometry (OFDR) and it measures changes in frequency of the Rayleigh scatter along the cable. Strain and/or temperature are obtained by comparing stressed fibre optic results with reference values in unloaded situation. Also in this case temperature compensation with a "dummy cable" is necessary, thus the thermal strain can be subtracted from the results obtained in the cable bonded to the structure in order to catch mechanical strain. (DeRosa, 2013)

Along up to 70 m of cable and for a spatial resolution of 10 mm, it is possible to have a strain resolution of $1 \mu\epsilon$. Currently only fibre optic technologies are able to reach this level of resolution in strain measurements for Structural Health Monitoring applications. (DeRosa, 2013)

Advantages:

- High strain resolution (best performance $<1 \mu\epsilon$)
- High strain accuracy (best performance $\pm 2 \mu\epsilon$)
- Low size and weight of the fibres
- High resistance to degradation (good behaviour in harsh environment)

- Dynamic measurements (acquisition time from 1 second to 2 minutes for high resolution ones)
- Continuous strain profile as output
- Possibility to realise a wireless monitoring
- Embeddable capability
- Inherent immunity to electromagnetic and radiofrequency interference
- Long-term reliability (good signal stability and system durability)
- Very large distance between sensors and interrogator (several km)
- Cost-effective solution for medium/large projects
- High fatigue limits
- High multiplexing capability (capability to read distributed signals in a single optical fibre)

Disadvantages:

- Need for thermal compensation
- Complexity of cabling
- High cost of the sensing system
- Strain resolution is influenced by the interrogation duration
- Spatial resolution is influenced by the sensing range (km) chosen
- Difficulties in replacing/maintenance (when embedded)
- Problems of the network in case of a single failure
- Difficulties in sensor validation in relation to the real behaviour of the structure
- Starting and ending point of the cable should be the same for closed loop

1.6.3 Fabry-Perot cavities sensors

Another solution is represented by Fabry-Perot cavities, which can measure strain thanks to the detection of changes in cavity parameters; they work as the basis in the transducer system or as part of the optoelectronic unit. Their application can be active, like in an integrating system with a fibre laser sensor, but also passive. One famous technology *"is the Extrinsic Fabry-Perot Interferometer (EFPI) that is constituted by a capillary silica tube containing two cleaved optical fibres facing each other, but leaving an air gap of a few microns or tens of microns between them"*. (López-Higuera, 2014)

Pumping the light into one fibre, a back-reflected interference signal is produced and this is related to the reflection of light at the level of the interface between air and glass; in order to understand the variations in the fibre spacing, this interference is demodulated. (López-Higuera, 2014)



Fig. 19: Strain transducer

1.6.4 Multicore Fibre (MCF) based on helical structures

The last technology is an *"highly sensitive strain sensor based on helical structures assisted Mach Zehnder interference in an all-solid heterogeneous multicore fibre, which was locally twisted into helical structures and then spliced between two short sections of multimode fibres (MMFs) to construct an in-line MZI"*. The multicore fibre with helical structures is divided in two segments of multimodal fibres and linked to an optical spectrum analyzer and a light source. (Zhang, 2017)

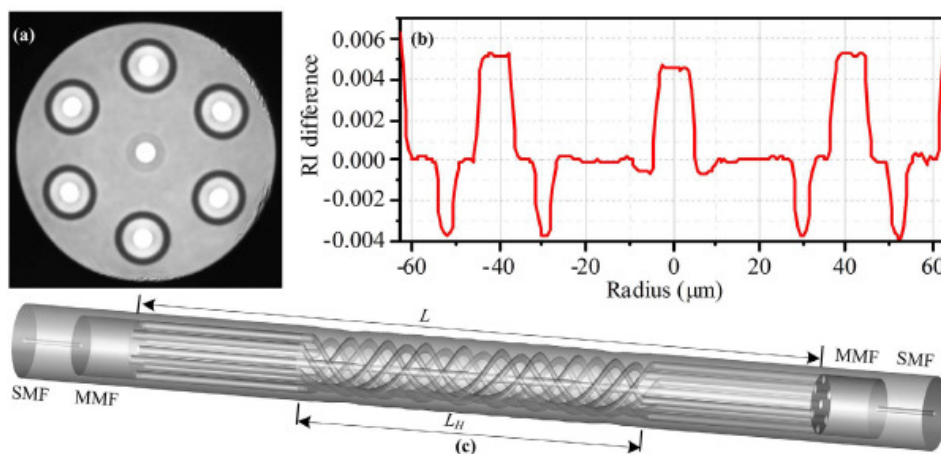


Fig. 20: Multicore Fibre Optic operation

With this technology, we can reach a strain sensitivity much higher than that related to the multicore fibre by using Mach-Zehnder interferometer. The mechanical strength is better than air-cavity based schemes, because there are all-solid fibres with the same cladding diameter. This smart technology has not only a robust structure and an high sensitivity but also other advantages, like low cost and strain-temperature discrimination. (Zhang, 2017)

1.7 Innovative strain monitoring technology: S3 system

Smart steel S3 system has completely changed the way to measure strain state with revolutionary ideas and it will be studied in details for the all this paper since Chapter 2. Conventionally strain transducer is placed upon steel bars' surface in order to catch internal state of strain and stress in reinforced concrete elements, but this brings serious problems in terms of maintenance because of harsh environment which the instrument is exposed to since its installation. The transducer could be also an obstacle for bonding, because of its position on the interface between concrete and steel bar and this local modification could alter the strain measurements. The first innovative solution is embedding the instrumentation inside the bar, in order to solve both problems. In *S3 system*, the transducer is located in an cylindrical hole drilled through the bar.

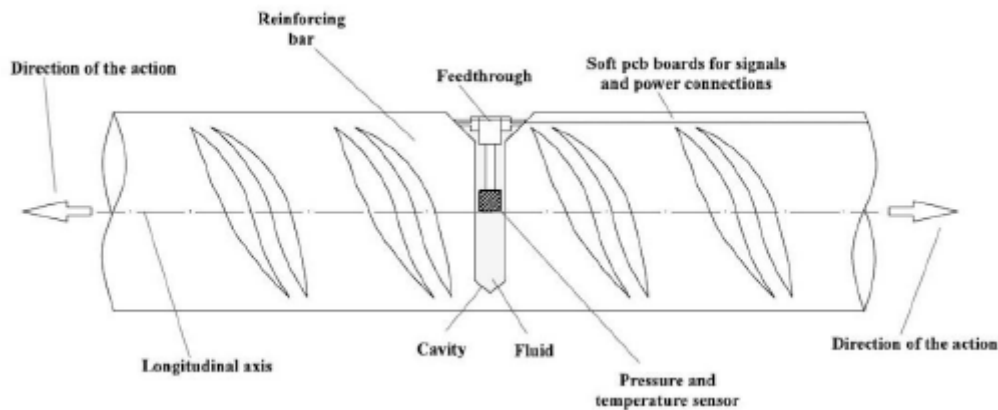


Fig. 21: Longitudinal section of the smart steel bar

The transducer inside cavity is a commercial Micro Electro-Mechanical System (MEMS) barometric sensor, very cheap (around 2\$) and small (about $2 \times 3 \times 1 \text{ mm}^3$). The sensor LPS25H (STMicroelectronics®) is mounted on an hard PCB contained inside the cavity which is closed by an electrical feed-through element, designed to let a soft PCB pass through it in order to allow signals transmission and power supply. The hole is hermetically sealed and the sensor is connected by the soft PCB to a converter board linked to an acquisition system. This smart steel technology is based on *Patent [102016000118077, Italy]* (Tondolo, 2016).

The sensor is only able to measure air *pressure* and *temperature* inside the hole and this is enough. Thanks to a simple application of the gas law and with a preliminary sensors calibration, these two measured quantities allow calculation of air volume variation divided by initial volume ($\Delta V/V_0$), which is something very similar to a 3-dimensional deformation; therefore it is possible to determine indirectly the longitudinal force passing through the bar at the level of section where the sensor is placed. Thanks to the low cost of this technology, it is possible to hand out sensors in a very high number of points inside the reinforced concrete structures, in order to have quasi-distributed measurements along steel bars; this allows a control over deformations and internal actions development in the structural elements. In Chapter 4 the system will be tested in a RC beam subjected to a four-point bending test. (Tondolo, 2018)

Chapter 2

2. Numerical study

Different numerical models of reinforcement bar are realised by means of the software ADINA 9.4 in order to simulate S3 system functioning and to study the steel bar's mechanical behaviour, as it is influenced by the cavity. This software runs numerical analysis according to the Finite Elements Method. This method is very beneficial to obtain cinematic and static solutions in situations, which can't be interpreted as a simple analytical case, because of a complex three-dimensional state of stress and strain. The body is discretized into small 3D elements, that are defined by a certain number of nodes: the parametric generation of all nodes and elements for the 3D models is obtained by writing a script in MATLAB 2018a.

The first model is an eighth of a $\Phi 20$ steel bar, the second one is an eighth of a $\Phi 20$ steel bar with an eighth of a simplified cavity drilled through it and the last one is a quarter of a $\Phi 20$ steel bar with a quarter of a more realistic cavity drilled through it. All the models are subject to a longitudinal displacement uniformly applied to one extremity face. Only a portion of the solid is represented thanks to symmetry reasons related to the geometry of the problems: appropriate supports are defined to recreate symmetry conditions inside the models.

The last model is calibrated on the basis of experimental data given by a previous testing campaign (Tondolo, 2018) and this allows to do various simulations by changing the original features. Different cases are considered by varying the steel constitutive law's characteristics in order to do a sensitivity analysis and to understand the best relation to define; in Chapter 3 these numerical results will be shown and compared to the experimental results.

2.1 Parametric generation of 3D elements

The output consists of a matrix of nodes and matrixes of elements, one for each different element group to be defined in the software. The matrix of nodes has 4 columns and as many rows as the nodes generated: the first column value represents the node number, while the other three columns are the spatial coordinates (x, y, z) of the node. The dimensions are in mm and the coordinate system centre is positioned at the edge of the bar.

1	0.0	0.0	0.0
2	0.0	0.9	0.0
3	0.0	1.8	0.0
N	x	y	z

The matrix of elements has 9 columns and as many rows as the 3D elements generated: the first column value represents the element number, while the other eight columns are numbers referred to the nodes, which compose the 8-nodes 3D solid element. It is important to follow the exact order of nodes during element definition. The three-dimensional (3D) solid element is a variable 4- to 20-node or a 21- or 27-node isoparametric element applicable to general 3D analysis and for computational reasons the 8-nodes element is used in the following models. The 3D solid element should be employed in analyses in which the three-dimensional state of strain is required, as in this case. The elements usually used are isoparametric displacement-based finite elements.

1	1	2	13	12	114	115	126	125
2	2	3	14	13	115	116	127	126
3	3	4	15	14	116	117	128	127
N	N1	N2	N3	N4	N5	N6	N7	N8

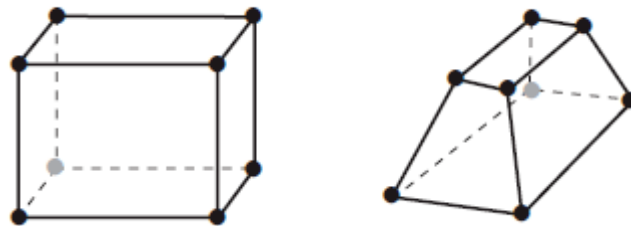


Fig. 22: 8-nodes 3D elements

Other two kinds of 3D solid elements should be necessary; the first one is the 6-nodes element and it is always defined in the same matrix with second and fourth columns having same node number, fifth and eighth as well. It is like having an 8-nodes element, where two couple of nodes are collapsed in two nodes.

66	43	86	87	43	156	199	200	156
N	N1	N2	N3	N1	N4	N5	N6	N4

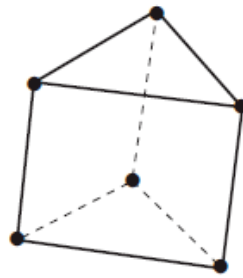


Fig. 23: 6-nodes 3D element

The other one is a tetrahedral (4-nodes) element, which is used in zones, where it is fundamental to use transition elements, because of geometric reasons or mesh size changes. In this second case, the element is defined only by five columns, element number and four nodes, while the other four remain blank. This situation definition is incomplete for the software and so it is necessary to write the script in order to have another output, a vector of element numbers, which suggests which are the tetrahedral elements. Then, I manually add this information ("Element Data > Tetrahedron Flag > Yes") in correspondence with these elements.

4516	5096	5184	5385	5107	0	0	0	0
N	N1	N2	N3	N4	-	-	-	-

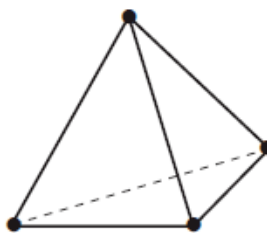


Fig. 24: 4-nodes 3D element

At the beginning of the script, there are some lines where the input data of the model must be inserted, within a certain range of values. The parameters of the models are:

Hh = hole height
R = steel bar radius
nL = number of longitudinal subdivisions (z-axis)
HL1 = hole longitudinal dimension (z-axis)
HL2 = hole transverse dimension (x-axis)
L = steel bar length

2.2 Constitutive Law of B450C steel

The models represent a B450C steel bar in some different cases; the material characteristics are always the same for the first two model, while they are varied for the last one in order to do the sensitivity analysis. It is necessary to determine a reference constitutive law. One $\Phi 20$ B450C steel bar is tested in tension under displacement control with an universal testing machine with capacity of 600 kN: the results are presented below.

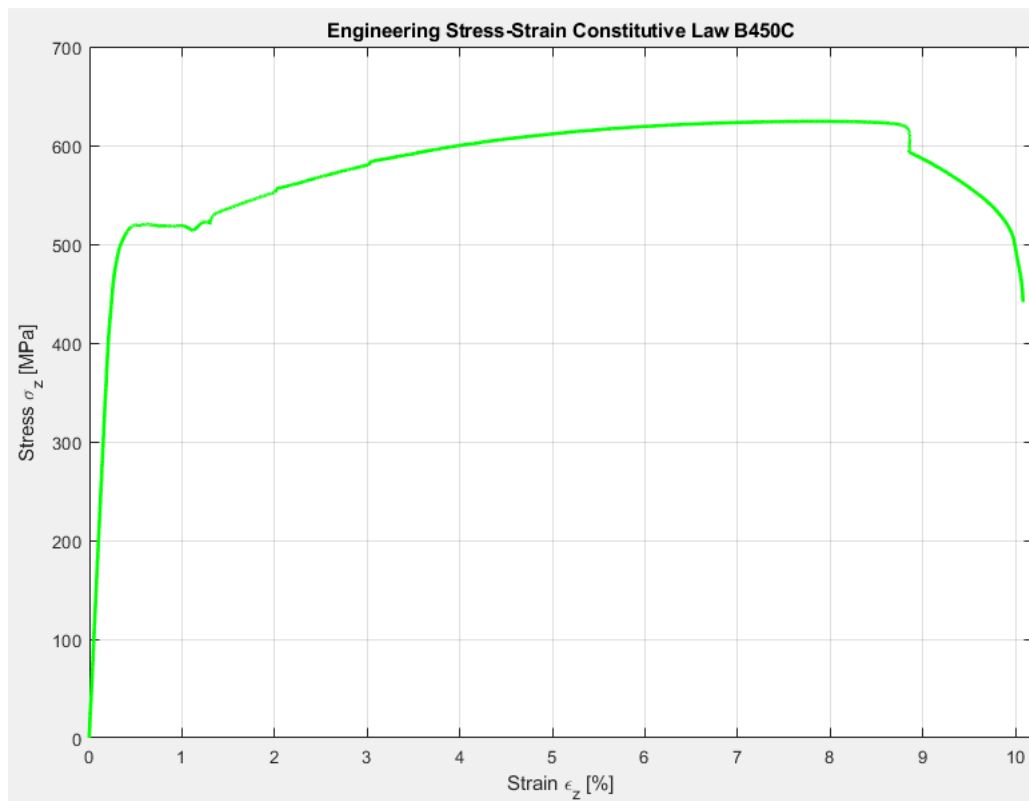


Fig. 25: Engineering stress-strain B450C

The graph represents the relation between engineering stress and strain, measured during the tensile test; these values are not so representative, because they are affected by steel necking due to a large concentration of strain localized in a small region of the bar. In order to avoid this affection, true stress and true strain should be calculated from the engineering values.

$$\sigma_T = \frac{P}{A} = \frac{P}{A} \cdot \frac{A_0}{A_0} = \frac{P}{A_0} \cdot \frac{A_0}{A} = \sigma \cdot \frac{A_0}{A}$$

$$A_0 \cdot l_0 = A \cdot l$$

$$\frac{A_0}{A} = \frac{l}{l_0} = \frac{l_0 + \Delta l}{l_0} = 1 + \varepsilon$$

$$\sigma_T = \sigma \cdot (1 + \varepsilon)$$

$$\varepsilon_T = \int \frac{dl}{l} = \ln\left(\frac{l}{l_0}\right) = \ln\left(\frac{l_0 + \Delta l}{l_0}\right)$$

$$\varepsilon_T = \ln(1 + \varepsilon)$$

The new relationship between stress and strain will be used during modelling of mechanical characteristics of the steel in the FEM as the reference constitutive law and it represents in a proper way the global one-dimensional behaviour of the steel bar under consideration. In any case the material definition will be affected by mistake, because this relation will be used as a local law in models with 3-dimensional state of stress and strain. The true stress-strain constitutive law is shown below. The Poisson's ratio for transverse strain will be assumed as 0.3 .

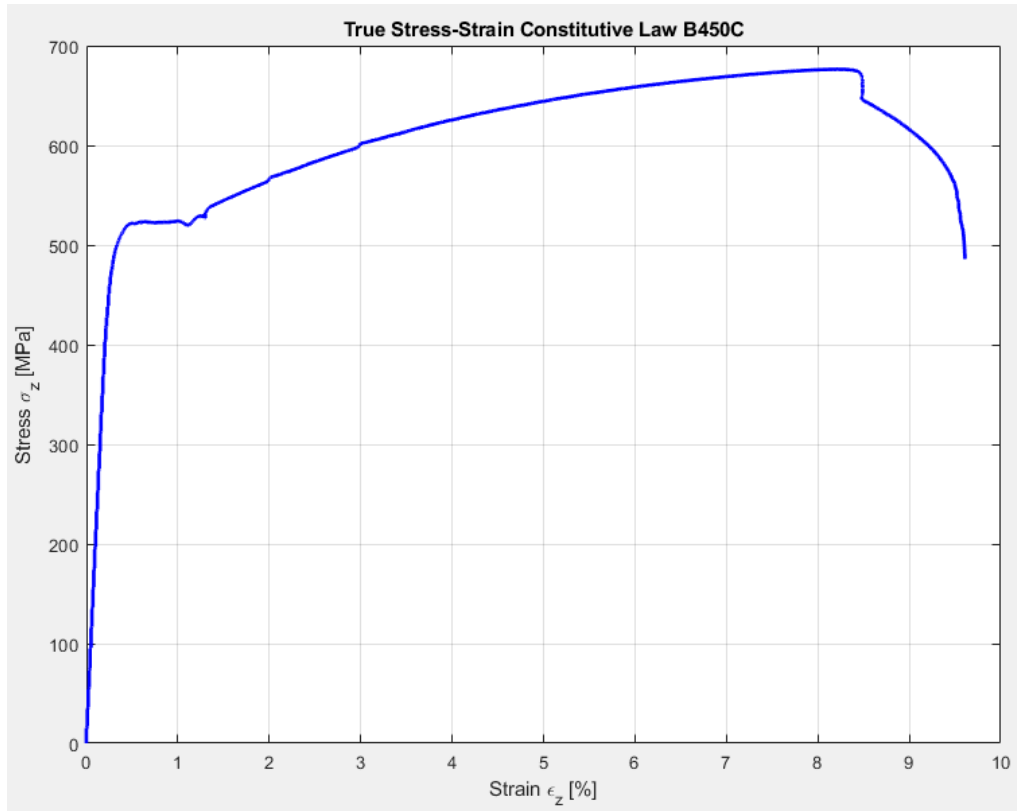


Fig. 26: True stress-strain B450C

2.3 Whole Steel Bar F.E.M. model

This first Finite Element model represents an eighth of steel bar B450C $\Phi 20$, without ribs as a simplification; this bar is subject to tension, by applying an incremental displacement at the extremities. At this step, the objective is to validate the model with the previous constitutive law, just to check if the results are compliant; in this case the stress-strain relation should be alike the law applied, because of the one-dimensional behaviour of the bar under tension.

2.3.1 Model definition

A "plastic-multilinear" material (steel) is inserted and Element Group 1 is defined as a group of "3D solid" steel elements. Then, nodes and elements matrixes are uploaded from MATLAB output and the model geometry is generated, an eighth of a cylinder with a radius of 10 mm and a total length of 10 cm, cut by three planes (XY, YZ, XZ) at the centre of the bar for symmetry reasons.

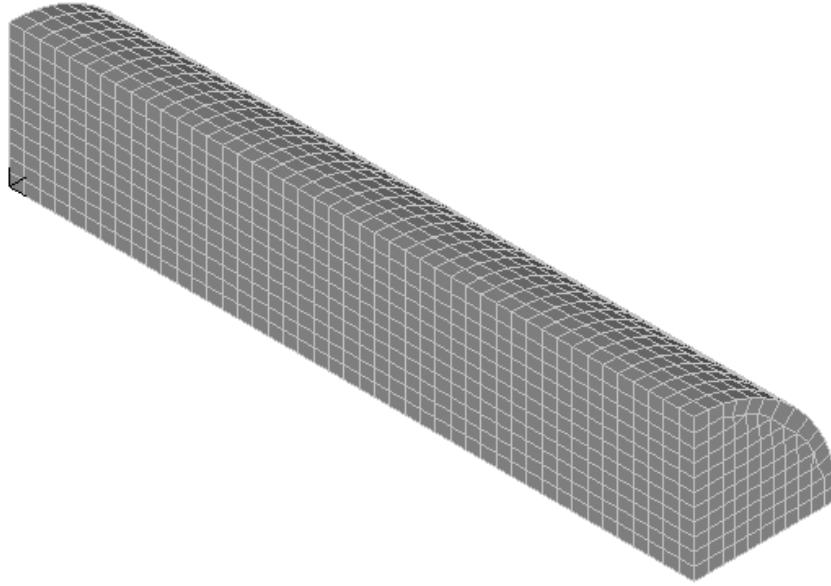


Fig. 27: Whole steel bar geometry

The boundary conditions are defined, by applying fixities on nodes: each one of the three faces generated by cutting the bar with planes have translation constrained along their respective orthogonal direction. Nodes lying on plane XY have translation along Z-axis fixed, nodes on plane YZ have translation fixed along X-axis and nodes on plane XZ have translation fixed along Y-axis. Thanks to these symmetry supports, only an eight of bar can be modelled in order to check the stress and strain development inside, having the same behaviour and reducing computational time.

An uniform displacement of 5.0 mm is applied along Z-axis in all the nodes belonging to not constrained extreme face (lying on plane XY) and a linear time function is defined with 40 time steps (5 x 0.01 , 15 x 0.05 , 20 x 0.01), in order to have a better resolution at the beginning, when the bar is in elastic range, and at the end, when post-peak behaviour is expected. Finally the software runs the F.E.M. analysis of the steel bar under displacement control with convergence criteria based on energy and force.

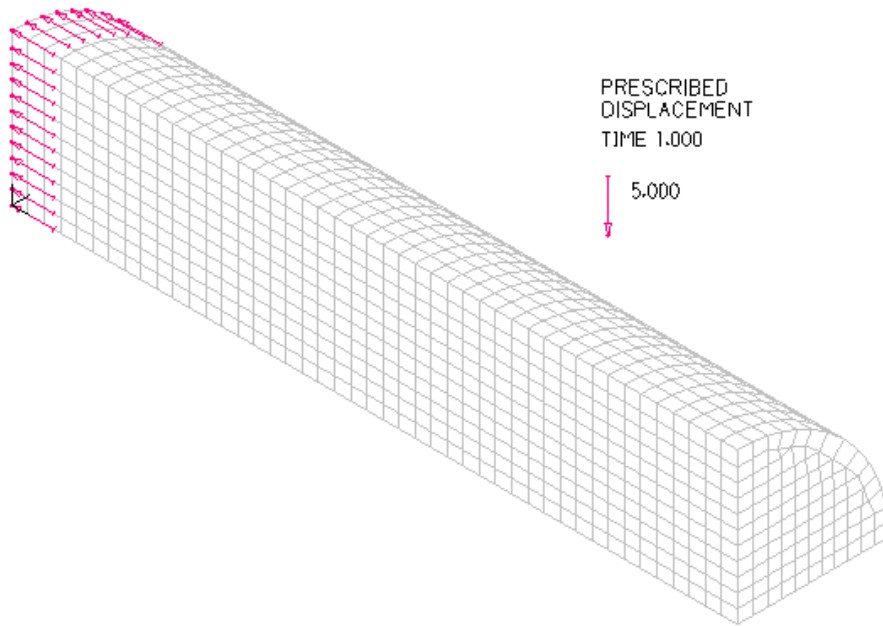


Fig. 28: Whole steel bar - applied displacement

2.3.2 Deformed shape

Here the deformed element is represented at the last step of displacement applied. The first picture represents its axonometric projection, while the other two projections (on plane XY and XZ) show the comparison between deformed (light blue) and non-deformed (violet) element. We can see circumferential contraction and longitudinal elongation of the bar due to tension obtained by displacement application. The pictures are not to scale.

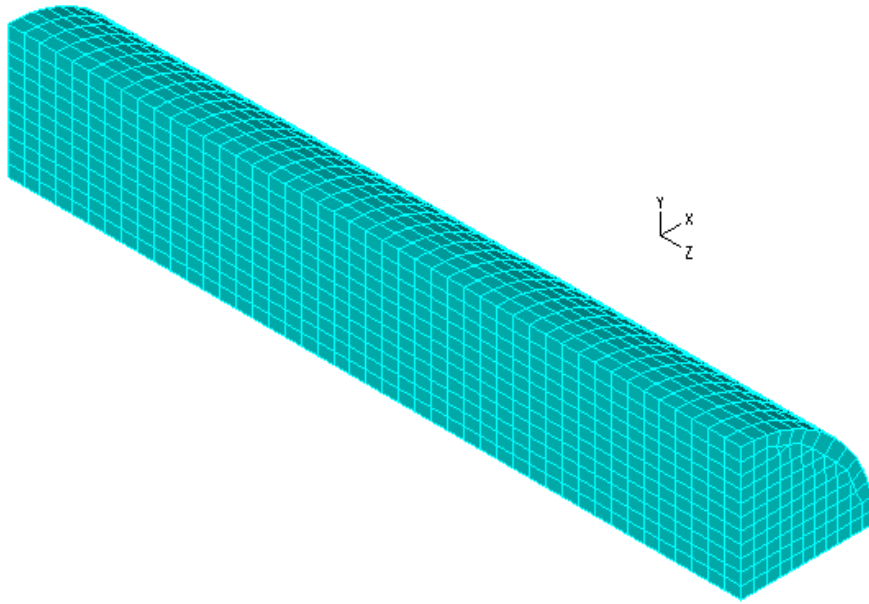


Fig. 29: Deformed whole steel bar axonometric projection

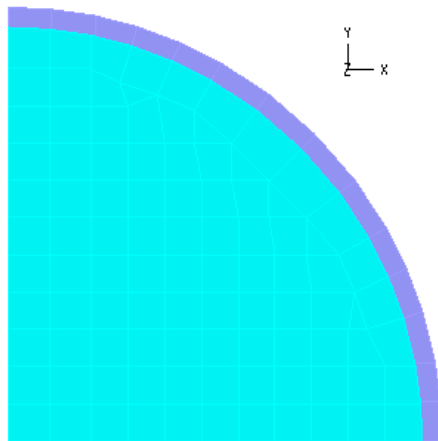


Fig. 30: Deformed whole steel bar orthogonal projection (XY)

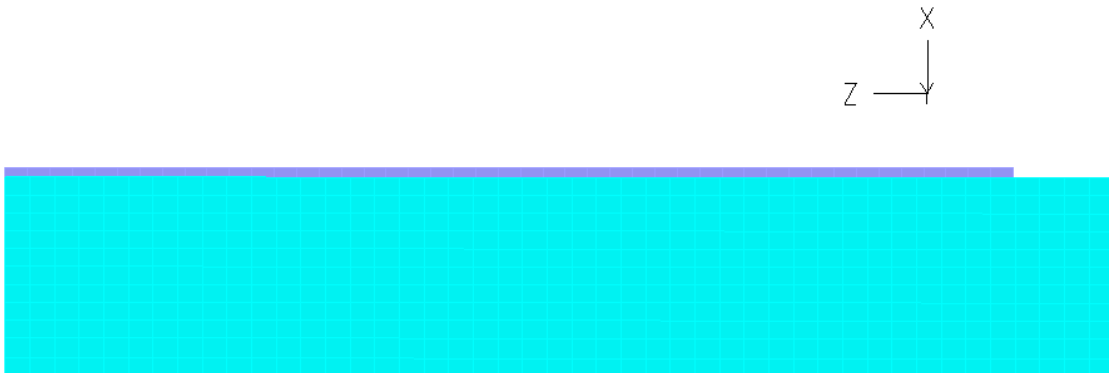


Fig. 31: Deformed whole steel bar orthogonal projection (XZ)

2.3.3 Constitutive law and FEM model behaviour

Under displacement control we get stress-strain relationship from unloaded situation to maximum strain, about 10 %; these data are taken from one random point in the model, since there is an homogeneous state of longitudinal stress and strain in the whole bar. This curve is represented in the same graph where true stress-strain constitutive law of steel B450C is plotted and so we can compare the material law with FEM response in one-directional state of stress along Z-axis. The comparison shows a quasi-perfect correspondence between two curves and this proves that material properties are inserted correctly in the model. The model seems to have a little bit longer hardening curve and at the end the FEM analysis stops because of excessive distortion of 3D solid elements. Focusing on the elastic branch, it is possible to observe that model follows properly the trend given by the constitutive law; there is also a good matching of the curves on the yielding and hardening zone.

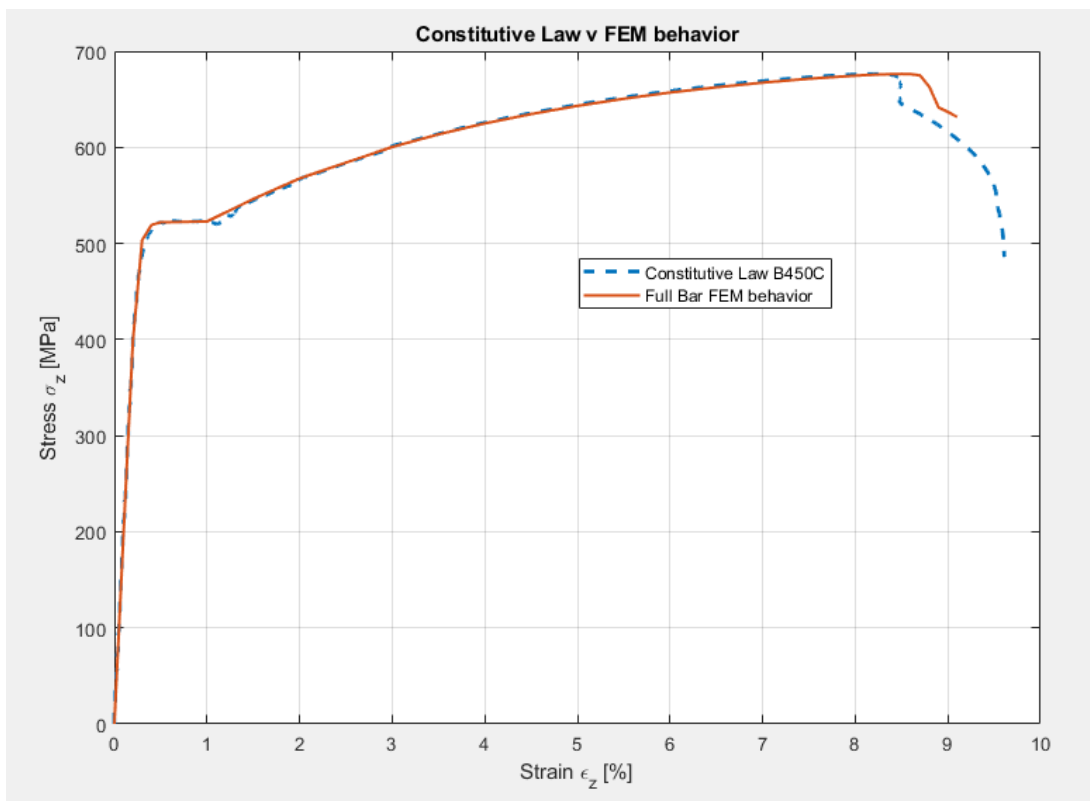


Fig. 32: Constitutive law and FEM behaviour

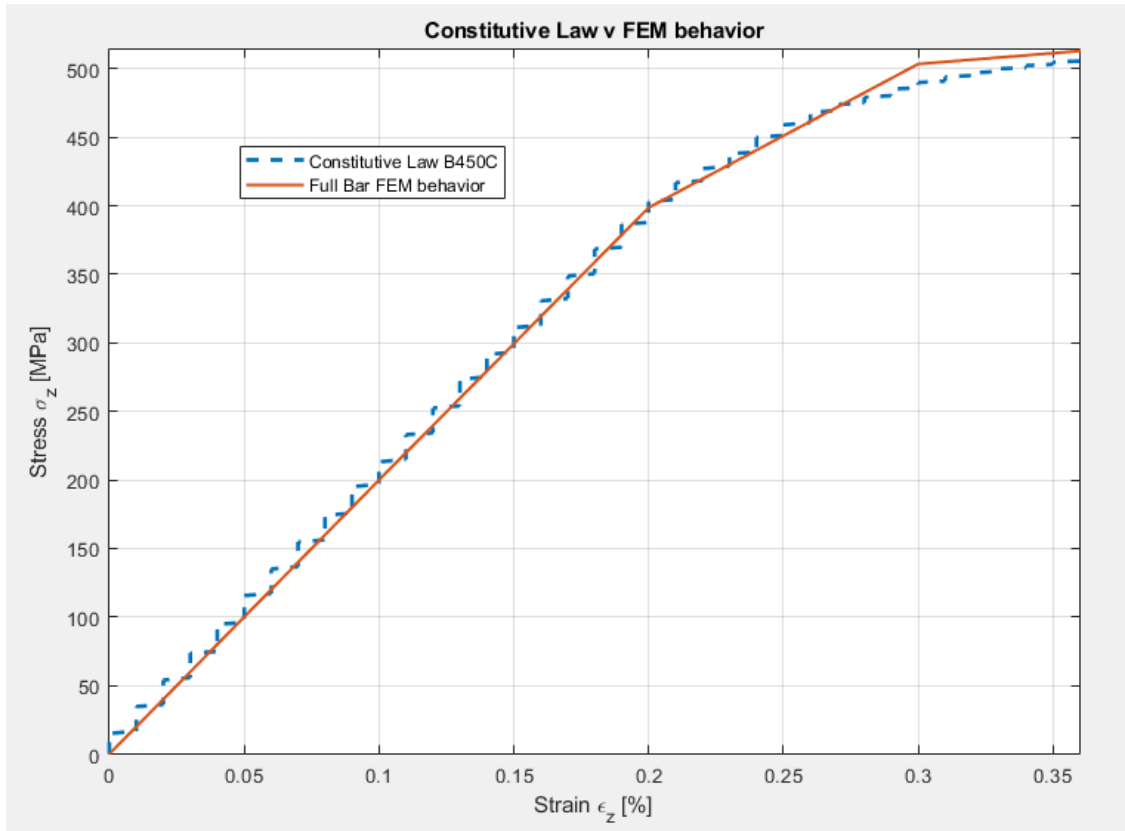


Fig. 33: Constitutive law and FEM behaviour - focus on elastic branch

2.4 One-eighth of Smart Steel Bar FEM model

This Finite Element Method model represents an eighth of steel bar B450C $\Phi 20$, without ribs, but with a simplified drilled cavity containing air; this bar is subject to tension, by applying an incremental displacement at the edge.

This is a first attempt to represent with good approximation the mechanical behaviour of the steel bar instrumented with S3 system, even if this is still a simplified model. The results obtained by this analysis are really interesting to study the relationship between pressure changes and volumetric deformations of the air and to quantify the influence of the non-deformable elements inside the cavity.

2.4.1 Cavity geometry

Smart steel bar has a transversal cylindrical drilled hole, where barometric sensor and hard PCB are embedded. The cylinder has its main dimension along Y-axis, while the bar has its own along longitudinal direction Z. In this paper, S3 system is applied on a steel bar B450C $\Phi 20$ with same constitutive law seen before. In this case the air cavity has a diameter of 4 mm and an height of 15.5 mm, therefore its volume is around 194.7 mm^3 , without considering volume occupied

by electronic instrumentation. The hole is included among a steel layer 1 mm thick at the bottom and the electrical feed-through at the top, occupying a cylindrical zone 3.5 mm thick with a 6 mm diameter; this closing portion is something like a discontinuity for stress and strain state, but it won't be studied in details in this paper and it will modelled in some simplified ways.

In the following drawings, a whole smart steel bar, an half and an eighth are shown, highlighting the hole geometry; electrical feed-through portion is coloured with red, without going deeper in its features. Pictures are not to scale and dimensions are in mm.

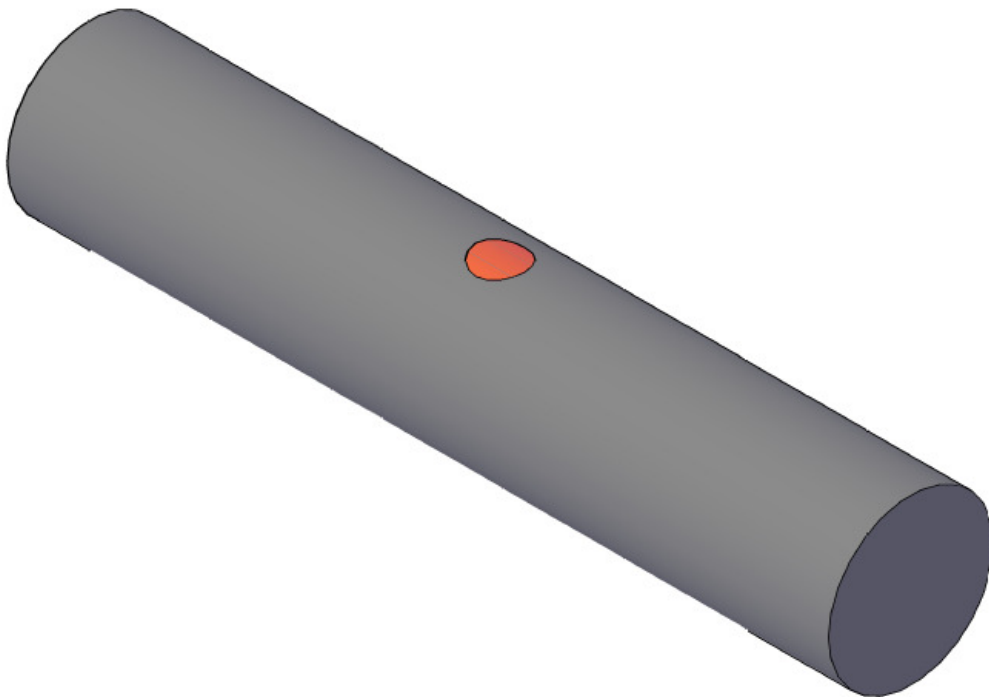


Fig. 34: $\Phi 20$ Smart Steel Bar 10 cm long

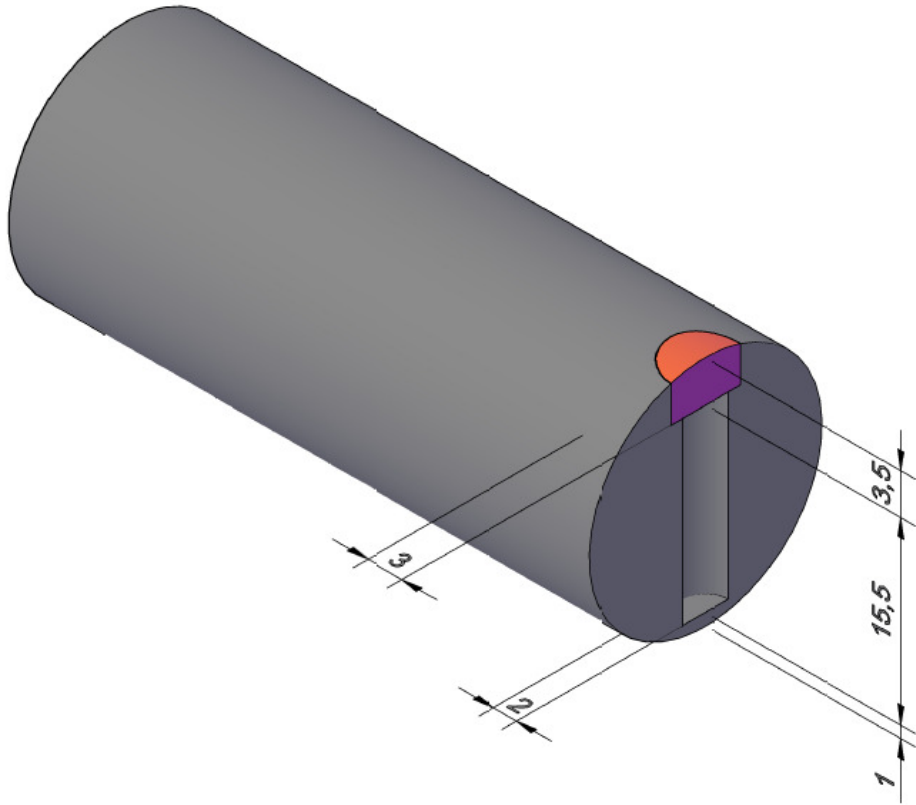


Fig. 35: Half of $\Phi 20$ Smart Steel Bar

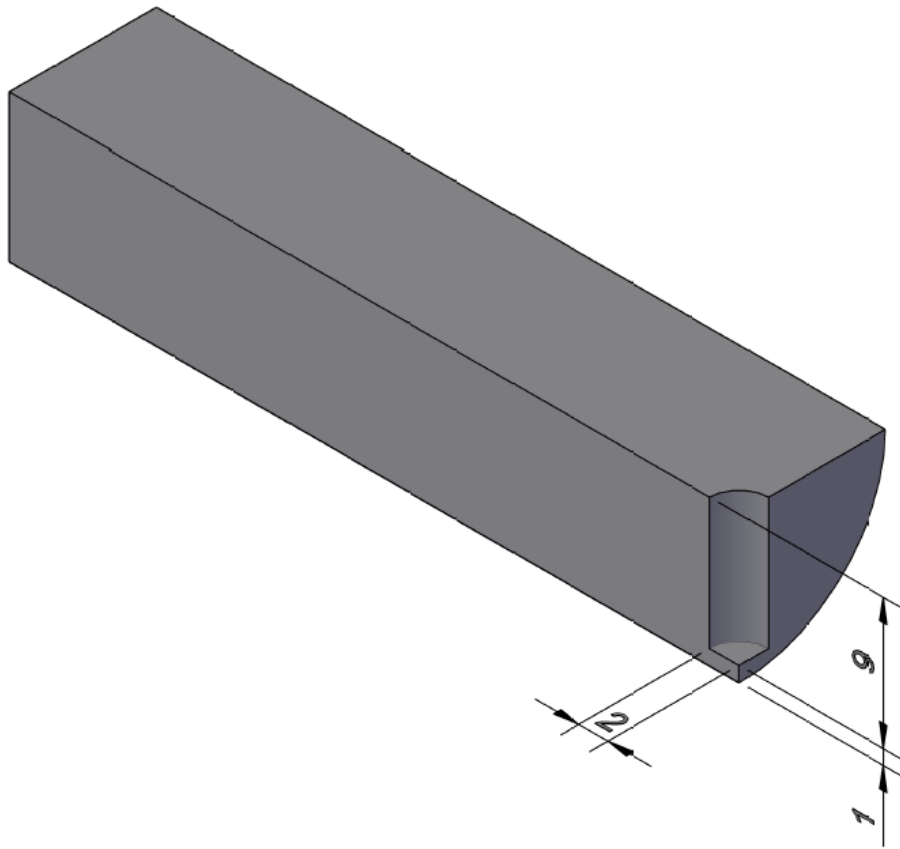


Fig. 36: An eighth of $\Phi 20$ Smart Steel Bar (lower part)

2.4.2 Steel bar definition

The hole geometry is defined as symmetrical in relation to Z-axis as a simplification: in this FEM model, air cavity is represented by an eighth of cylinder with a diameter of 4 mm and an height of 18 mm, while the upper steel layer is 1 mm thick. These dimensions are realistic for the lower part of the cavity, although they are not so representative for the top part, closed by the electrical feed-through; this portion has its own complex geometry and it also reduces air cavity volume. In this case, air volume in one-eighth-bar model is 27.3 mm^3 , while air occupies 218.4 mm^3 in the entire cylindrical cavity.

A "plastic-multilinear" material (steel) is inserted and Element Group 1 is defined as a group of "3D solid" steel elements. Nodes and elements matrixes are uploaded from MATLAB output in order to generate the model geometry, an eighth of steel bar with a length of 10 cm and a diameter of 20 mm, cut for symmetry reasons by three planes as done before. The cavity stands at the middle of the bar, so at the edge of one-eighth-bar model.

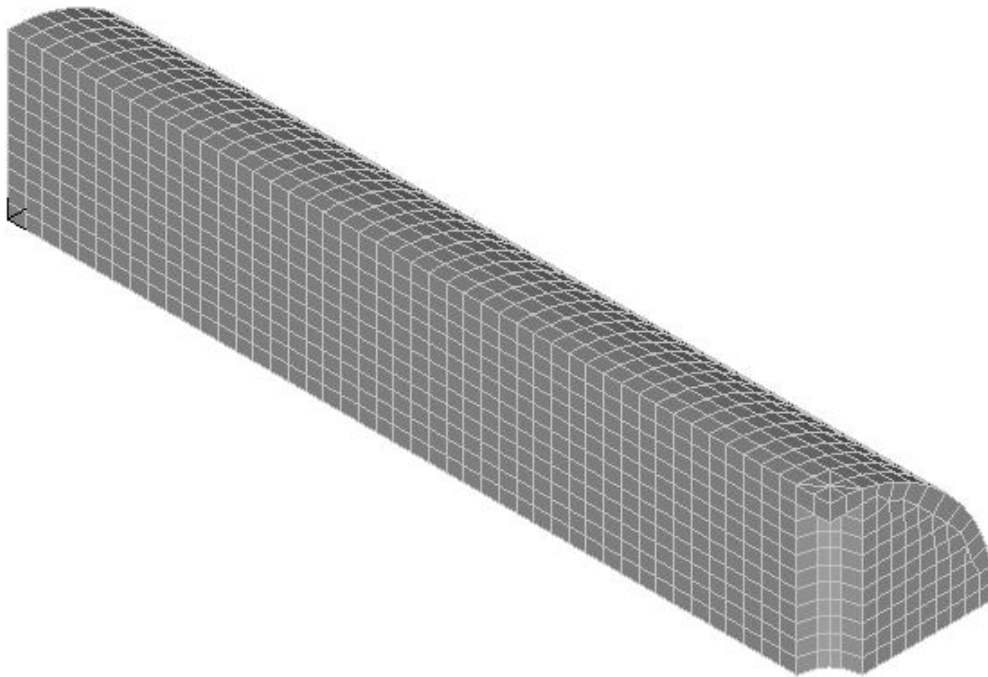


Fig. 37: One-eighth steel bar (EG1) geometry

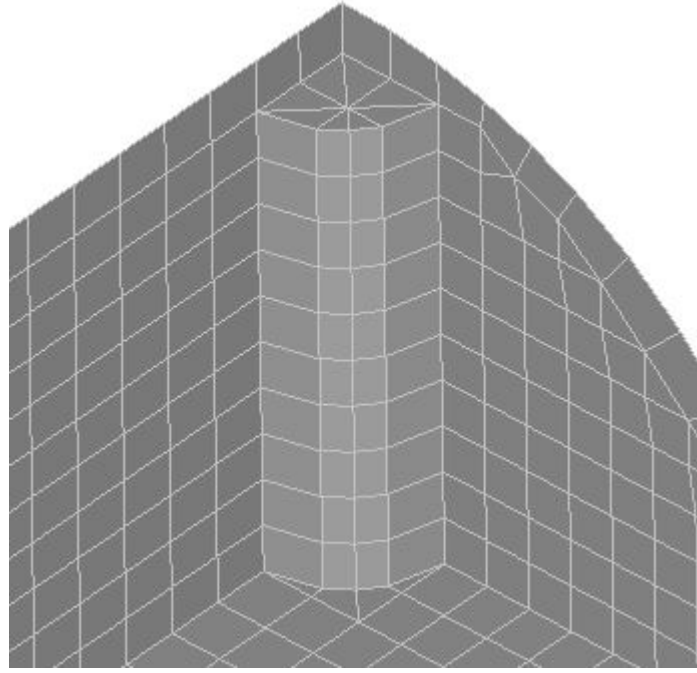


Fig. 38: One-eighth steel bar (EG1) geometry - detail

2.4.3 Air cavity definition

The fluid inside the cavity is air and its compressibility characteristics are related to the bulk modulus, which gives the relation between volume deformation and pressure variation inside the hole without considering temperature change; this factor depends on initial conditions, air composition and kind of physical transformation, but in typical situations its order of magnitude is 10^2 kPa , so around 6 orders below steel Young's modulus (around 200 GPa). It means that the air is not really able to give a contribution in terms of strength and so the real value of this term is not so important, as we will see later in details. The fluid is defined with a bulk modulus of 142 kPa and a density of 1.2 kg/m^3 .

Element Group 2 is defined as group of "3D fluid" air elements and then nodes and elements matrixes are uploaded from MATLAB output in order to generate the fluid model, an eighth of air cylinder with an height of 18 mm and a diameter of 4 mm, cut for symmetry reasons by three planes as done before. This fluid cylinder fits in the cavity left by the steel bar model and the two elements group share the nodes located along the interface between them; in this way the software will deform air cavity volume in function of the steel bar strain state, thanks to fluid-structure interface connection. The other three faces are automatically restrained by boundary conditions alike the ones applied on neighbour faces.

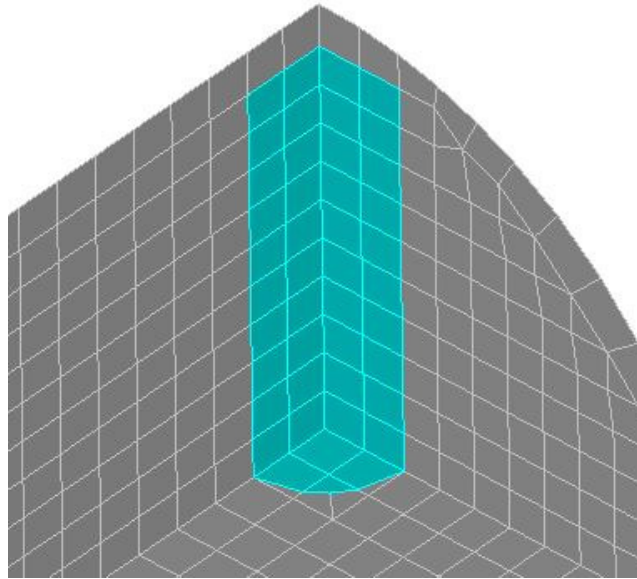


Fig. 39: One-eighth steel bar (complete model) geometry - detail

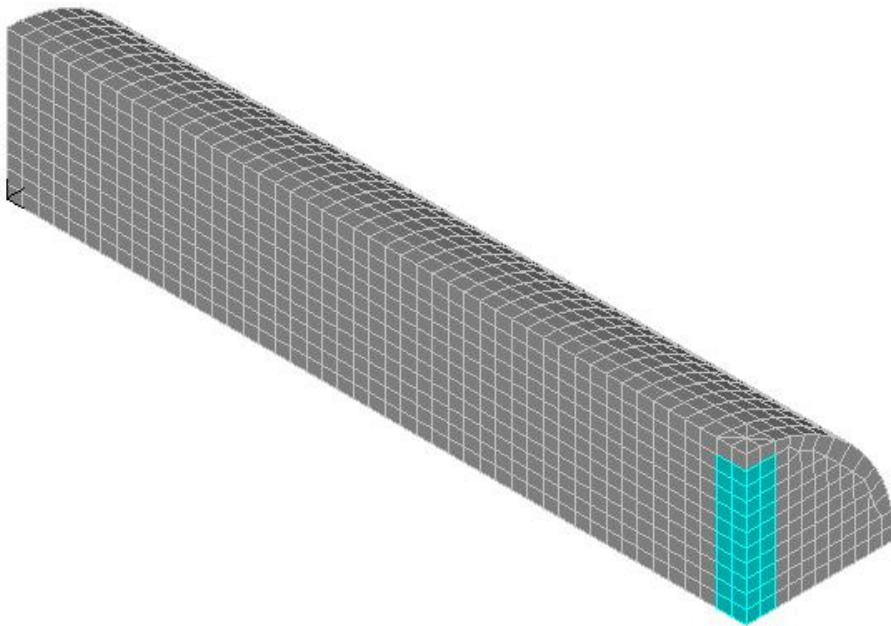


Fig. 40: One-eighth steel bar (complete model) geometry

2.4.4 Complete model definition

Boundary conditions are defined, by applying fixities on nodes: each one of the three faces generated by cutting the bar with planes have translation constrained along their respective orthogonal direction. Nodes lying on plane XY have translation along Z-axis fixed, nodes on plane YZ have translation fixed along X-axis and nodes on plane XZ have translation fixed along Y-axis.

An uniform displacement of 0.28 mm is applied along Z-axis in all the nodes belonging to not constrained extreme face (lying on plane XY) and a linear time function is defined with 50 time steps (30 x 0.01, 20 x 0.035), in order to have a better resolution at the beginning, when the bar is in elastic range. Finally the software runs F.E.M. analysis of the steel bar under displacement control with convergence criteria based on energy and force.

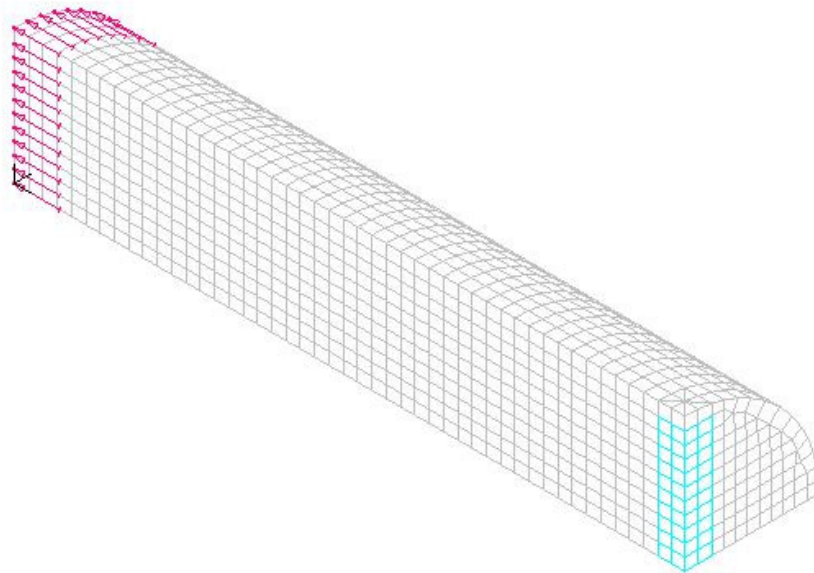


Fig. 41: One-eighth steel bar - applied displacement

2.4.5 Deformed shape

Here the deformed element is represented at the last step of displacement applied, that is 0.2702 mm; after this point, the software can't find convergence anymore. The first picture represents EG1's axonometric projection, while the other two projections (on plane XY and XZ) show the comparison between deformed (light blue) and non-deformed (violet) element, with deformed shape increase by a magnification factor of 10 to have a clearer view; the same comparison is realised in last image to show deformed shape of air volume (EG2) inside the cavity in axonometric projection. The pictures are not to scale.

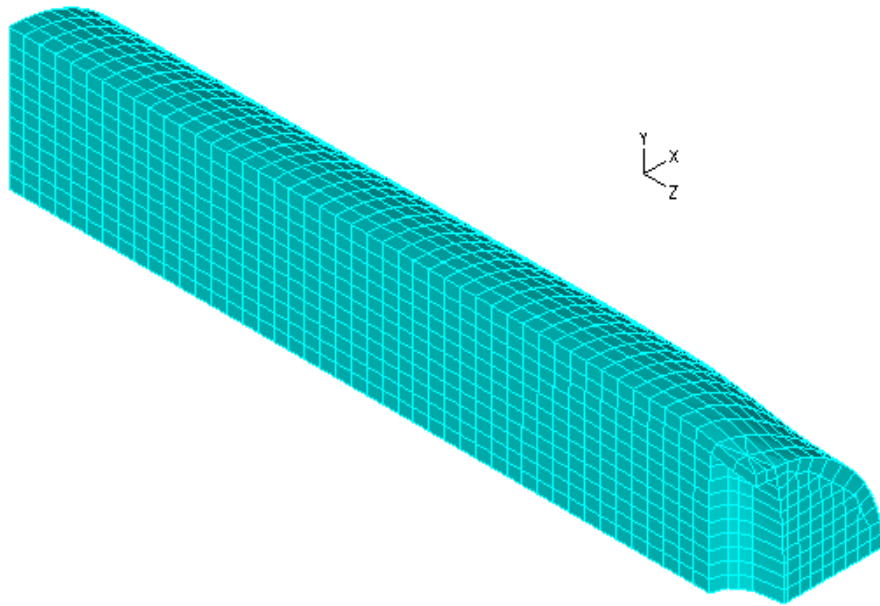


Fig. 42: Deformed one-eighth steel bar (EG1) axonometric projection

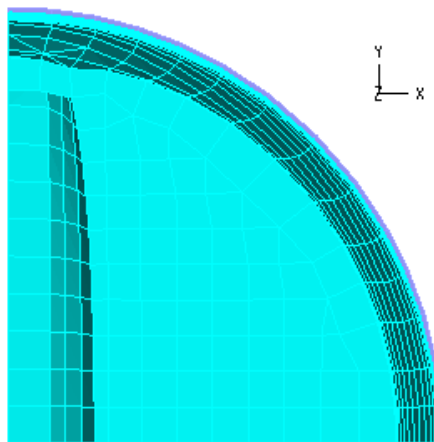


Fig. 43: Deformed one-eighth steel bar (EG1) orthogonal projection (XY)

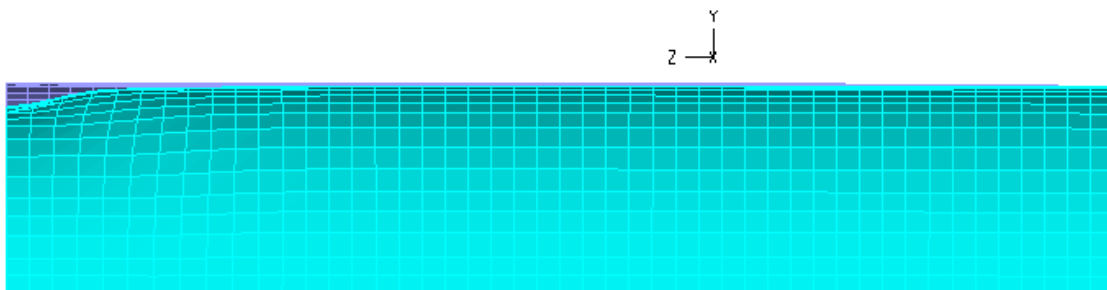


Fig. 44: Deformed one-eighth steel bar (EG1) orthogonal projection (XZ)

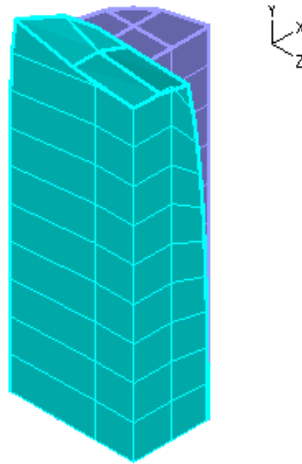


Fig. 45: Deformed one-eighth air volume (EG2) axonometric projection

2.4.6 Pressure-Volume in-depth analysis

The F.E.M. software uses a linear law to determine the pressure inside the fluid in relation to its volume reduction; the formulation gives pressure variation in function of volume variation divided by its volume and this proportionality is ruled by the bulk modulus. The value of $\Delta V/V_0$ is really interesting, because it can be compared to the values determined by the experimental campaigns and it represents a physical quantity conceptually very close to strain; looking at the pressure development in the model, it is possible to determine easily that value thanks to the bulk modulus set in the software.

$$\Delta P = \frac{\Delta V}{V_0} \times k$$

$$\text{Air Bulk Modulus: } k = 142 \text{ kPa}$$

Inside the hole, there are some non-deformable objects, which occupy some of the available cylindrical volume, where the air is contained inside; this produce a reduction of the fluid deformable volume and it is wrong to don't take it into account. A reduction of deformable volume -without any change in the hole geometry- doesn't influence the absolute volume variation ΔV , but it modifies the value $\Delta V/V_0$, because the denominator V_0 changes, and so also the pressure variation ΔP changes. It is not necessary to model the exact amount of non-deformable objects inside the hole, because the following linear formulation can be used, considering V_a as the hole volume and V_b as the hole volume minus the volume of non-deformable material contained inside.

$$\Delta P_b = \frac{V_a}{V_b} \times \Delta P_a$$

A comparison between two different situations (with and without non-deformable objects) is shown below; the results are obtained by F.E. models in order to demonstrate the formulation validity. In both the cases, a tension of 50 MPa is applied at the edge. The volume of the hole is measured on the model and in the first case this is also the volume occupied by air.

$$V_a = 27.3 \text{ mm}^3$$

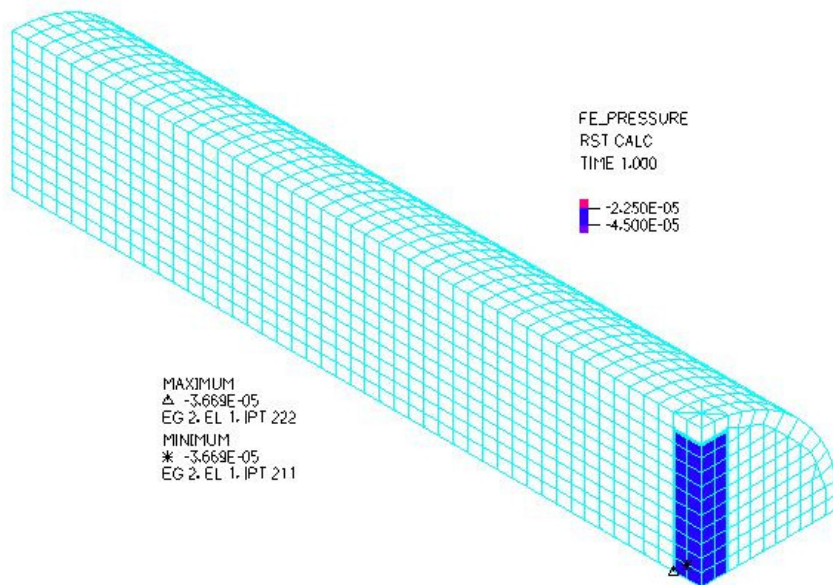


Fig. 46: One-eighth steel bar (case a) - air cavity pressure (last time step)

$$\Delta P_a = 36.7 \text{ Pa}$$

In the second case, four additional "3D solid" steel cubic elements are modelled (total volume of 3.6 mm^3); thus the available deformable volume occupied by air is reduced and so the pressure will be higher, because of an higher value of $\Delta V/V_0$.

$$V_b = 27.3 \text{ mm}^3 - 3.6 \text{ mm}^3 = 23.7 \text{ mm}^3$$

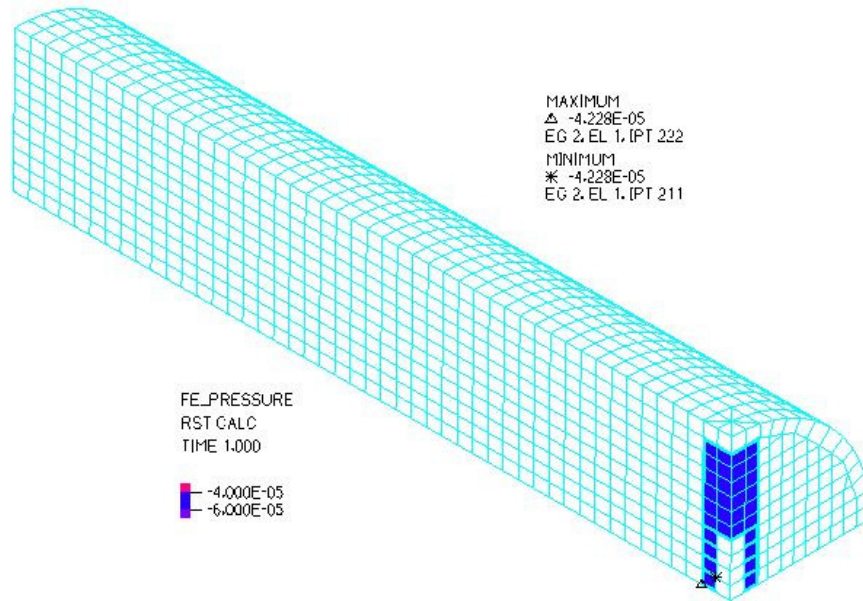


Fig. 47: One-eighth steel bar (case b) - air cavity pressure (last time step)

$$\Delta P_b = 42.3 \text{ Pa}$$

According to the previous formulation the ratio between pressure variations should be equal to the ratio between the fluid volumes and so it is. This allows a F.E.M. modelling without considering inner objects, but it is important to apply a correction to the pressure values due to this deformable volume reduction. In the example, the ratio is equal to 1.15 and this means that non-deformable elements inside the hole increase the fluid pressure of a 15%.

$$\frac{\Delta P_b}{\Delta P_a} = \frac{V_a}{V_b} = 1.15$$

2.5 One-quarter of Smart Steel Bar FEM model

This Finite Element model represents a quarter of steel bar B450C $\Phi 20$, without ribs, considering a cavity with a more realistic geometry and taking into account the space left for the electrical feed-through; this bar is subject to tension, by applying an incremental displacement at the edge.

The purpose is to simulate in a more precise way not only the mechanical behaviour of the instrumented bar, but also the S3 system functioning. The numerical results will be compared in the following chapter with experimental data obtained by a previous testing campaign.

Here it is not possible to represent only an eighth of bar, because the cavity geometry is not symmetrical with respect to plane XZ. Furthermore, the model is longer than the previous one in order to apply tension like the testing machine, where an imposed displacement is applied at the extremities, 25 cm far from the cavity. In this way, the deformed shape is compliant to the actual one.

2.5.1 Steel bar definition

The cavity geometry is defined according to the real dimensions: in this FEM model, air cavity is represented by an quarter of cylinder with a diameter of 4 mm and an height of 15.5 mm. At the bottom there is a steel layer 1 mm thick, while at the top of the air cavity, another hole is modelled in order to represent the upper portion where the feed-through is placed: this is a quarter of cylinder with a diameter of 6 mm and an height of 3.5 mm.

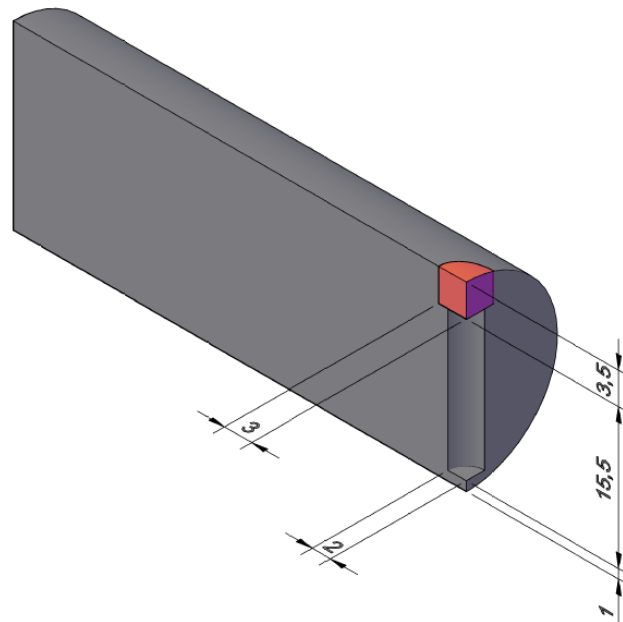


Fig. 48: A quarter of $\Phi 20$ Smart Steel Bar

The electrical feed-through is not modelled, because it doesn't give significant contribution in terms of stiffness, but this should be needed in further detailed studies. In this case, air volume in one-quarter-bar model is 51.1 mm^3 , while air occupies 204.6 mm^3 in the entire cylindrical cavity.

A "plastic-multilinear" material (steel) is inserted and Element Group 1 is defined as a group of "3D solid" steel elements: in this final model, four different constitutive laws are considered in order to define a sensitivity analysis, which will be discussed in Chapter 3. The elements are generated with an "automatic mesh" tool, after defining the geometry of the model, that is a quarter of steel bar

with a length of 50 cm and a diameter of 20 mm, cut for symmetry reasons by two planes (XY-YZ). This length allows to obtain an application of tensile axial load closer to a previous experimental campaign, which will be presented in Chapter 3. The cavity stands at the middle of the bar, so at the edge of one-quarter-bar models.

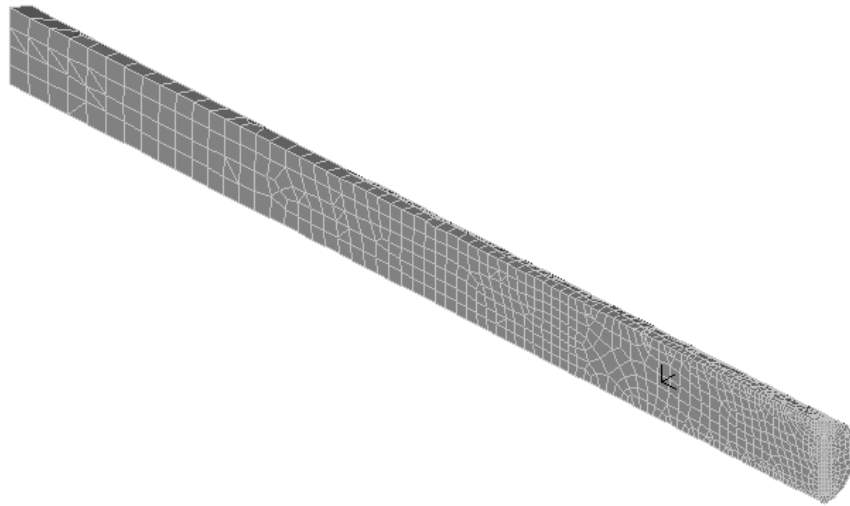


Fig. 49: One-quarter steel bar (EG1) geometry

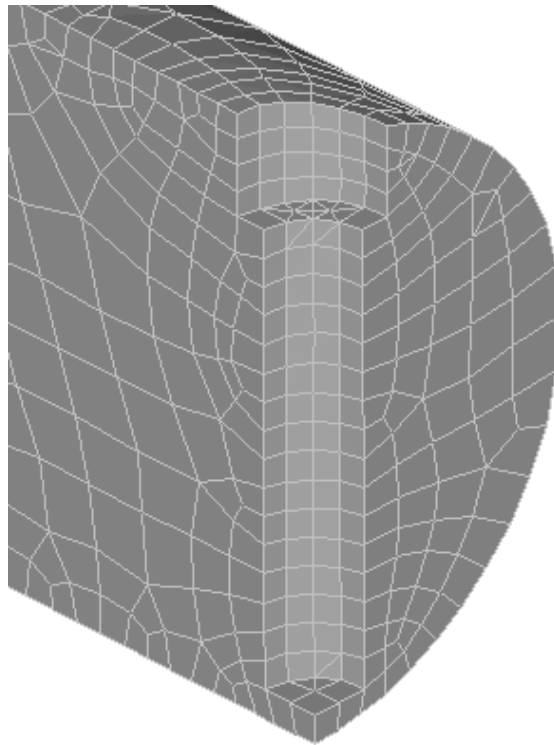


Fig. 50: One-quarter steel bar (EG1) geometry - detail

2.5.2 Air cavity definition

The fluid inside the cavity is air and it is defined with a bulk modulus of 142 kPa and a density of 1.2 kg/m^3 . Element Group 2 is defined as group of "3D fluid" elements and then elements composing the fluid model are generated, a quarter of air cylinder with an height of 15.5 mm and a diameter of 4 mm, cut for symmetry reasons by two planes as done before. This fluid cylinder fits in the lower cavity left by the steel bar model and the two elements group share the nodes located along the interfaces between them; the other two vertical faces are automatically restrained by boundary conditions alike the ones applied on neighbour faces, while the top face is closed by a thin cap, realised of "3D solid" elements (Element Group 3) and made of an elastic material with low stiffness (3 GPa). This is used to simulate the closing contribution given by the feed-through element, but without giving additional stiffness to the drilled portion.

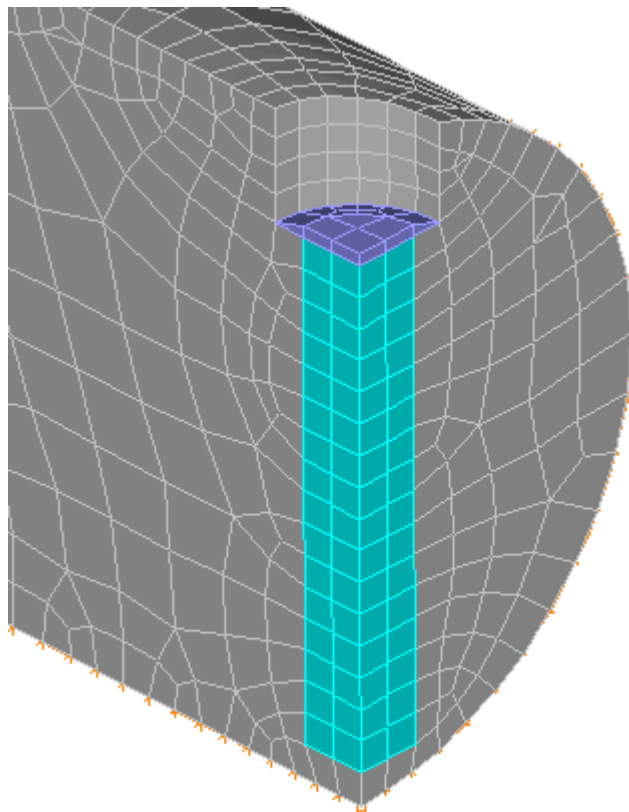


Fig. 51: One-quarter steel bar (complete model) geometry - detail

2.5.3 Complete model definition

Boundary conditions are defined by applying fixities on nodes: each one of the two faces generated by cutting the bar with planes have translation constrained along their respective orthogonal direction. Nodes lying on plane XY have translation along Z-axis fixed and nodes on plane YZ have translation fixed along X-axis.

An uniform displacement is applied along Z-axis in all the nodes belonging to not constrained extreme face (lying on plane XY) and a linear time function is defined with different time steps, in order to have a better resolution at the beginning and at the end, when the bar is in elastic range and then next to non-convergence point. Finally the software runs F.E.M. analysis of the steel bar under displacement control with convergence criteria based on energy and force.

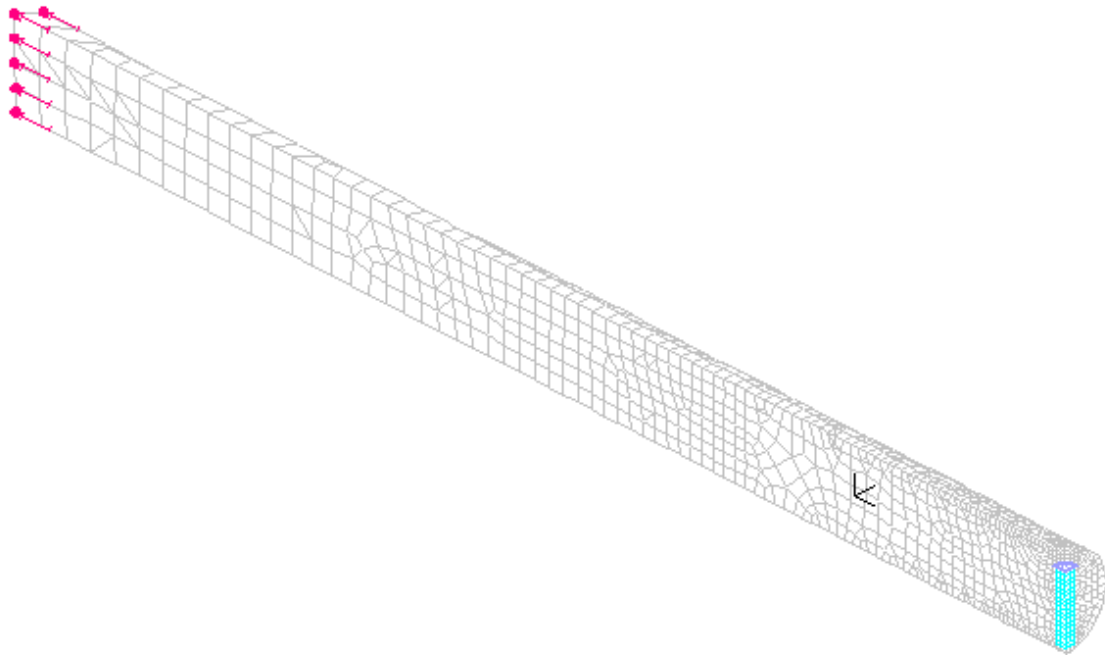


Fig. 52: One-quarter steel bar - applied displacement

2.5.4 Deformed shape

Here the deformed element is represented at the last step of displacement applied, that is 0.8918 mm in the case with the original constitutive law used for previous models too. The first picture represents EG1's axonometric projection, while the other two projections (on plane XY and XZ) show the comparison between deformed (light blue) and non-deformed (violet) element, with deformed shape increase by a magnification factor of 10 to have a clearer view. The same comparison is realised in last image to show deformed shape of air volume (EG2)

inside the cavity in axonometric projection; this shape looks like strange because of a bad rendering of 3d-fluid elements, but it represents in a proper way the outline of deformed air volume with thick line. The pictures are not to scale.

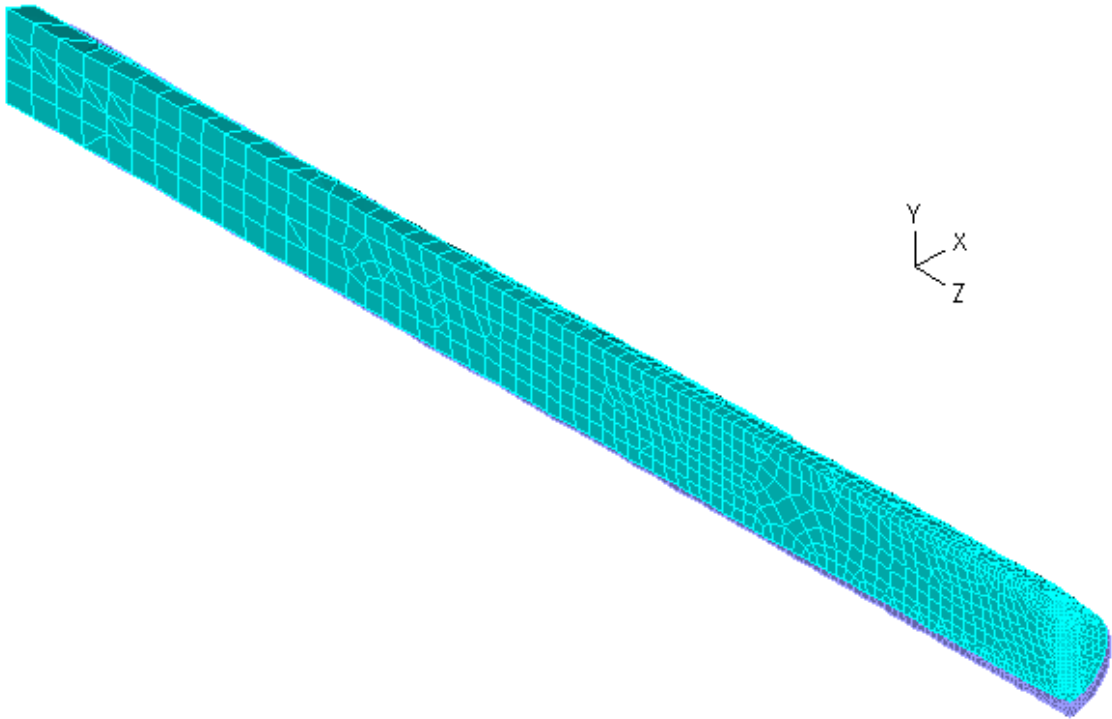


Fig. 53: Deformed one-quarter steel bar (EG1) axonometric projection

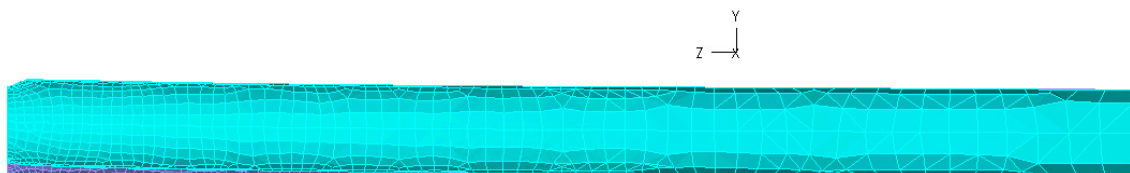


Fig. 54: Deformed one-quarter steel bar (EG1) orthogonal projection (XZ)

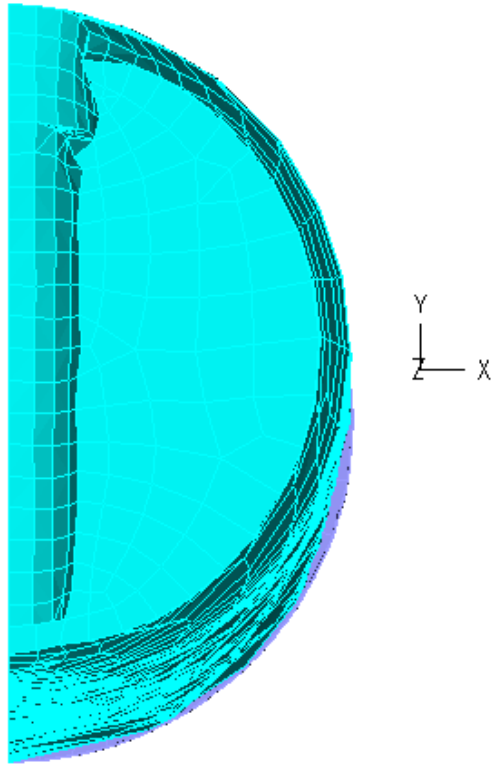


Fig. 55: Deformed one-quarter steel bar (EG1) orthogonal projection (XY)

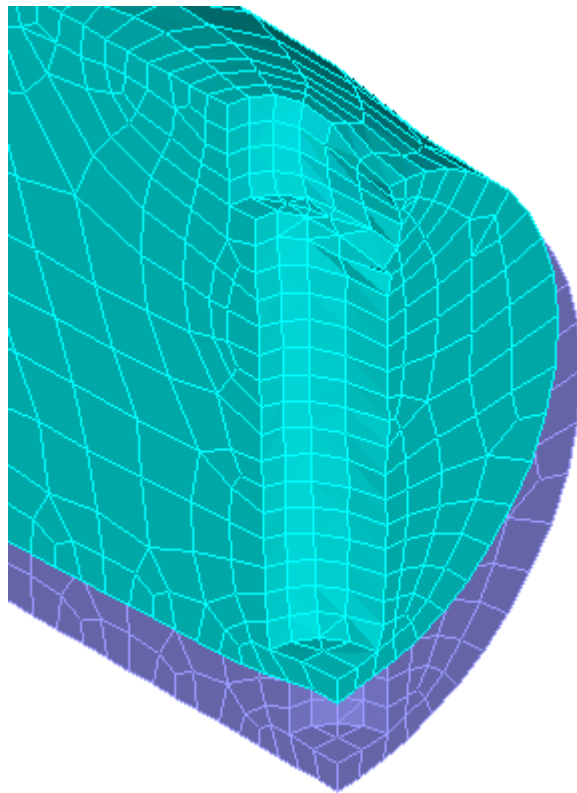


Fig. 56: Deformed one-quarter steel bar (EG1) axonometric projection - detail

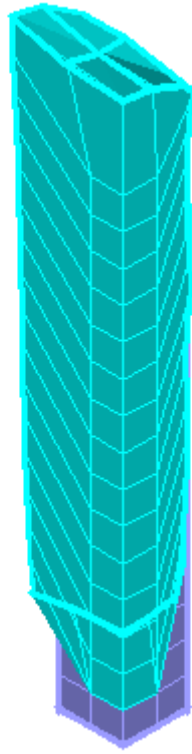


Fig. 57: Deformed one-quarter air volume (EG2) axonometric projection

Chapter 3

3. Comparison with previous studies

3.1 Previous experimental campaign on S3 system

As it is described in a previous paper (Tondolo, 2018), some tests were performed on a $\Phi 20$ smart steel bar equipped with three S3 system's sensors placed with a spacing of 80 mm (S_1 , S_2 and S_3). The measurement unit is contained in transversal cylindrical hole with a diameter of 4 mm, closed at the top by an electrical feed-through: cavity's geometry is described in details in Chapter 2. In addition, a longitudinal groove is realised into the bar in order to host soft PCB, which links hard PCB inside the cavity with Converter Board. The digital pressure and temperature data sensed by embedded sensors are transferred to the CB and they are transformed into analogue continuous voltage signals, recorded by HBM Spider8 acquisition system.

3.1.1 Theoretical basis

The new smart idea behind S3 system is extremely simple: an embedded low-cost sensor measures pressure and temperature of the air inside a cavity drilled through a steel bar, in order to sense the deformation in a certain section. The theoretical formulations are reduced only to one of the most known physical law in thermodynamics: the *General Gas Equation*, formulated in 1834 by Clapeyron.

$$pV = nRT$$

Low-cost transducers have the capability to measure pressure and temperature variations of the air with good sensitivity; thanks to the previous law, it is possible to determine easily the variation of air cavity volume divided by initial volume $\Delta V/V_0$, that is a *deformation* in all respects.

$$\frac{\Delta V}{V_0} = \left(1 + \frac{\Delta T}{T_0}\right) / \left(1 + \frac{\Delta p}{p_0}\right) - 1$$

This volumetric deformation is mainly the mirror of mechanical and thermal strains in the steel bar. The mechanical contribution is depending proportionally on the force ΔF applied to the bar and this is valid within elastic range and in case of axial load, but it's not true anymore when plasticisation begins; the other contribution is function of environmental temperature variation ΔT^* , which generally is not equal to ΔT , the temperature variation of the air in the cavity.

$$\frac{\Delta V}{V_0} = \left(\frac{\Delta V}{V_0}\right)_{\Delta F} + \left(\frac{\Delta V}{V_0}\right)_{\Delta T^*}$$

So the first thing to do is a thermal calibration test for each measurement unit in order to know in each moment the quantity of volumetric deformation due to the environmental temperature, which the bar is exposed to. Then thanks to mechanical test, the relation between this deformation and the force applied to the steel bar is determined; this allows to know which tensile force is passing through the reinforcement only by measuring two simple physical quantities like pressure and temperature of air inside a cavity drilled through the bar.

3.1.2 Thermal calibration tests

Firstly the smart steel bar is subject to wide temperature variations without any load applied in order to understand the influence of this physical quantity on $\Delta V/V_0$ and so the system can be calibrated. The tests are performed into a temperature controlled chamber, where different cycles of slow temperature variations are applied to the bar with a range of values between 14.5°C and 41.5°C. Starting from pressure and temperature data, a different experimental relation between ΔT^* and $\Delta V/V_0$ is determined for each sensor; this means that S3 system always needs this kind of preliminary compensation, because at the present stage of development there is not an universal relation valid a priori and each measurement unit has its specific behaviour.

$$\left(\frac{\Delta V}{V_0}\right)_{\Delta T^*} = \left.\frac{\Delta V}{V_0}\right|_{\Delta F=0} = f(\Delta T^*)$$

These experimental relations are interpolated by cubic functions, which reveal a nonlinear and monotonically decreasing trend. The reason why the trend is decreasing needs further studies in order to give an explanation: this is probably due to the complexity of thermo-mechanical behaviour of all the components that

are part of the measurement system, in particular the sensor, the steel bar and the feed-through. Although this is a counterintuitive result, these relations are necessary to compensate environmental temperature influence over the readings.

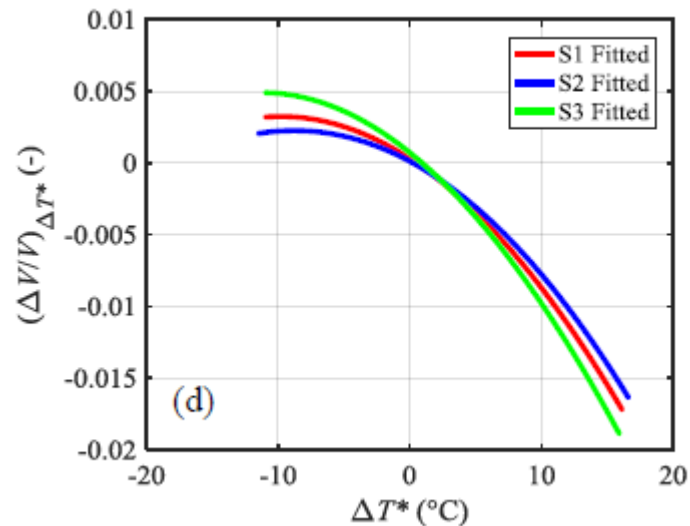


Fig. 58: Thermal compensation: determination of the $f(\cdot)$ relation between ΔT^* and $(\Delta V/V)\Delta T^*$, through fitting the experimental data obtained in a temperature controlled environment, for the three sensors

3.1.3 Axial tensile tests

The same smart steel bar is then tested under uniaxial tensile load, applied by a MTS 250 testing machine in uncontrolled thermal conditions. Since area of transversal section at the level of the hole is reduced by 24% compared to the nominal area and stress concentration factor around the cavity could be around 3, the maximum load applied is 40 kN, in order to avoid any plasticisation during the different tests; thus the smart steel bar is tested within its elastic range.

We are going to focus now on the first test performed, which was used to determine the mechanical calibration of the measurement units. The loading is divided in 8 steps of 5 kN each, which corresponds to 20 MPa of tensile stress, each load step is applied instantaneously and kept for 120 seconds; the procedure is the same for unloading phase.

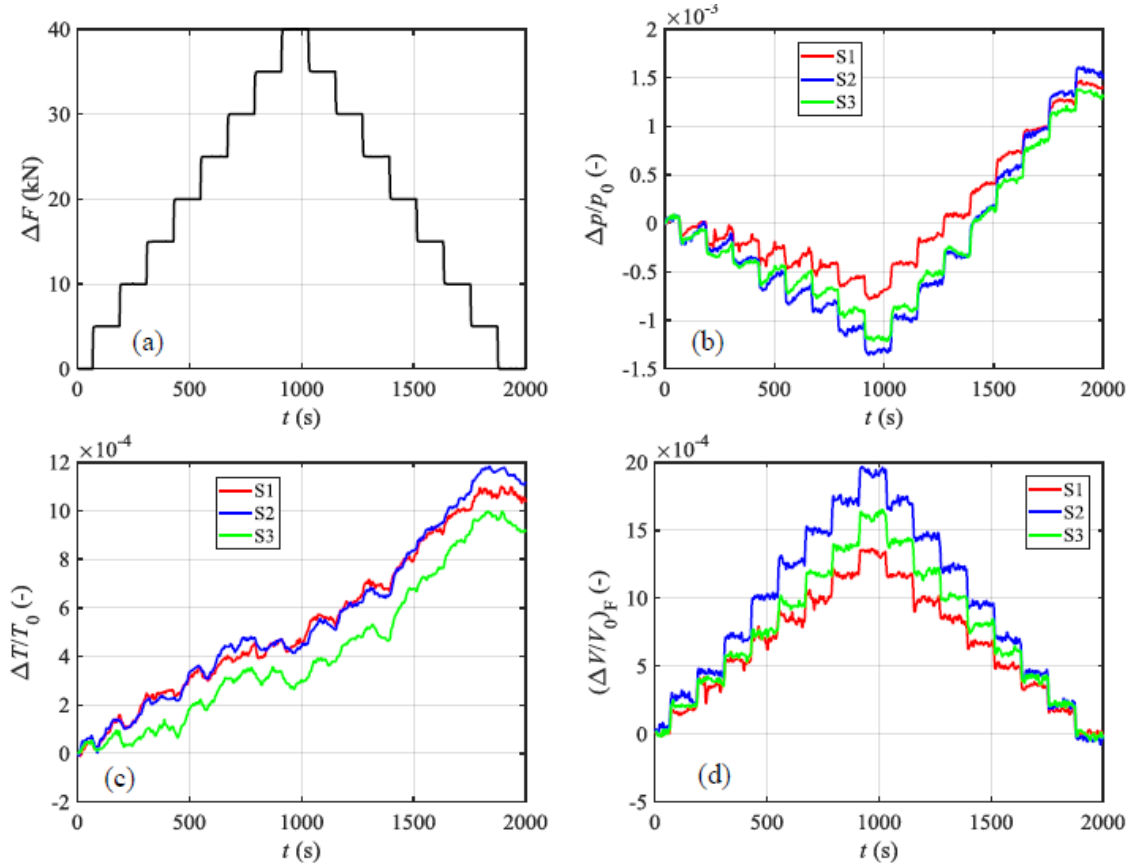


Fig. 59: Axial load test: (a) applied force; (b) measured pressure; (c) measured temperature; (d) reconstructed force-dependent volume variation

Variations of temperature and pressure are measured by S3 system sensors and they are represented here above; $\Delta V/V_0$ is calculated, starting from these values and according to the previous thermal calibration. This ratio represents a sort of mechanical strain due to the state of stress around the cavity and this value varies proportionally to the force applied, because the material is still within its elastic range. The three curves and the respective coefficients k are shown below.

$$\left(\frac{\Delta V}{V_0}\right)_{\Delta F} = \frac{\Delta V}{V_0} - f(\Delta T^*) = g(\Delta F) = \frac{1}{k} \cdot \Delta F$$

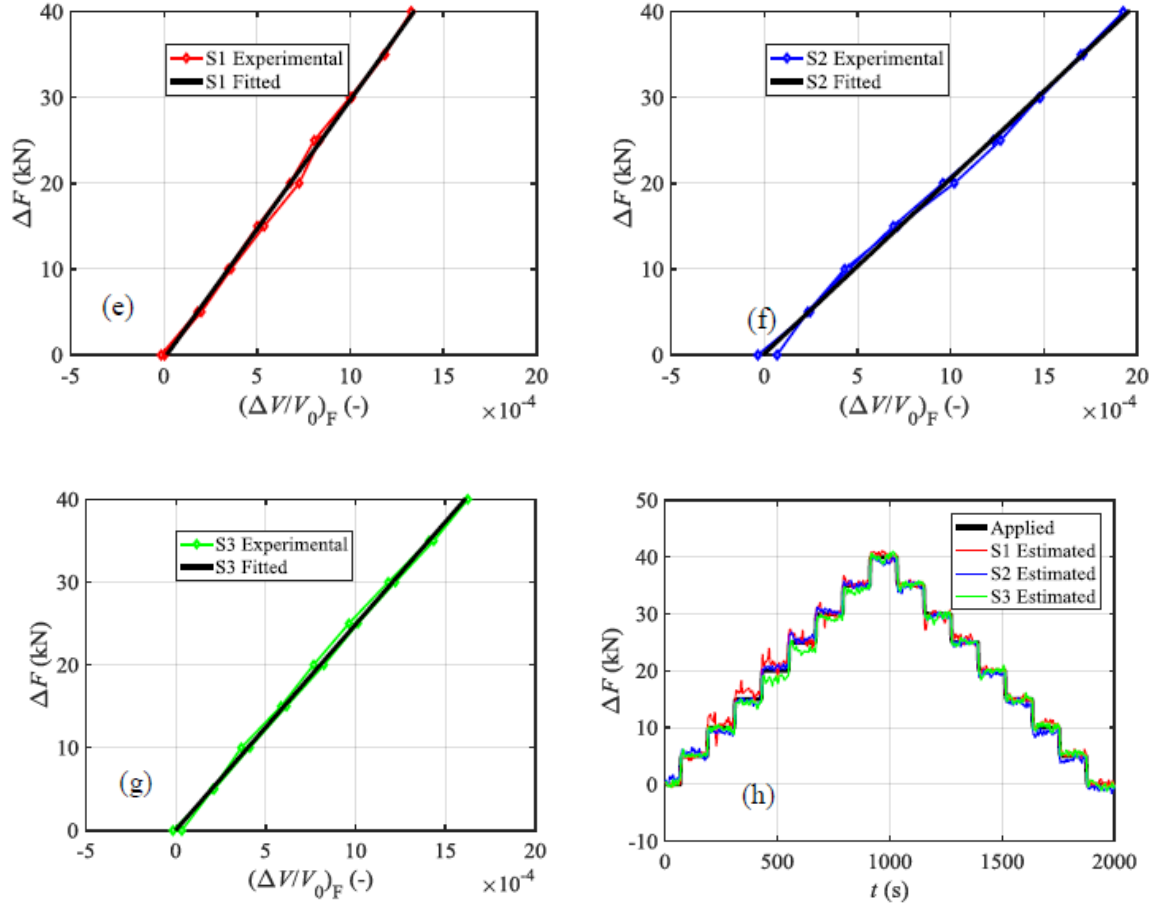


Fig. 60: Axial load test: (e) volume-to-force calibration for sensor S1; (f) volume-to-force calibration for sensor S2; (g) volume-to-force calibration for sensor S3; (h) applied v estimated force

$$k_1 = 3.0162 \cdot 10^4 \text{ kN}, \quad k_2 = 2.0396 \cdot 10^4 \text{ kN}, \quad k_3 = 2.4823 \cdot 10^4 \text{ kN}$$

3.1.4 Axial tensile test until rupture

The instrumented bar is provided with three high precision HBM DD1 strain transducers, which are placed across the three holes: these instruments will measure axial elongation ΔL over 25 mm of bar, in order to check the level of deformation around the cavities. Finally this bar is subject to an axial tensile test until rupture. The first graph shows the relation between force applied and DD1 elongation results over 25 mm of bar; the measurements are interrupted at a certain time, since the instruments are removed before bar reaches failure.

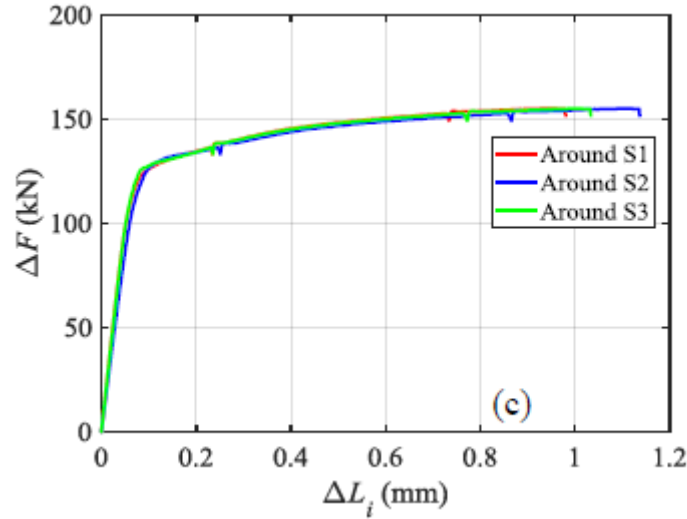
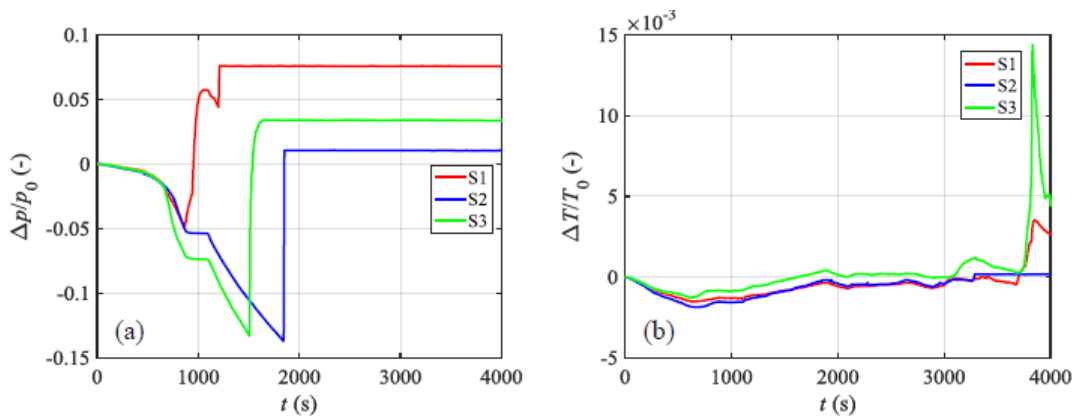


Fig. 61: Monotonic tensile test until rupture: force-displacement relations for the three displacement transducers

The S3 system sensors are able to measure strain until the cavities opening, which occurs firstly for S2 sensor with an applied load of $\Delta F = 135 \text{ kN}$; all the three measurement units are opened in correspondence of $\Delta F = 152 \text{ kN}$ and after this point the force prediction is impossible to realise, because of meaningless pressure and temperature data. Thus S3 system can't survive until rupture at this level of development, but it is able to detect strain along a significant portion of plastic branch. Air volume deformations and applied force predictions are calculated as done before, thanks to pressure and temperature sensing.



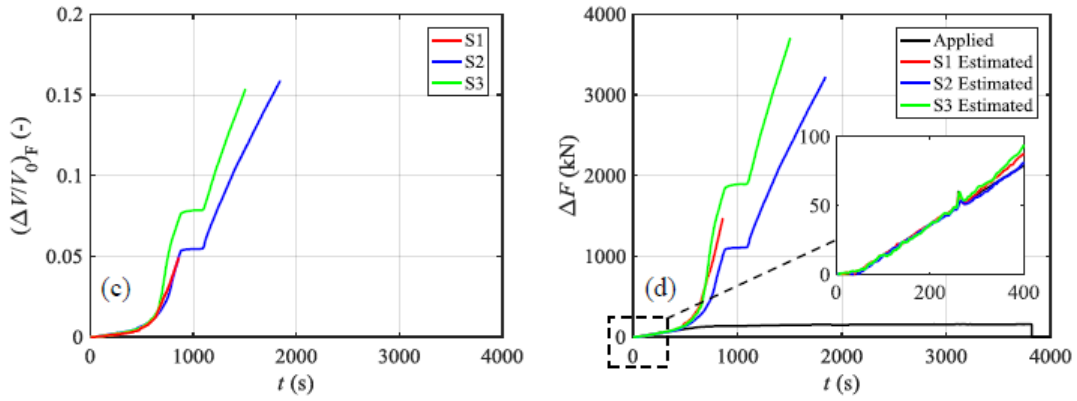


Fig. 62: Monotonic tensile test until rupture: (a) measured pressure; (b) measured temperature; (c) reconstructed force-dependent volume; (d) applied v estimated force

Predicting force passing through the bar is a problem after zone around cavity starts to yield, so when linear behaviour is lost. The previous calibration is valid to determine force values starting from volume deformations of air cavity during elastic branch, but it is not appropriate anymore when plastic strains appear. There is a good matching between actual applied force and predicted force with linear correlation until $\Delta F = 50 \text{ kN}$. The mechanical calibration during plastic behaviour of smart steel bar needs to be developed in further studies. Here below the graph shows the relation between air volume deformation and applied force.

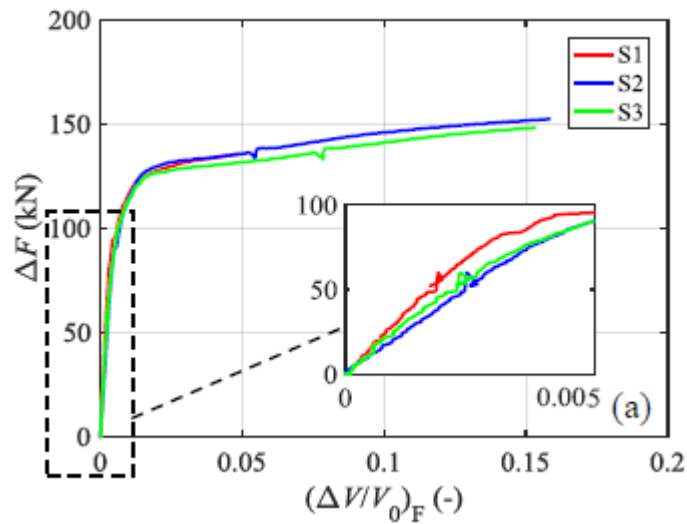


Fig. 63: Monotonic tensile test until rupture: experimental correlations between cavity volume variations and applied force

3.2 Comparison with numerical results

As discussed in Chapter 2, some different F.E.M. models are realised in order to understand the mechanical behaviour of a steel bar equipped with S3 system: here the last numerical results are presented and compared with the values obtained by the previous experimental campaign. Geometry of the models is the last one presented during the previous chapter and it consists on a quarter of a smart steel bar 50 cm long with an hole drilled through: the fluid is contained in a quarter of a transversal cylinder with a diameter of 4 mm and an height of 15.5 mm, while the feed-through zone is represented by a quarter of transversal cylinder with a diameter of 6 mm and an height of 3.5 mm. Two faces have fixed translations because of symmetry reasons and the load is applied under displacement control at the furthest edge from the hole. The model is 25 cm long in order to represent properly the deformed shape actually induced during axial tensile test.

3.2.1 Models description

Four different materials are defined in order to realise a sensitivity analysis: the first case represents the constitutive law as it is given from uniaxial load test on a whole steel bar. As reported in Table 3.2.1, all the other three cases have a yielding stress reduced by about 4%: as we will see, this value gives results closer to the experimental ones and it is still included within a realistic dispersion range of mechanical characteristics. The second model has only this change, while the last two have different bigger maximum strain: the third one has 50%, the fourth one 100%. This values could look like overstated, but we should remember that steel global behaviour is inserted as a local constitutive law and this is a really big simplification. Actually some little portions of material could maybe have much bigger strains than the measured limit, before the bar reaches failure point. This why it is not so absurd to define these kinds of local constitutive law in order to obtain a sensitivity analysis, even if there are wide changes in material characteristics.

Models	Young Modulus E [GPa]	Yielding Stress f_y [MPa]	Maximum Strain A_{gt} [%]
01	200	520	9.6
02	200	500	9.6
03	200	500	50
04	200	500	100

Tab. 3.2.1: Mechanical properties of the four models

3.2.2 Force-Displacement relations comparison

The experimental results are obtained from HBM DD1 transducers placed over a length of 25 mm around the three cavities: the three curves stop when the instruments are taken away before to reach failure in order to preserve them. This means that smart steel bar has further strength resources, but there is no more information after the instruments are removed from the bar. Instead FEM model analysis stops to run, when convergence is not found anymore, so when the bar theoretically reaches failure; there are also other aspects, which could stop the analysis abnormally, like small time step dimension and low mesh quality, but they seem to be adequate.

FEM displacement is directly read in the software output, but this value needs to be multiplied by 2, because it is related to a node placed 12.5 mm far from the cavity centre and so it is originally measuring the displacement due to an half of the actual length considered by DD1 transducers. The displacement under interest is along longitudinal direction (Z-axis) and the force applied as well: this force is obtained multiplying by 2 the longitudinal reaction in a terminal face. The following graphs show the relation between applied force to the bar and the longitudinal displacement referred to 25 mm around the cavity.

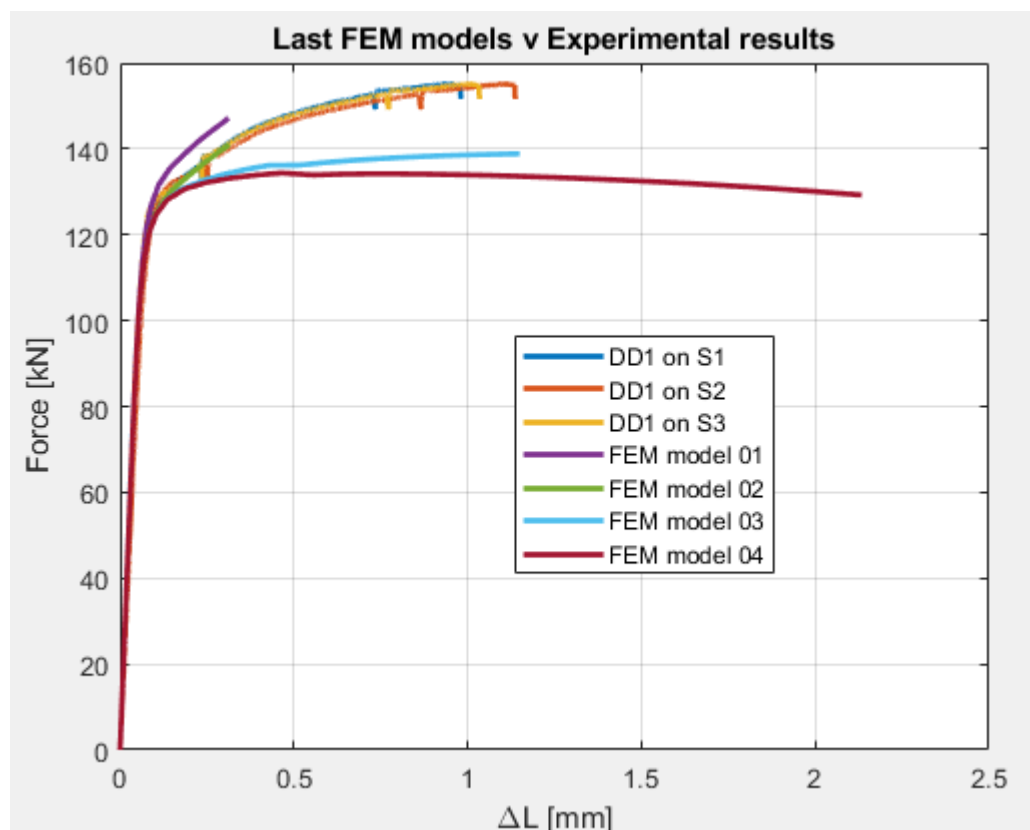


Fig. 64: Force-Displacement comparison

In Figure 64, we can see the comparison between the three DD1 transducer and the four FEM models with a wide view. Having a first look, we can't really compare the curves, because they don't look similar at all; obviously various constitutive laws with different maximum strains determine different maximum volumetric deformations, which could considerably vary. It is important to notice that the original maximum strain value is not effective to describe the bar's behaviour, because the curves of first two model stop before experimental curves ends: this could be due to the fact that a global constitutive law couldn't be suitable to describe the steel's local behaviour in a 3D state of stress. The last two models have maximum deformation values higher than the experimental ones, confirming that it's more correct to allow higher local deformations in the model to describe the actual behaviour of the bar. At the same time, the slope of these plastic branches is very different from the experimental ones and this suggests that increasing maximum strain is not the only correction to be considered in further studies.

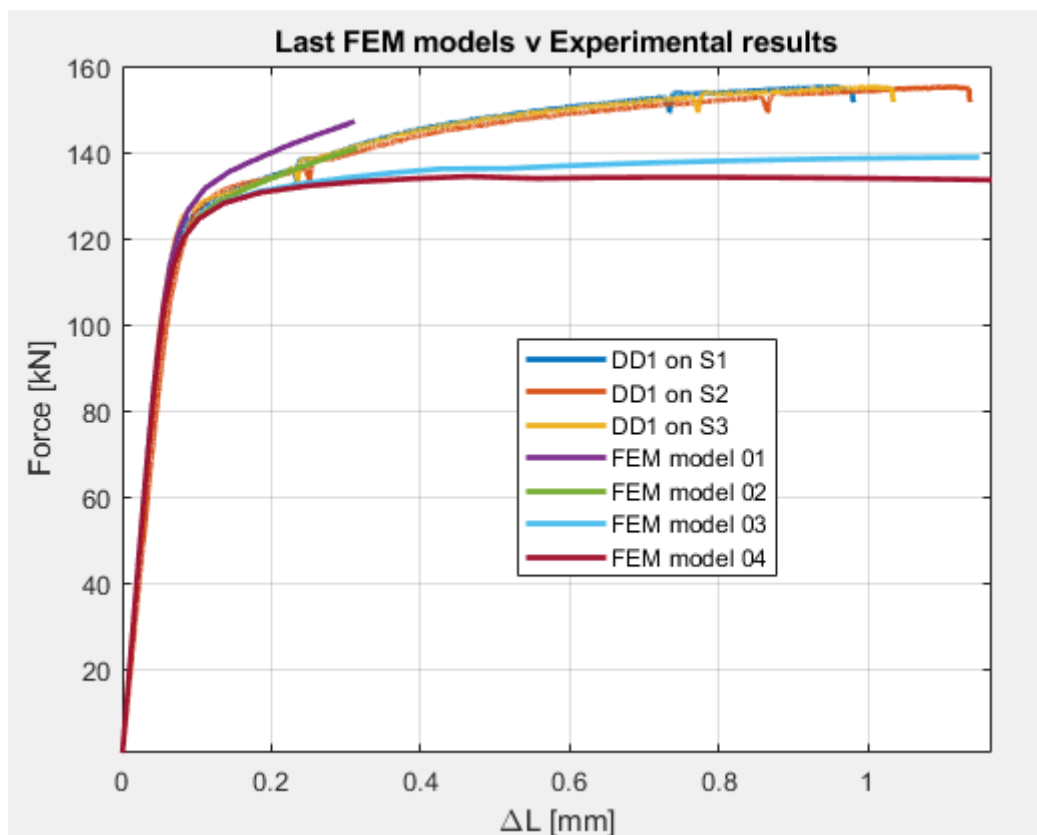


Fig. 65: Force-Displacement comparison - focus on first models

The second graph is realised in order to have a closer overview to experimental curves. As we discussed before, here we can notice how the plastic branch slopes of last two models is very different from actual ones, while the first two show the same slope of the experimental case, even if the convergence is not reached anymore with too small displacement. Here it is more interesting to notice at what level of force applied and displacement there is a sudden slope's change in the curves, that is consequence of steel yielding. Obviously this happens for an higher force in model 01 than in the others, since the first one has the original constitutive law with an higher yielding stress. The models with a yielding stress lowered by about 4% show curves with a change of slopes at the same force value of experimental curves; this is a good result, because mechanical properties have a certain scatter of values, which could be around 5%. Both the first models yield at a level of displacement, which is the same determined during the experimental campaign and this suggests that the elastic branch's slope is well represented; we are going to focus on it in the next graph.

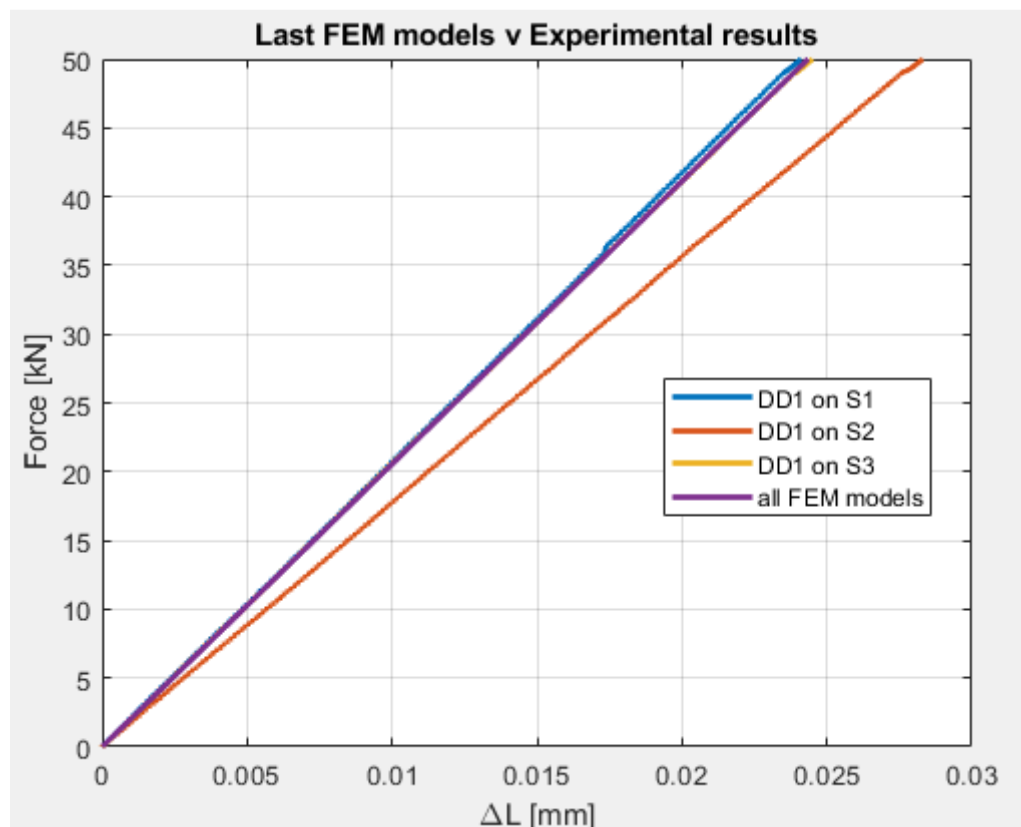


Fig. 66: Force-Displacement comparison - focus on elastic branch

Here we can see the comparison of the linear branch between all the FEM models and experimental results: the numerical curve has the same slope as DD1s placed on S_1 and S_3 , while it is not so similar to the one on S_2 , but this is could be to local defects around that cavity. This fact confirms that the FEM model has a

good behaviour in terms of strain response to the force applied and it is good to interpret the mechanical behaviour of a smart steel bar equipped with S3 system, at least during its elastic branch and yielding point too. Further studies should be realised in order to detect correctly the plasticisation around the cavity.

3.2.3 Force-Deformation relations comparison

The experimental results are obtained from S3 sensors measurements during the last tensile test until rupture: the three curves stop when the cavity sealing reaches failure. This means that smart steel bar has further strength resources, but there is no more information about mechanical behaviour of the bar after cavity is open. Instead FEM model analysis stops to run, when convergence is not found anymore, so when the bar theoretically reaches failure; there are also other aspects, which could stop the analysis abnormally, like small time step dimension and low mesh quality, but they seem to be adequate.

While experimental values $\Delta V/V$ are calculated starting from pressure and temperature changes thanks to General Gas Equation, FEM results are obtained only by considering pressure variations, because temperature is kept constant in the analysis. FEM volumetric deformation is calculated dividing pressure change by bulk modulus previously defined and the force applied is evaluated as the reaction along longitudinal direction (Z-axis) in a terminal face, multiplied by 2. The following graphs show the relation between applied force to the bar and the relative volumetric deformation of the air inside cavity.

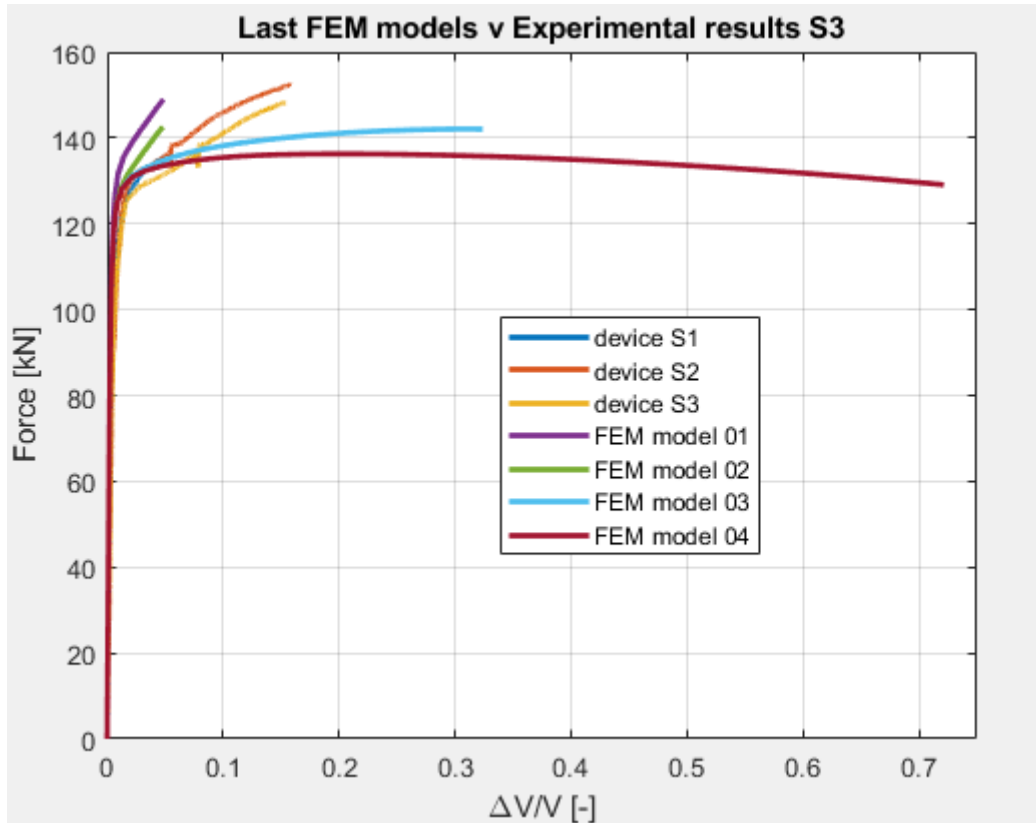


Fig. 67: Force-Deformation comparison

In the first one, we can see the comparison between the three S3 system devices and the four FEM models with a wide view. Also in this case, various constitutive laws with different maximum strains determine different maximum volumetric deformations, which could considerably vary. It is important to notice that the original maximum strain value is not effective to describe the bar's behaviour, because the curves of first two model stop before experimental curves end for the sealing failure: this could be due to the fact that a global constitutive law couldn't be suitable to describe the steel's local behaviour in a 3D state of stress. The last two models have maximum deformation values higher than the experimental ones, confirming that it's more correct to allow higher local deformations in the model to describe the actual behaviour of the bar. At the same time, the slope of these branches is very different from the experimental ones and this suggests that increasing maximum strain is not the only correction to be considered in further studies.

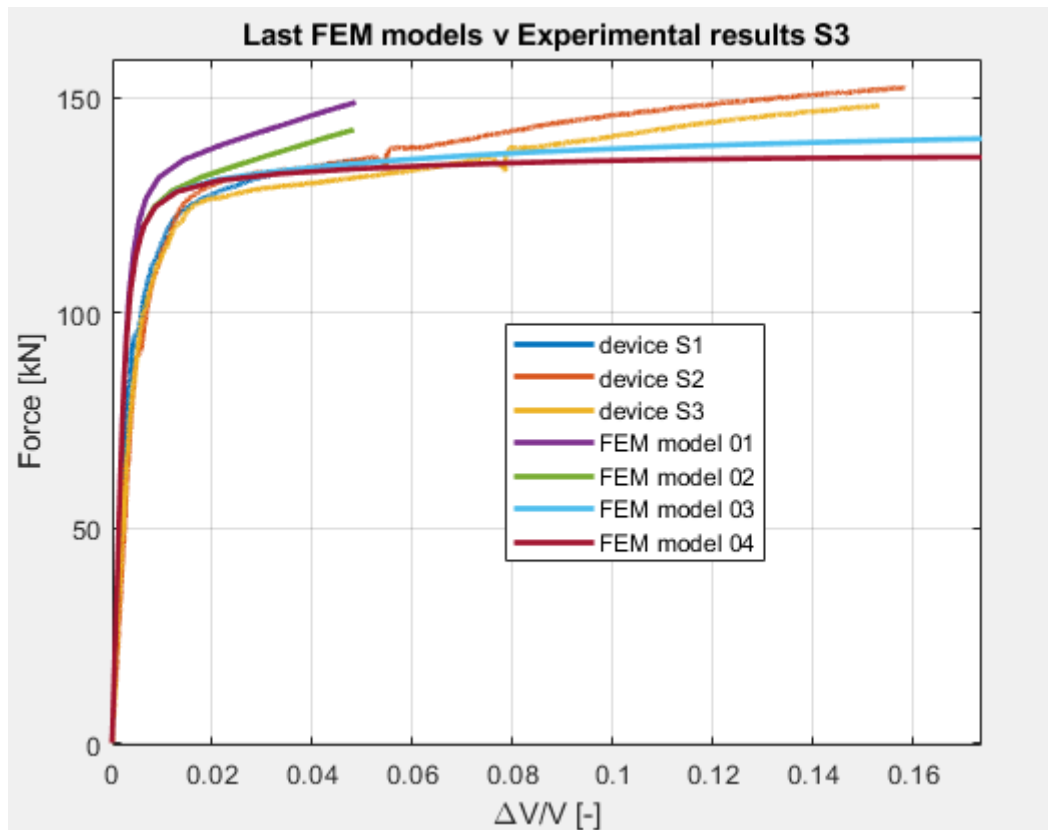


Fig. 68: Force-Deformation comparison - focus on first models

The second graph is realised in order to have a focus next to experimental curves. As we discussed before, here we can notice how the plastic branch slopes of last two models is very different from actual ones, while the first two show almost the same slope of the experimental case, even if the convergence is not reached anymore with too small volumetric deformations. Here it is more interesting to notice at what level of force applied there is a sudden slope's change in the curves, that is consequence of steel yielding. Obviously this happens for an higher force in model 01 than in the others, since the first one has the original constitutive law with an higher yielding stress. The models with a yielding stress lowered by about 4% show curves with a change of slopes approximately at the same force value of experimental curves; this is a good result, because mechanical properties have a certain dispersion of values, which could be around 5%. At the same time, we have to notice that this yielding sensed by air cavity happens for lower values of deformation than in reality and this is a problem that we are going to discuss, having a look to next graph.

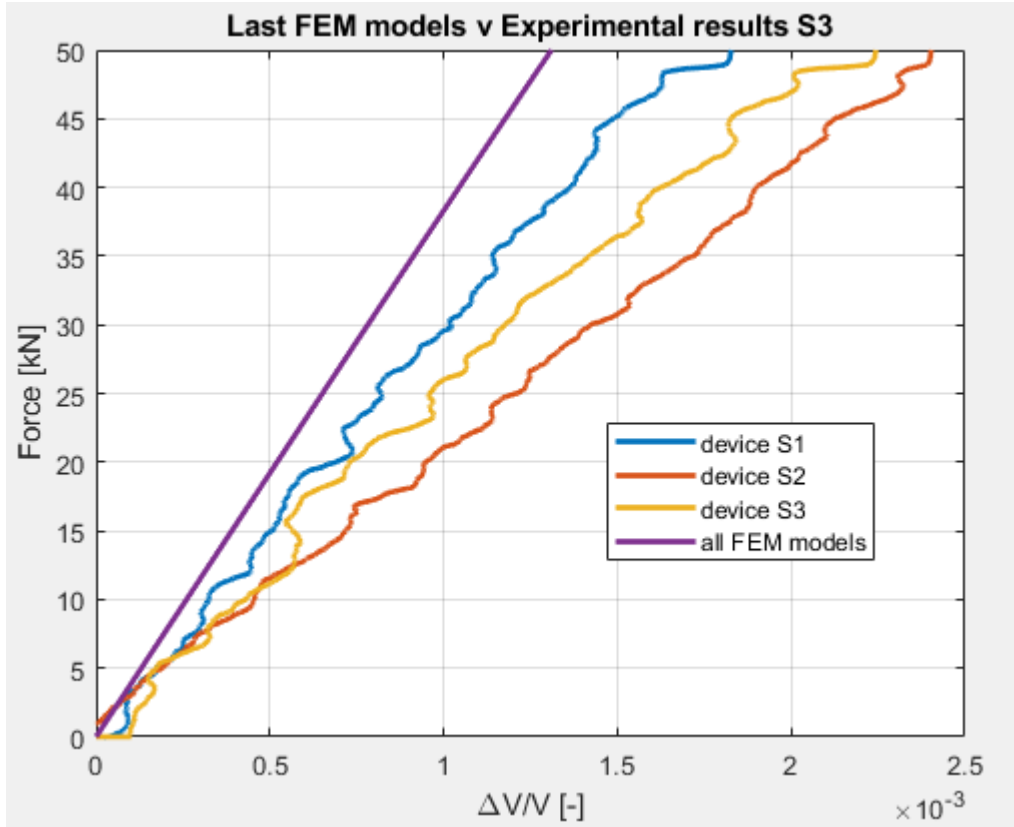


Fig. 69: Force-Deformation comparison - focus on elastic branch

The main difference between FEM models and experimental results is highlighted in Figure 69: all the FEM models have the same elastic branch's slope, which is higher than all the three experimental outcomes. This means that the models seem to be quite more rigid than in reality; at the same time, we should notice that also the mechanical characterisation of the three devices is not the same, as if every unit sensing force passing through the bar with a different stiffness, probably because of different thermo-mechanical situations inside the cavities. A necessary correction to apply to FEM results is related to the presence of non-deformable material inside the cavity, which increases the volumetric deformations in correspondence with same pressure readings, as we discussed in Chapter 2. Inside the cavity there are some additional elements like the transducer and hard PCB and the total volume occupied by these components is estimated to be around 32 mm^3 , which means that we should consider a non-deformable volume of 8 mm^3 in the quarter of cavity model.

$$V_{nd} = 8 \text{ mm}^3$$

$$k = \frac{V_d}{V_d - V_{nd}} = \frac{51.14 \text{ mm}^3}{51.14 \text{ mm}^3 - 8 \text{ mm}^3} = 1.185$$

$$\left(\frac{\Delta V}{V}\right)_b = \left(\frac{\Delta V}{V}\right)_a \cdot k$$

This correction determines an increase by about 18% of the air volumetric deformations and this gives a reduction of the elastic branch's slope. In this way the results are closer to experimental ones, even if sensing stiffness of models is still a little higher and so further studies to improve FEM modelling are required.

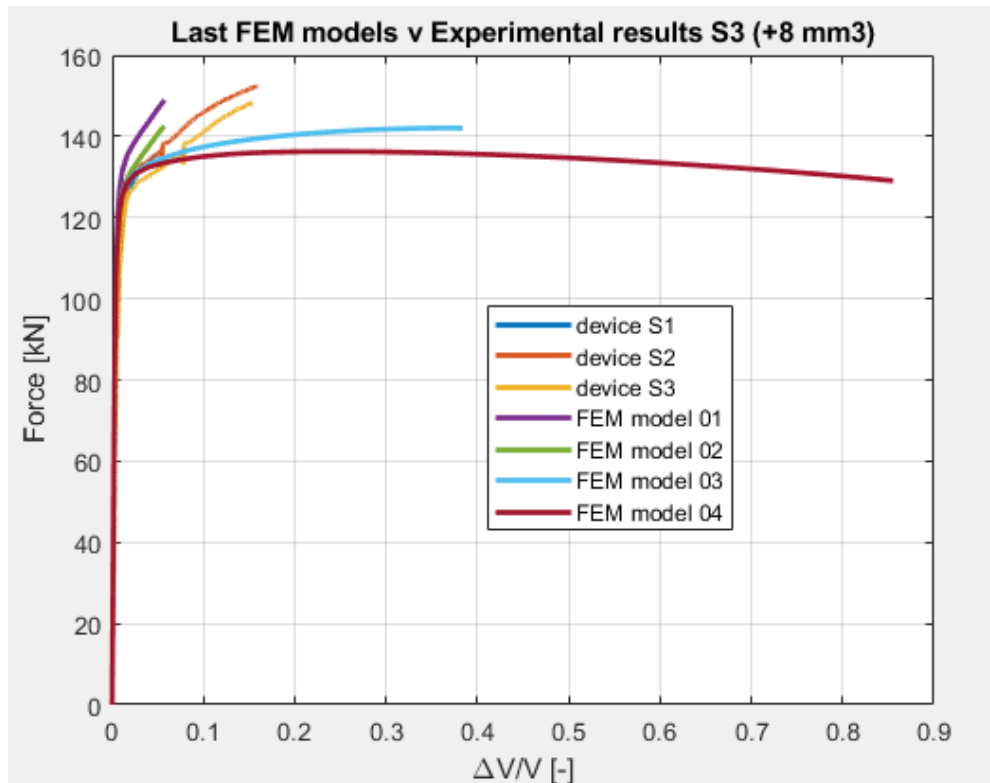


Fig. 70: Force-Deformation comparison - 8 mm³ n.d.

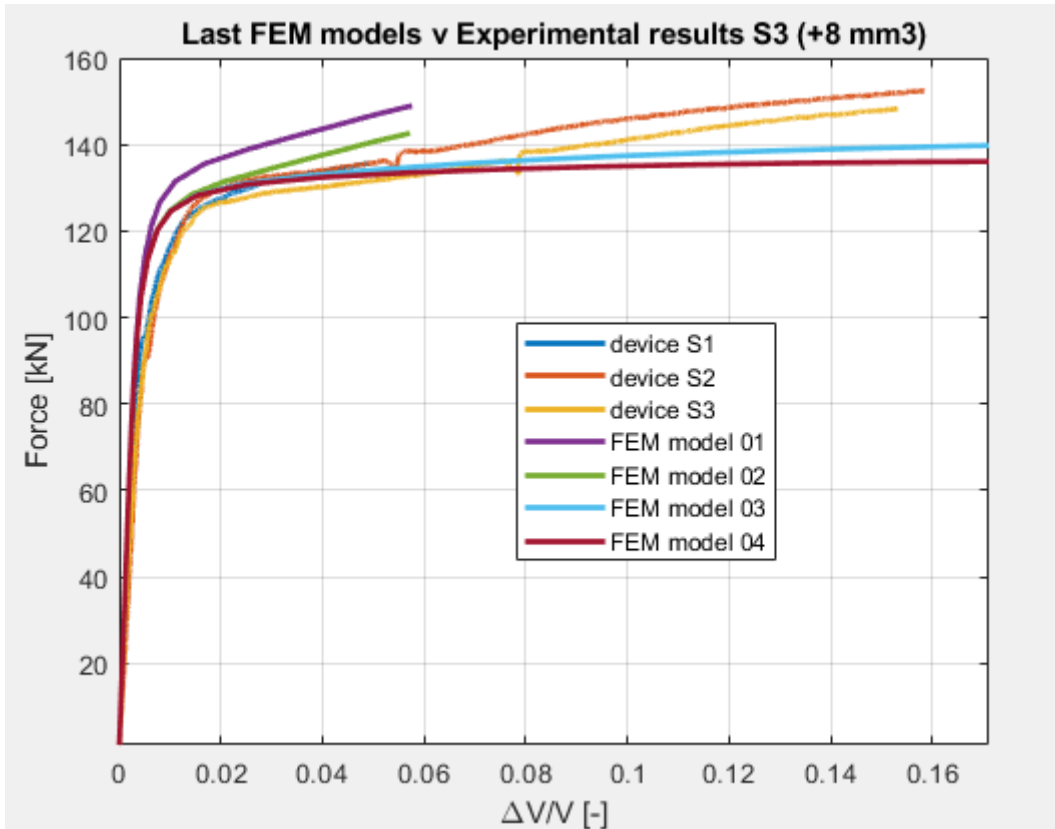


Fig. 71: Force-Deformation comparison - 8 mm³ n.d. - focus on first models

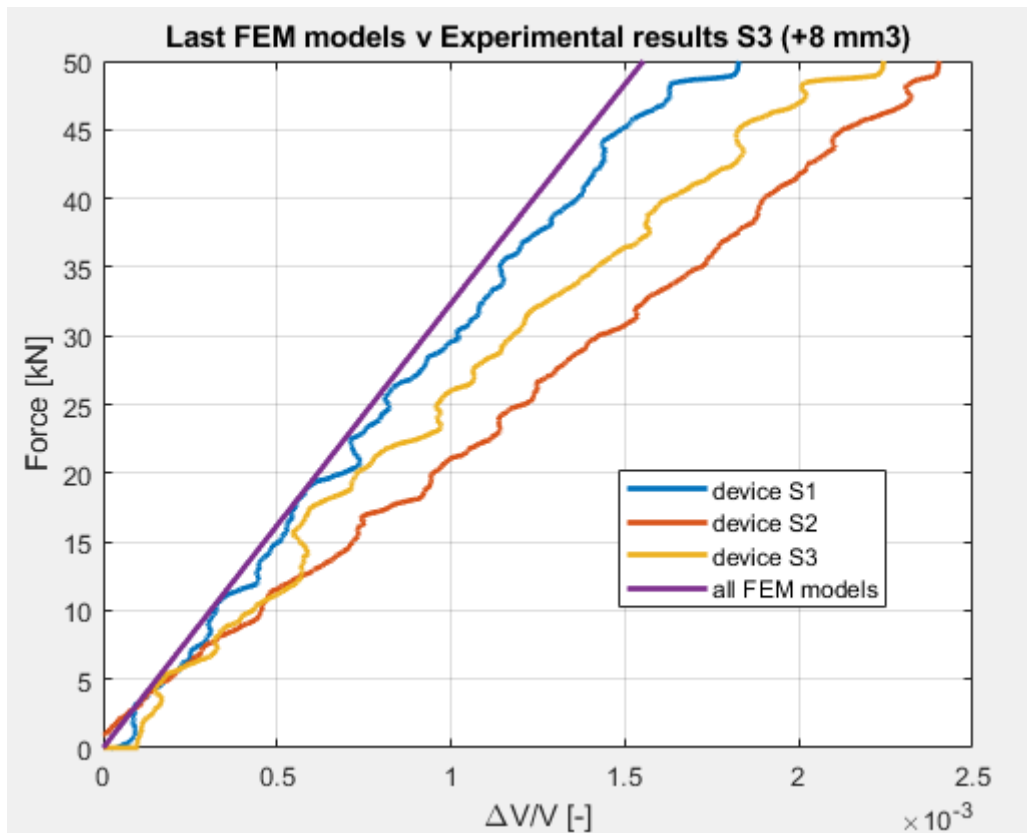


Fig. 72: Force-Deformation comparison - 8 mm³ n.d. - focus on elastic branch

Chapter 4

4. Experimental study

In this chapter we are going to analyze "S3 system" in smart steel bars by means of a complete experimental study. Firstly the bars instrumented with the smart monitoring system are characterised with tensile tests, then these bars are located as reinforcement in casted beams. Finally, a 4-point bending test is realised, monitoring the mechanical behaviour of the elements with traditional strain gauges too.

4.1 Instrumented bars tensile test

It's important to characterize the mechanical behaviours of the instrumented steel bars under tension and so I have to prepare them for tensile tests. This is also a good test for the S3 system measurements in order to verify the theoretical relationships in a situation of applied load. The bars are tested with the tensile testing machine (MTS 250 kN), which applies load steps of 5 kN every 60 seconds until the maximum value of 40 kN, because I want to keep the steel in the elastic behaviour to don't damage bars.

4.1.1 Axial tensile test staging

Each instrumented $\Phi 20$ B450C bar has both threaded extremities, it is long 1 meter and has two sensors embedded in the steel (except for B1, which has only one), one 195 mm far from the edge, the other one 205 mm far from the opposite edge. I cut two pieces of $\Phi 20$ steel bar with one threaded extremity for a length of about 20 cm, in order to don't have direct contact between the jaws and the instrumented bar. Thanks to Bartec couplers (length of 55 mm, diameter of 30 mm), I connect the two pieces to the instrumented bar's edges and I close the MTS jaws around them. I repeat the same procedure for all the bars.

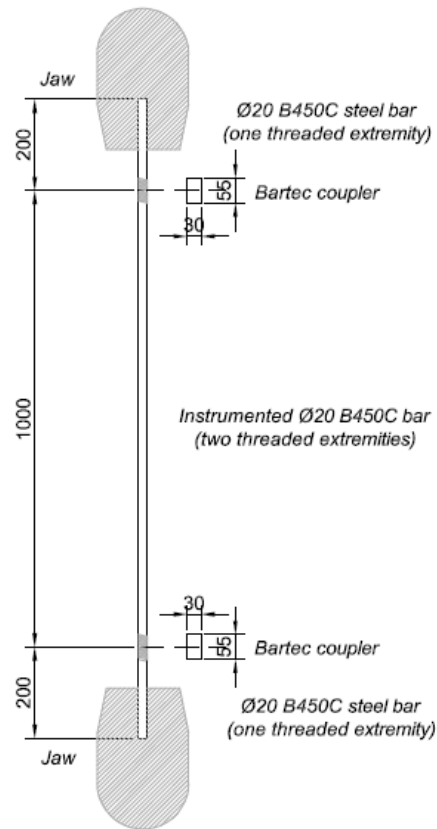


Fig. 73: Axial tensile test scheme

I take a 1 meter long piece of timber and I place it vertically next to the steel bar, along one column of the testing machine. So I put in position two converter boards at about the same height of the sensors, in order to acquire the measurements by means of the soft PCBs linked to the boards. The CB are connected by cables to the data acquisition and energy supply system.

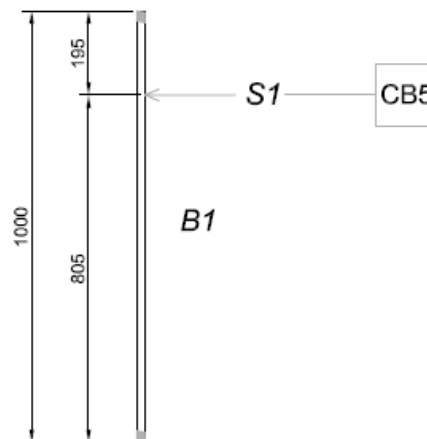


Fig. 74: Axial tensile test configuration (a) and a zoomed view (b)

4.1.2 Sensors numeration and CB settings

The five instrumented steel bars -B1, B2, B3, B4 and B5- have in total nine sensors -S1, S2, S3, S4, S5, S6, S7, S8 and S9- and they are tested one at a time by the MTS. The upper sensors are connected to the converter board CB5 and the lower ones to the converter board CB3. They both are set in the same way:

- >Temperature Middle: 22°C
- >Temperature Threshold: 5°C
- >Pressure Middle: 98 kPa
- >Pressure Threshold: 1 kPa
- >Moving Average: 1 sample



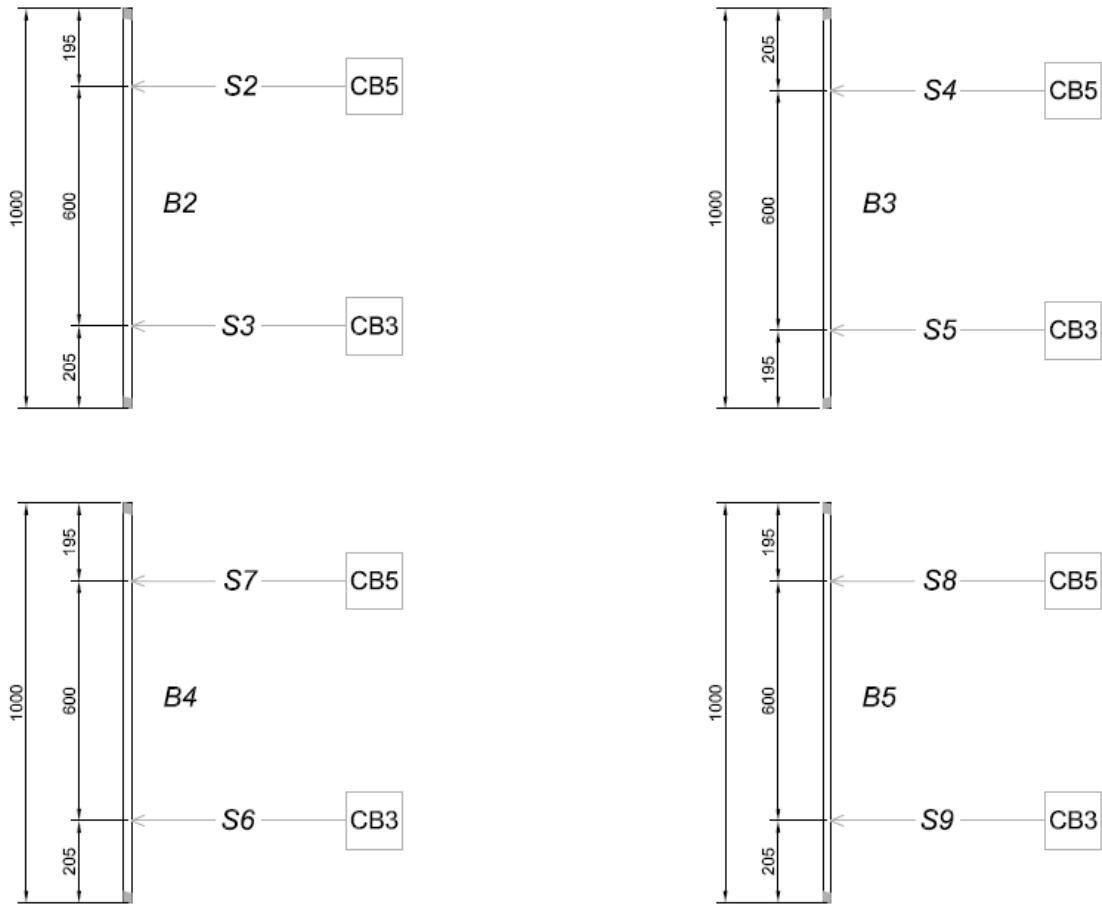


Fig. 75: S3 system numeration: bars from B1 to B5 from figures (a) to (e)

4.1.3 Load path applied

The tensile load is applied with eight incremental steps of 5 kN every 60 seconds, till it reaches the value of 40 kN and it remains so for 120 seconds. Then, the MTS starts to decrease the load with other eight steps of 5 kN every 60 seconds, until there is no more applied tension anymore.

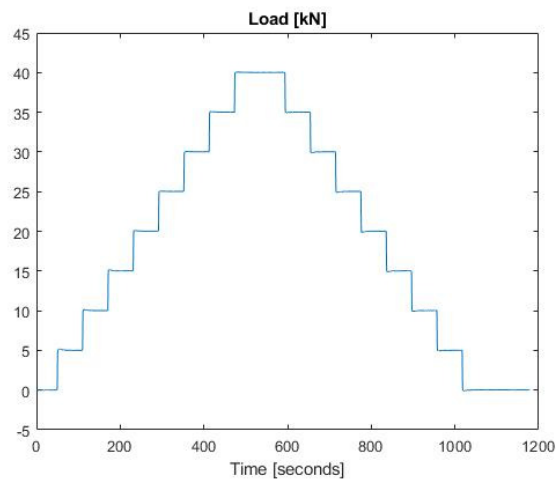
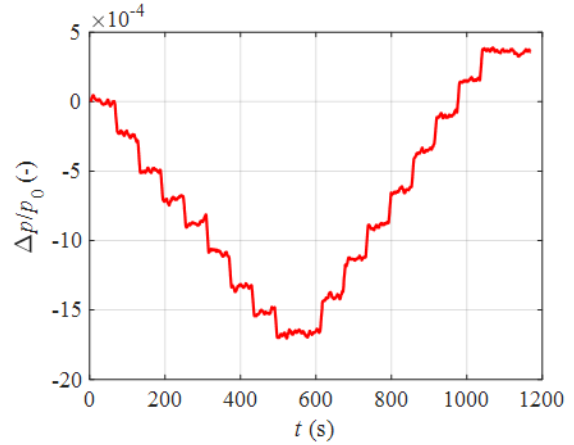
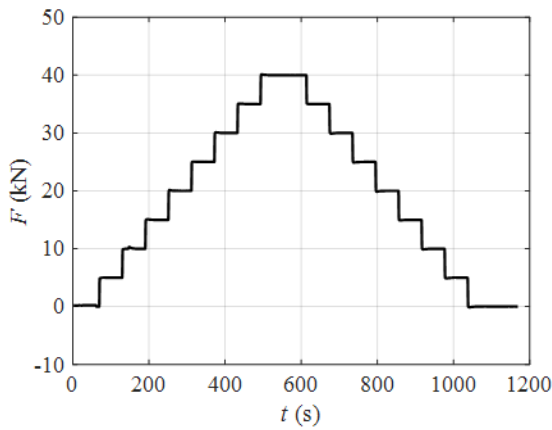


Fig. 76: Time history of applied load

4.1.4 Mechanical characterisation results

The results of the mechanical calibration test are summarized for the *S2* unit in the following figures, where time histories are reported for, respectively, the applied force (a), the measured pressure (b) and temperature (c) variations, the volumetric deformations (d) (corrected to account for the temperature variations occurring during the test), the deformation-to-force calibration function (e), and the comparison between the applied and estimated axial force (f). In particular, the angular coefficient of the straight line in figure (e) represents the mechanical calibration coefficient k_1 for this unit. The corresponding mechanical calibration coefficient k_2 is nothing but k_1 divided by the axial stiffness EA referred to the bar gross transversal area (where $E = 200$ GPa is assumed). By looking at the figures, a satisfactory matching between the applied and the estimated load is apparent (figure f), reflecting the substantial proportionality and the negligible hysteresis inherent in the deformation-to-force relations (figure e).



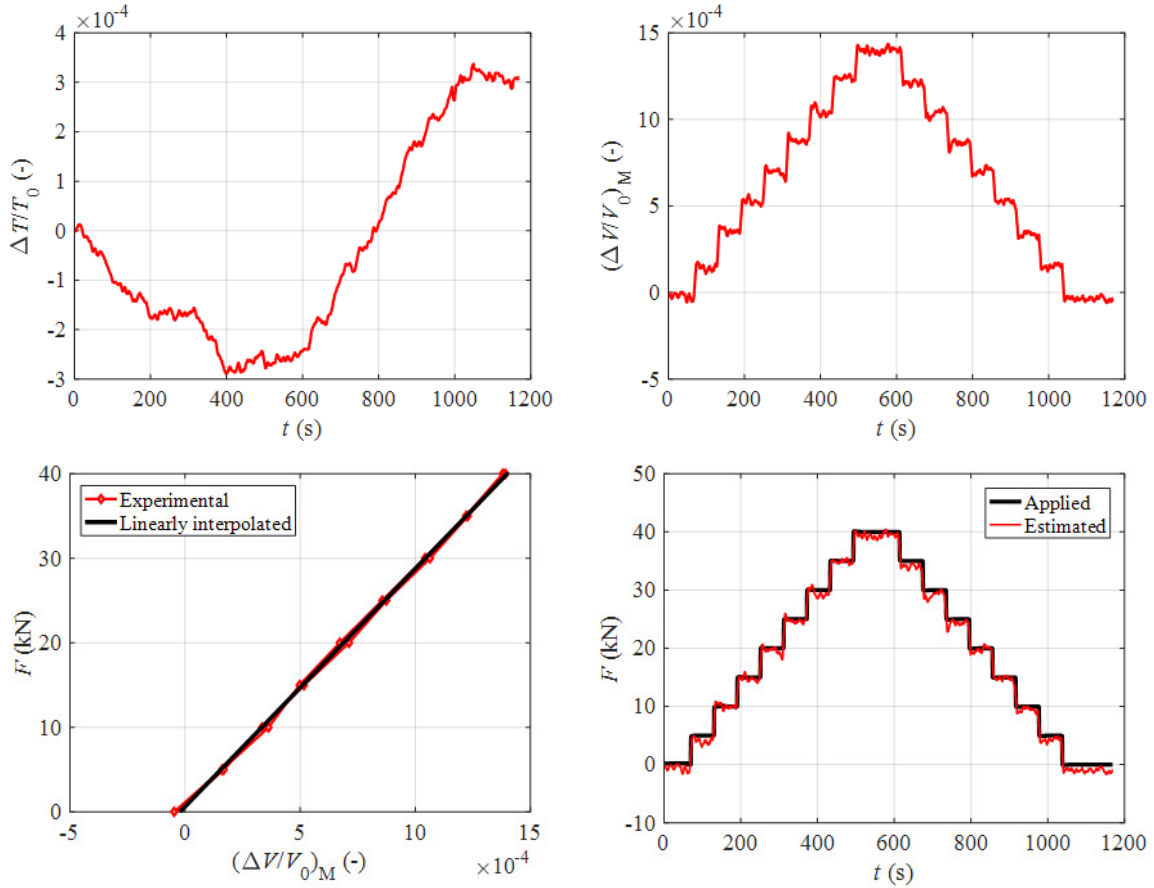


Fig. 77: Mechanical calibration test for the S2 unit: (a) applied force; (b) measured pressure; (c) measured temperature; (d) reconstructed force-dependent volume variation; (e) volume-to-force calibration; (f) applied v estimated force (Tondolo, 2018)

By repeating the procedure for the other three sensing units, the calibration coefficients k_1 and k_2 are eventually obtained and they are reported for completeness in the table below. It can be observed that these coefficients appear quite homogeneous among the four units.

Bar	Unit	k_1 [kN]	k_2 [$\mu\text{m}/\text{m}$]
B2	S2	$2.815 \cdot 10^4$	$4.481 \cdot 10^5$
B2	S3	$2.646 \cdot 10^4$	$4.212 \cdot 10^5$
B3	S4	$2.816 \cdot 10^4$	$4.481 \cdot 10^5$
B3	S5	$2.987 \cdot 10^4$	$4.755 \cdot 10^5$

4.2 The 4-point bending test

It's now necessary to validate the measurement system in a typical situation for civil engineering applications, a beam subjected to bending moment. In order to find out if the system is able to monitor strain properly, I prepare the 4-point bending test on two reinforced concrete beams equipped with S3 system and strain gages. The aim of the experiment is to control the strain development in

the reinforcing steel until flexural collapse, comparing innovative and conventional measurements: thanks to the testing method, I can arrange the instruments in two zones, where the bending moment is linearly varying and where the bending moment is constant - between the two points of load application the shear force is zero.

The two beams (Beam1, Beam2) are realised according to the following drawings.

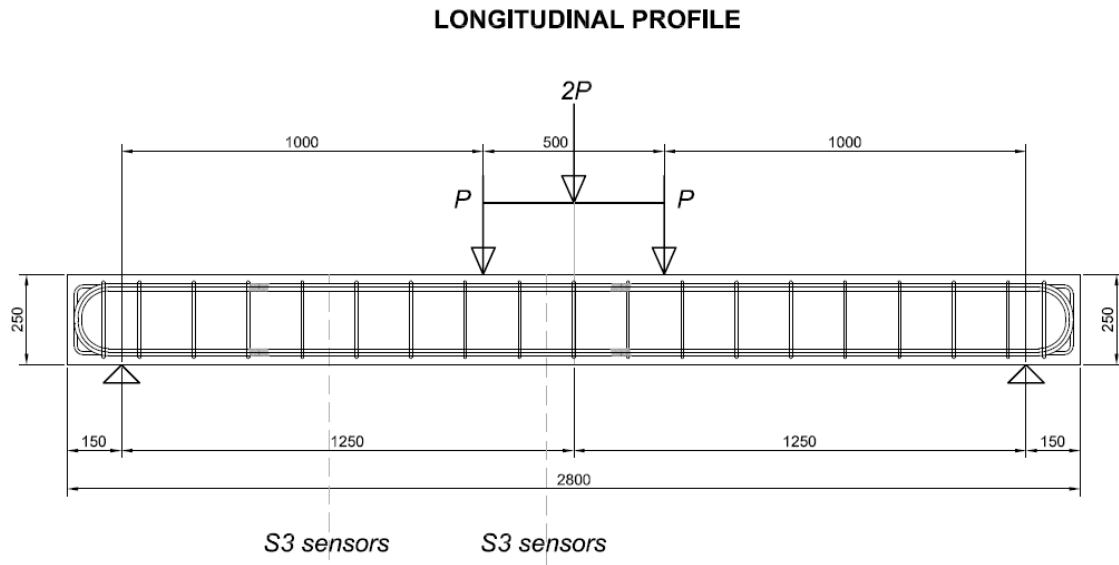


Fig. 78: Longitudinal profile of the RC beam

TRANSVERSAL SECTION

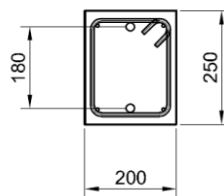


Fig. 79: Transversal section of the RC beam

4.2.1 Strain gages installation

The four instrumented steel bars previously tested (B2 - B3 - B4 - B5) are now equipped with three strain gages apiece, twelve in total: the instruments are steel foil linear strain gages from Y series (HBM product n° 1-LY41-6/120). Each bar should have the same scheme: one strain gage is located at the same level of the

first sensor, the other one at the level of the second sensor and the last one at the distance of 12 cm from the second sensor. In this way, there will be two strain gages in the constant bending moment zone, in order to compare the axial strain measurement of the bar in the holed section and in the full section with the same bending moment applied. All the three strain gages must be placed in the bar's opposite side of the sensors' feed-through positions. Here the scheme for bar B2 is presented (G stands for strain gages, S for S3 sensors, dimensions in mm).

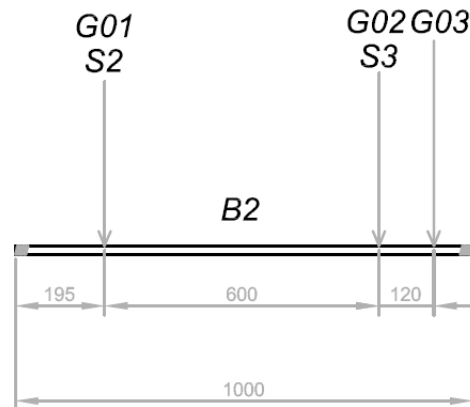


Fig. 80: S3 sensors and strain gauges placement in bar B2

Smooth surfaces are realised with an angle grinder in generous areas around the three measuring points, they are sanded off with a fine grit sandpaper, in order to be roughened for a better adhesion, and then they are finely cleaned with a rag soaked in light petroleum. A mark is traced to have an aligned positioning of the instrument along the longitudinal direction of the bar and finally the strain gages are glued to the surfaces of the bar with a cyanotic glue (Z70, HBM). After waiting an appropriate time for the chemical bonding forces development, the instruments are soldered to the cables and covered by a protective coating made of silicone rubber (SG250, HBM).



Fig. 81: Sanding off bar's surface



Fig. 82: Strain gauges glued to bar's surface



Fig. 83: Strain gauges final configuration

4.2.2 Reinforcement cage realisation

The reinforcement steel cage is realised by assembling $\Phi 8$ B450C bars with stirrups. For each beam, the cage is composed by four longitudinal $\Phi 8$ steel bars 2967 mm long, bent at the two extremities for a distance of 116 mm with a curvature radius of 16 mm and nineteen $\Phi 8$ stirrups arranged with a longitudinal spacing of 15 cm along the span and 10 cm on the supports. The stirrup has 2 arms, an height of 216 mm and a width of 176 mm, with a total length of 845 mm. The four longitudinal bars, two in upper position and two in lower one, are located at the angles of the stirrups and they are tied with steel wire.

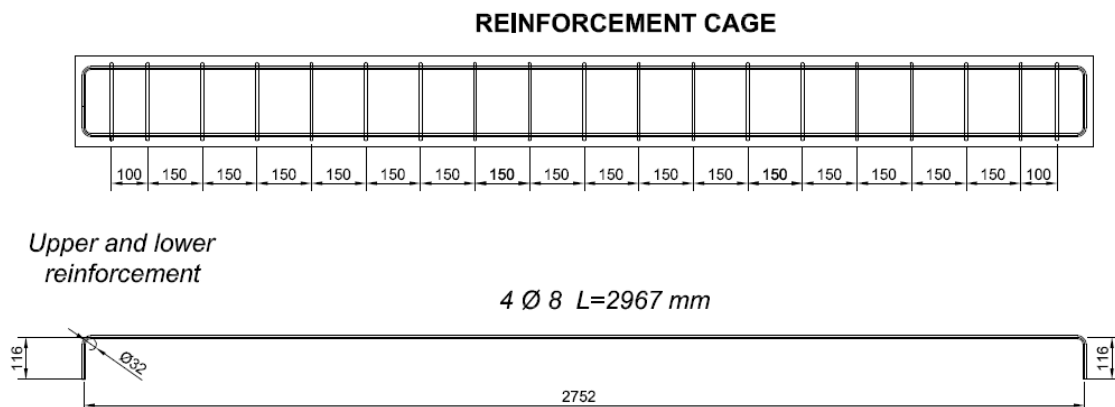
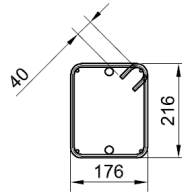


Fig. 84: Reinforcement cage's longitudinal profile

*Transversal
reinforcement*



19 \varnothing 8 L=845 mm

Fig. 85: Steel reinforcement's transversal section



Fig. 86: Reinforcement cage

4.2.3 Instrumented reinforcement bars assembly

The main reinforcement is represented by $\Phi 20$ B450C steel bars and each one is composed by three pieces: in the middle I place the instrumented bar, tested before and equipped with the measurement instruments (S3 system sensors and strain gages). The central bar is 1 meter long and it has two threaded extremities: the other two parts of bars are connected to its edges by means of two Bartec couplers (diameter of 30 mm, length of 55 mm). The first steel piece is 611 mm long and it is bent at the end for a distance of 157 mm with a curvature radius of 75 mm and the other piece is 1351 mm long, bent at the end for a distance of 157 mm with a curvature radius of 75 mm. All the three pieces are tightened, by fastening the threaded parts with the couplers in order to have only one steel bar: for each beam I need two Full Bars, one as upper reinforcement and the other as lower one, so in total I prepare four of them (FB1 and FB2 for Beam1 - FB3 and FB4 for Beam2).

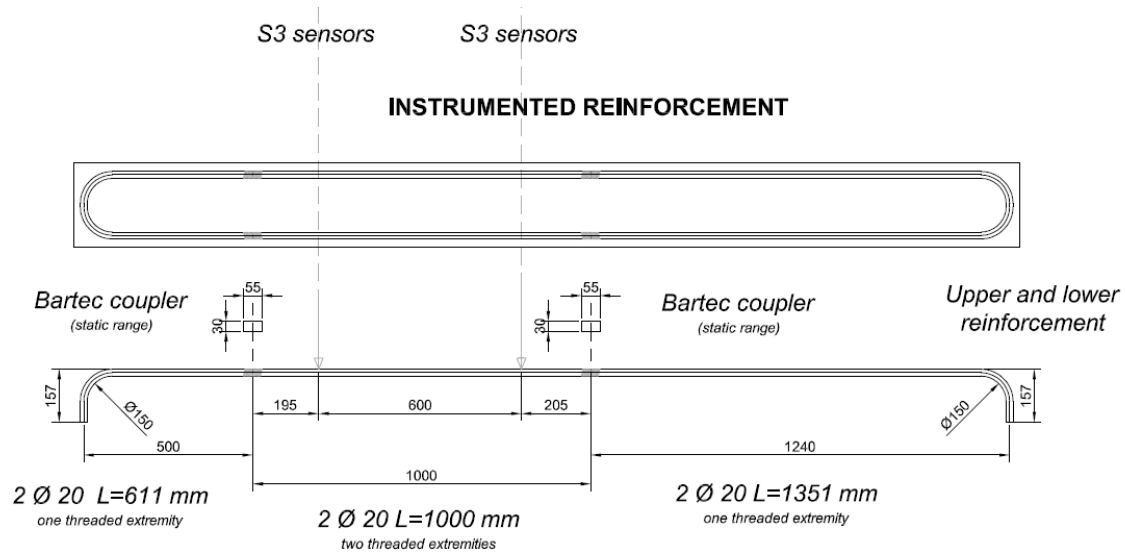


Fig. 87: Instrumented reinforcement longitudinal profile

I take the bars with one threaded extremity and according to the dimensions given, I bend them with a steel bending machine using a spindle with a diameter of 150 mm, then the ending part is cut with a circular saw blade. Finally, the three pieces are assembled in the full bar, which is accurately placed inside the reinforcement cage and it is tied with steel wire; the procedure is the same for upper and lower full bars.

Then, two formworks are realised by assembling iron plates in order to contain two parallelepipeds, having an height of 25 cm, a width of 20 cm and a length of 280 cm. The internal surfaces of the formworks are painted with oil; here both the cages are placed and kept in position by upper supports made by steel wires attached to pieces of timber.



Fig. 88: Steel bars bending



Fig. 89: Reinforcement cage assembled with instrumented reinforcement



Fig. 90: Cables organisation and numeration



Fig. 91: Formworks assembly



Fig. 92: Reinforcement placed inside the formworks for Beam1 and Beam2

4.3.4 Strain gages and sensors numeration

The reinforcement cage and the instrumented bars are almost completed; the last part to do is to organize all the measuring instruments with progressive alphanumerical names and write them in wrappers at the terminal parts of the cables. This is important to know the position of the instruments, when I won't be able to see them anymore, because embedded in concrete.

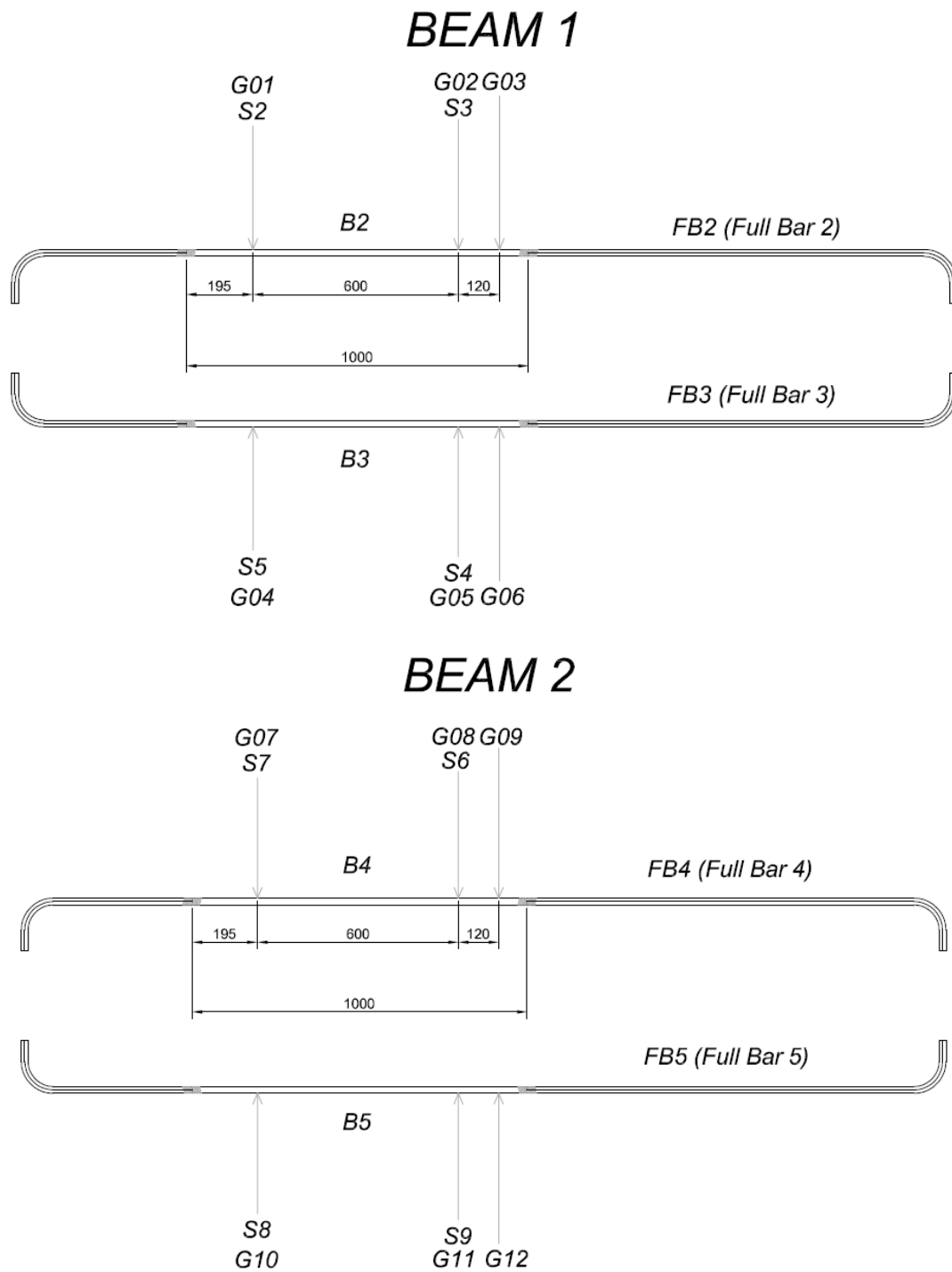


Fig. 93: Beam1 (a) and Beam2 (b) measurement units numeration

4.3.5 Concrete mix design

In the laboratory there are three types of aggregates: thin sand (0-2), coarse sand (0-5) and gravel (3-8). I use an Excel algorithm to obtain the best aggregates mix, so that the overall granulometry curve can be close to the theoretical Fuller curve as much as possible.

Aggregate	3-8	0-2	0-5
Percentage	22 %	25 %	53 %

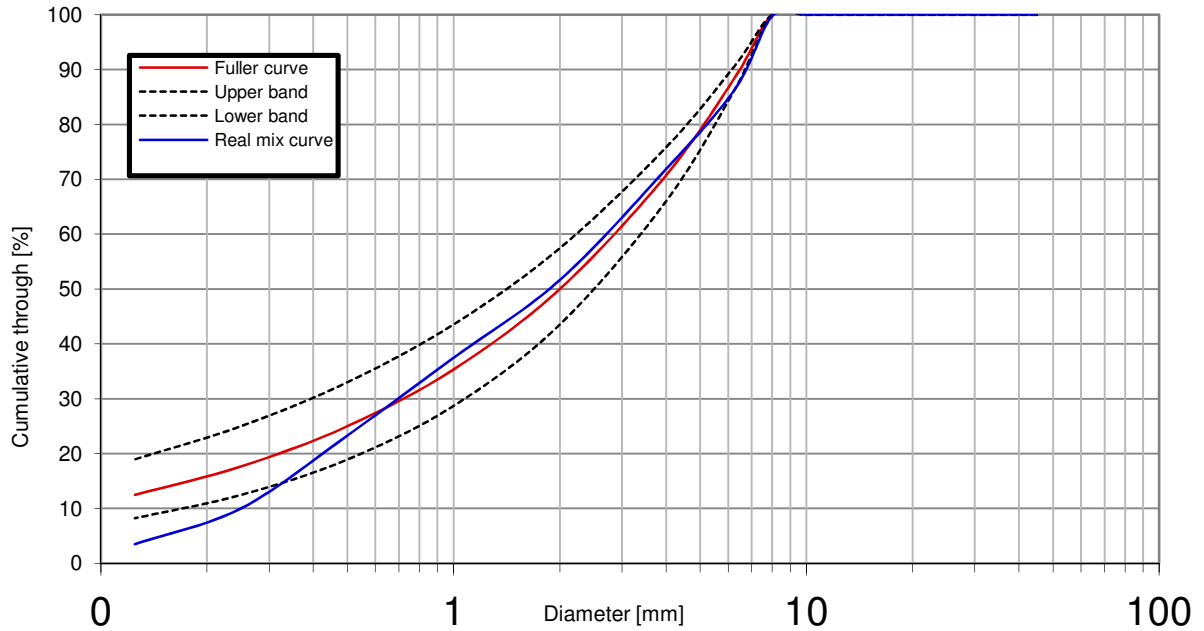


Fig. 94: Granulometric curve for mix design

The concrete mixer capacity is limited, so I have to prepare two concrete mixes: the first one for Beam 1 and the related cylinders (diameter of 15 cm, height of 30 cm), needed for the mechanical characterisation tests, and the second one for Beam 2 and the other cylinders. For each different concrete, I need to realise at least three cylinders for compression tests and three for tensile tests.

Element	V [m ³]	Quantity	V [l]
Beam	0.140	1	140.0
Cylindrical specimens	0.005	6	31.8
Concrete in total	/	/	171.8

The beam has a volume of 140 litres and the specimens around 32 litres, so both concrete mixes need to have at least a volume of 172 litres; I decide to prepare 40 litres more each, so 210 litres in total (the second one has 1,5 litre of water more to increase the W/C ratio for a better workability).

The mix designs are decided according to these assumptions: 340 kg of cement for 1 cubic meter of concrete, ratio water/cement equal to 0,50 (0,52 in the second mix), air estimated in a percentage by volume of 3,1%, plasticiser added in a percentage by mass of 1% and aggregates mix as established before.

First Mix Design (210 litres) for Beam 1				
Component	V[l]	V[m ³]	M [kg]	MV [gr/cm ³]
Cement	23,4	0,023	71,4	3,05
3-8 (gravel)	32,2	0,032	83,7	2,60
0-2 (thin sand)	36,1	0,036	93,8	2,60
0-5 (coarse sand)	75,5	0,075	196,2	2,60
Water (W/C = 0,50)	35,7	0,036	35,7	1,00
Air (3,1% by V)	6,5	0,007	0,0	0,00
Plasticiser (1% by M)	0,7	0,001	0,7	1,10
<u>Concrete in total</u>	210	0,210	481,5	2,29

Second Mix Design (211,5 litres) for Beam 2				
Component	V[l]	V[m ³]	M [kg]	MV [gr/cm ³]
Cement	23,4	0,023	71,4	3,05
3-8 (gravel)	32,2	0,032	83,7	2,60
0-2 (thin sand)	36,1	0,036	93,8	2,60
0-5 (coarse sand)	75,5	0,075	196,2	2,60
Water (W/C = 0,52)	37,2	0,037	37,2	1,00
Air (3,1% by V)	6,5	0,007	0,0	0,00
Plasticiser (1% by M)	0,7	0,001	0,7	1,10
<u>Concrete in total</u>	211,5	0,212	483,0	2,30

When mix is prepared, concrete is poured inside the formworks and it is kept moist during the curing period in order to achieve optimal mechanical characteristics. The formworks are removed just some days after, when concrete setting is concluded; we consider hardening phase finished conventionally after 28 days with around 90% of mechanical strength reached. Beam 1 and its related cylinders are tested after about two months after concrete casting.



Fig. 95: Concrete poured in the formworks for Beam1 and Beam2



Fig. 96: Cylindrical concrete specimens

4.3.6 Concrete mechanical characterisation

The cylindrical specimens made of same concrete used to realise Beam1 are now tested under compression and tension in order to know the mechanical characteristics of concrete.

4.3.6a Cylindrical Compressive Strength Test

In Compressive Strength Test the specimen is placed vertically between two steel plates, one fixed and the other one movable; the load is applied continuously and uniformly until material rupture and then maximum force applied is recorded; compressive strength is determined by means of a relation between this force and specimen dimensions, then the test is repeated for other three cylinders. The strength value is calculated by averaging the four results; starting from the averaged compressive strength, we can also estimate concrete Young's Modulus.

Specimen	h [mm]	So [mm ²]	ρ [g/cm ³]	F _{max} [kN]	σ _m [N/mm ²]
G1C1	280.0	17586.74	2.4369	1032.91	58.73
G1C2	290.0	17586.74	2.3607	1031.05	58.63
G1C3	288.0	17552.85	2.5022	1047.60	59.68
G1C4	291.0	17577.34	2.3851	987.74	56.19

$$f_{cm} = \frac{58.73 + 58.63 + 59.68 + 56.19}{4} \text{ MPa} = \mathbf{58.31 \text{ MPa}}$$

$$E_{cm} = 22000 \cdot \left(\frac{58.31 \text{ MPa} + 8 \text{ MPa}}{10} \right)^{0.3} = \mathbf{38430 \text{ MPa}}$$



Fig. 97: Compressive strength test

4.3.6b Indirect Tensile Strength Test

This test is able to measure tensile strength of concrete, by means of a diametrical loading across circular cross section. This load application provokes indirectly a perpendicular tensile deformation, which leads to a rupture. The maximum force applied is recorded and so tensile strength is calculated; the same procedure is repeated for other two specimens and then the average is computed.

Specimen	h [mm]	F _{max} [kN]	σ _m [N/mm ²]
G1T1	300.0	329	4.8
G1T2	300.0	330	4.8
G1T3	300.0	-	5.0

$$f_{ctm} = \frac{4.8 + 4.8 + 5.0}{3} MPa = 4.87 MPa$$



Fig. 98: Indirect tensile strength test

4.3.7 Bending test staging

First of all, Beam 1 is positioned upon two steel supports with a clearance of 2.5 meters. Three HBM strain gauges are glued directly on concrete surface following the conventional procedures, two of them on beam's extrados and the third one on intrados: G01C and G02C are placed at a longitudinal distance of 430 mm from the left support, while G03C is exactly at mid-span. These measurements are interesting to have a control over the strain development in three specific points, in order to check the worth of results given by embedded instrumentation.



Fig. 99: Strain gauge installation (G01C)

Each strain gauge used in this experimental campaign needs a dummy resistor to complete the Wheatstone bridge and to compensate the temperature effects: the required number of strain gauge is placed on the faces of some little concrete cubes. They are positioned on polystyrene and protected from sunlight in order to don't have much quicker temperature variations than in the embedded situation. This represents a good calibration for strain gauges on beam's surface, while it is not so proper for ones placed on the bars inside the beam, but this simplification is accepted in the following tests because of their short duration.

All the nine strain gauges (3 on upper reinforcement, 3 on lower reinforcement and 3 on concrete) are connected by cables to the acquisition system, together with respective dummy resistors. The embedded ones are tested to check which instruments still function: four strain gauges (G02, G02, G04 and G05) work correctly, while G01 and G06 must be discarded.

BEAM 1

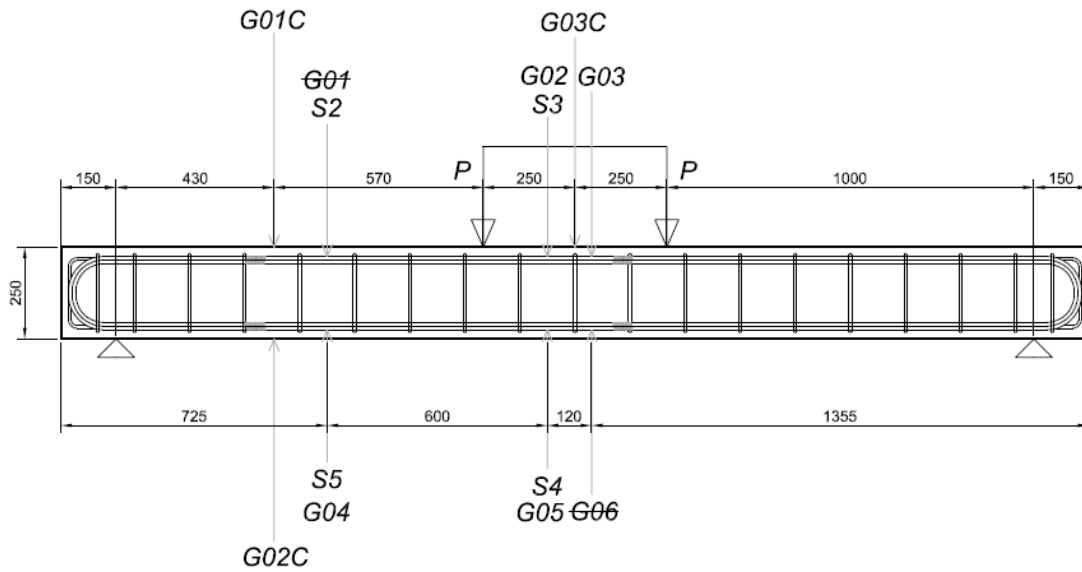


Fig. 100: Complete sensors numeration

Three LVDTs (Linear Variable Differential Transformers) are set to measure displacements in three points of the beam. Two of them are placed upon the beam at the level of supports in order to highlight settlements during the bending test: in those points the vertical displacement should be almost null, otherwise it could mean that a relative shift is arising or that supports are going down for some reasons. The third LVDT is positioned under the mid-span section and it measures the deflection of the beam.



Fig. 101: LVDT installation (LVDT-left)

Each "S3 system" sensor is connected to a Converter Board through its soft PCB: S2 to CB2, S3 to CB3, S4 to CB4 and S5 to CB5. The Converter Boards are set in different ways along the various load cases. In general, Pressure Middle and Temperature Middle are taken as the recorded values just before the daily tests, Pressure Threshold is fixed as ± 1500 Pa and Temperature Threshold as $\pm 2^\circ\text{C}$. Settings are modified in correspondence with last rupture test, when we expect to have large variations of pressure. These four CBs are glued to aluminium strips placed upon the beams without any rigid connection in order to avoid any influence to the RC element behaviour; each Converter Board is linked to the acquisition system by means of two cables, one for pressure data and another one for temperature data.



Fig. 102: S3 system sensors linked to CBs

Two steel cylinders are placed on the beam 250 mm far from the mid-span section, one at the left and the other one at the right: the spacing between them is in total 500 mm and this will represent the constant moment zone. A steel crossbeam HE is arranged upon the two supports; the element is changed with a bigger HE profile just before Load Case 16 in order to avoid buckling problems when high loads are applied. The additional load due to the weight of all the steel elements on the beam is here computed.

$$W, \text{tot1} = 0.133 \text{ kN} + 0.094 \text{ kN} + 0.338 \text{ kN} + 0.139 \text{ kN} + 0.080 \text{ kN} = \mathbf{0.78 \text{ kN}}$$

$$W, \text{tot2} = 0.133 \text{ kN} + 0.094 \text{ kN} + 0.57 \text{ kN} + 0.139 \text{ kN} + 0.112 \text{ kN} = \mathbf{1.05 \text{ kN}}$$

Finally the hydraulic press is positioned upon the mid-span of the element and force F is applied to crossbeam; consequentially two identical reactions $F/2$ burden the RC beam through the steel cylinders. At the end the beam is loaded in a configuration with two supports and two load application points and this is why the test is called 4-points bending test.



Fig. 103: Bending test final configuration

The acquisition system is composed by three HBM Spider8, two connected to Computer 1 and the other one to Computer 2. Force and stroke are data related the hydraulic press; force information cable is linked to both computers in order to obtain contemporary readings. Here below a synthetic scheme is presented.

Channel	Spider8-1 (PC1)	Spider8-2 (PC1)	Spider8-3 (PC2)
CH0	P_S2 [V]	Force [kN]	G02 [$\mu\text{m}/\text{m}$]
CH1	T_S2 [V]	Stroke [mm]	G03 [$\mu\text{m}/\text{m}$]
CH2	P_S3 [V]	LVDT_left [mm]	G04 [$\mu\text{m}/\text{m}$]
CH3	T_S3 [V]	Deflection [mm]	G05 [$\mu\text{m}/\text{m}$]
CH4	P_S4 [V]	LVDT_right [mm]	G01C [$\mu\text{m}/\text{m}$]
CH5	T_S4 [V]	G03C [$\mu\text{m}/\text{m}$]	G02C [$\mu\text{m}/\text{m}$]
CH6	P_S5 [V]	-	Force [kN]
CH7	T_S5 [V]	-	Temperature [$^{\circ}\text{C}$]

4.3.8 Expected moment-curvature behaviour

Since we know the mechanical characteristics of materials, the element geometry and the load application arrangement, we can determine an estimated relation between internal bending moment and curvature in a typical section of the beam. Thanks to simplified theoretical formulations, we calculate three different couples of bending moment and curvature, related to the situations at the end of three linear stages.

The first linear phase starts from origin of moment-curvature graph and it ends at the level of "cracking moment", that happens when the first concrete fibre under tension reaches a tensile stress equal to its tensile strength and the concrete begins to crack. Therefore the second linear stage has a lower slope, because of the reduced stiffness of the section: all the concrete under tension is considered as not contributing anymore. This phase ends when "yielding moment" occurs, so when the steel bars under tension reaches yielding stress; if there are different levels of bars, yielding happens in more than one situation, but as a simplification we consider it when the section presents yielding strain at the level of bar's centre of gravity. Again, the stiffness of the section is reduced and the third curve slope as well: this stage ends with the final point of the curve, that is the failure.

Here below the calculations of these three points are reported. The total section of the smart steel bars is taken into account, without considering the reduction due to the cavities. The geometrical and mechanical properties are written, according to the conventional nomenclature.

4.3.8a Cracking point

$$\begin{aligned} J_{yy} &= \frac{b \cdot h^3}{12} + n \cdot \left[A_{s1} \cdot \left(d - \frac{h}{2} \right)^2 + A_{s2} \cdot \left(\frac{h}{2} - d' \right)^2 \right] = \\ &= \frac{200mm \cdot (250mm)^3}{12} + 5.2 \cdot \left[414.48 mm^2 \cdot \left(215mm - \frac{250mm}{2} \right)^2 + \right. \\ &\quad \left. + 414.48 mm^2 \cdot \left(\frac{250mm}{2} - 35mm \right)^2 \right] = 2.95 \cdot 10^8 mm^4 \\ W_{el} &= \frac{J_{yy} \cdot 2}{h} = \frac{2.95 \cdot 10^8 mm^4 \cdot 2}{250mm} = 2.36 \cdot 10^6 mm^3 \\ \mathbf{M_{cr}} &= f_{ctm} \cdot W_{el} = 4.87 MPa \cdot 2.36 \cdot 10^6 mm^3 \cdot 10^{-6} = \mathbf{11.51 kNm} \end{aligned}$$

$$\chi_{cr} = \frac{M_{cr}}{E_{cm} \cdot J_{yy}} = \frac{11.5 \text{ kNm} \cdot 10^6}{38.43 \text{ GPa} \cdot 2.95 \cdot 10^8 \text{ mm}^4} = \mathbf{1.01 \cdot 10^{-3} \text{ m}^{-1}}$$

4.3.8b Yielding point

$$x = 49.69 \text{ mm}$$

$$\sigma_{s1} = f_{sy} = +530 \text{ MPa}$$

$$\sigma_{s2} = E_{sm} \cdot \varepsilon_{ys} \cdot \frac{x - d'}{d - x} = 200 \text{ GPa} \cdot 0.265\% \cdot \frac{49.69 \text{ mm}}{215 \text{ mm} - 49.69 \text{ mm}} = -47.1 \text{ MPa}$$

$$\varepsilon_c = \varepsilon_{ys} \cdot \frac{x}{d - x} = 0.265\% \cdot \frac{49.69 \text{ mm}}{215 \text{ mm} - 49.69 \text{ mm}} = -0.08\%$$

$$\begin{aligned} N_{compression} &= b \cdot x \cdot f_{cu} \cdot \beta_1 + \sigma_{s2} \cdot A_{s2} = \\ &= -200 \text{ mm} \cdot 49.69 \text{ mm} \cdot 58.31 \text{ MPa} \cdot 0.345 \cdot 10^{-3} + \\ &\quad -47.1 \text{ MPa} \cdot 414.48 \text{ mm}^2 \cdot 10^{-3} = -219.7 \text{ kN} \end{aligned}$$

$$N_{tension} = \sigma_{s1} \cdot A_{s1} = 530 \text{ MPa} \cdot 414.48 \text{ mm}^2 \cdot 10^{-3} = +219.7 \text{ kN}$$

$$N_{internal} = N_{tension} + N_{compression} = 0$$

$$\begin{aligned} M_y &= b \cdot x \cdot f_{cu} \cdot \beta_1 \cdot \left(\frac{h}{2} - \beta_2 \cdot x \right) \\ &\quad + \sigma_{s2} \cdot A_{s2} \cdot \left(\frac{h}{2} - d' \right) + \sigma_{s1} \cdot A_{s1} \cdot \left(d - \frac{h}{2} \right) = \\ &= [200 \text{ mm} \cdot 49.69 \text{ mm} \cdot 58.31 \text{ MPa} \cdot 0.345 \cdot \left(\frac{250 \text{ mm}}{2} - 0.346 \cdot 49.69 \text{ mm} \right) + \\ &\quad + 530 \text{ MPa} \cdot 414.48 \text{ mm}^2 \cdot \left(\frac{250 \text{ mm}}{2} - 35 \text{ mm} \right) + \\ &\quad + 47.1 \text{ MPa} \cdot 414.48 \text{ mm}^2 \cdot \left(215 \text{ mm} - \frac{250 \text{ mm}}{2} \right)] \cdot 10^{-6} = \mathbf{43.10 \text{ kNm}} \end{aligned}$$

$$\chi_y = \frac{\varepsilon_c}{x} = \frac{0.08\%}{49.69 \text{ mm}} = \mathbf{0.016 \text{ m}^{-1}}$$

4.3.8c Failure point

$$x = 29.7 \text{ mm}$$

$$\varepsilon_c = \varepsilon_{cu} = -0.35\%$$

$$\varepsilon_{s1} = \varepsilon_{cu} \cdot \frac{d - x}{x} = 0.35\% \cdot \frac{215\text{mm} - 29.7\text{mm}}{29.7\text{mm}} = +2.18\%$$

$$\sigma_{s1} = f_{sy} + (f_{su} - f_{sy}) \cdot \frac{\varepsilon_{s1} - \varepsilon_{sy}}{\varepsilon_{su} - \varepsilon_{sy}} =$$

$$= 530\text{MPa} + (620\text{MPa} - 530\text{MPa}) \cdot \frac{2.18\% - 0.265\%}{8.0\% - 0.265\%} = 552.32\text{MPa}$$

$$\sigma_{s2} = E_{sm} \cdot \varepsilon_{cu} \cdot \frac{d' - x}{x} = 200\text{GPa} \cdot 0.35\% \cdot \frac{35\text{mm} - 29.7\text{mm}}{29.7\text{mm}} = +124.92\text{MPa}$$

$$N_{compression} = b \cdot x \cdot f_{cu} \cdot \beta_1 =$$

$$= -200\text{mm} \cdot 29.7\text{mm} \cdot 58.31\text{MPa} \cdot 0.81 \cdot 10^{-3} = -280.6\text{ kN}$$

$$N_{tension} = \sigma_{s1} \cdot A_{s1} + \sigma_{s2} \cdot A_{s2} =$$

$$= 552.32\text{MPa} \cdot 414.48\text{mm}^2 \cdot 10^{-3} +$$

$$+ 124.92\text{MPa} \cdot 414.48\text{mm}^2 \cdot 10^{-3} = +280.6\text{ kN}$$

$$N_{internal} = N_{tension} + N_{compression} = 0$$

$$M_f = b \cdot x \cdot f_{cu} \cdot \beta_1 \cdot \left(\frac{h}{2} - \beta_2 \cdot x \right)$$

$$+ \sigma_{s2} \cdot A_{s2} \cdot \left(\frac{h}{2} - d' \right) + \sigma_{s1} \cdot A_{s1} \cdot \left(d - \frac{h}{2} \right) =$$

$$= [200\text{mm} \cdot 29.7\text{mm} \cdot 58.31\text{MPa} \cdot 0.81 \cdot \left(\frac{250\text{mm}}{2} - 0.42 \cdot 29.7\text{mm} \right) +$$

$$+ 552.32\text{MPa} \cdot 414.48\text{mm}^2 \cdot \left(\frac{250\text{mm}}{2} - 35\text{mm} \right) +$$

$$+ 124.92\text{MPa} \cdot 414.48\text{mm}^2 \cdot \left(215\text{mm} - \frac{250\text{mm}}{2} \right)] \cdot 10^{-6} = \mathbf{47.53\text{ kNm}}$$

$$\chi_f = \frac{\varepsilon_{cu}}{x} = \frac{0.35\%}{29.7\text{mm}} = \mathbf{0.118\text{ m}^{-1}}$$

	Moment [kNm]	Curvature [m ⁻¹]
<i>Cracking point</i>	11.51	0.001
<i>Yielding point</i>	43.10	0.016
<i>Failure point</i>	47.53	0.118

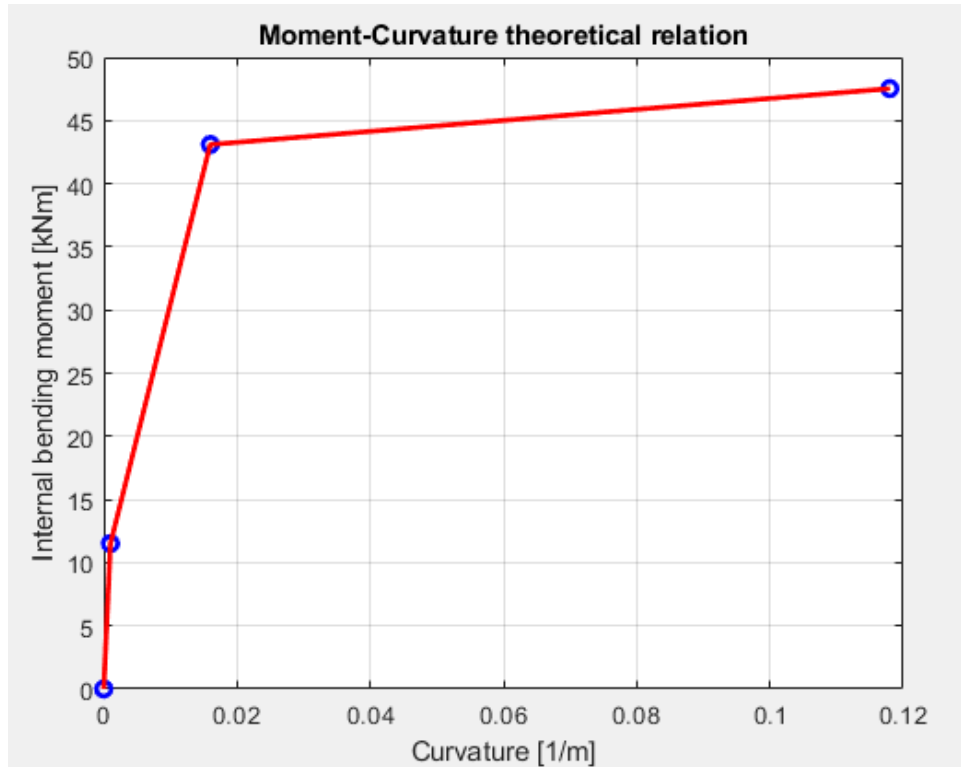


Fig. 104: Moment-Curvature graph

It is possible to estimate which are the theoretical values of force applied by the hydraulic press in order to reach these three points; we should consider also additional bending moment contributions due to the weight of beam and load transfer steel elements. The bending moment under observation is evaluated in mid-span section, but more in general this should be constant for the whole central zone. In yielding and failure points evaluation, the weight of additional steel elements is a little higher, because a bigger crossbeam is used.

	Moment in mid-span [kNm]	Applied Force [kNm]
<i>Cracking point</i>	11.51	20.27
<i>Yielding point</i>	43.10	83.20
<i>Failure point</i>	47.53	92.05

4.3.9 Load cases

We carry out 18 bending tests with different load cases and with progressive maximum force applied. The first 16 tests are conducted under force control, while the last two are under displacement control in order to reach failure point, allowing the detection of post-peak behaviour. The beam reaches failure point, when the fracture is formed in a section next to mid-span in correspondence with

a load of 88.45 kN. Therefore maximum load applied is around 4% below the estimated value (92.05 kN) and it is reasonable, because the difference stands within the variability range of materials characteristics.

Test	Control	Max. Load [kN]	Loading Velocity	Frequency [Hz]
1	Force	6	1 kN/min	5
2	Force	12	4 kN/min	5
3	Force	12	12 kN/min	25
4	Force	12	12 kN/min	25
5	Force	18	9 kN/min	5
6	Force	18	18 kN/min	5
7	Force	18	36 kN/min	5
8	Force	25	5 kN/min	5
9	Force	25	5 kN/min	5
10	Force	25	5 kN/min	5
11	Force	25	1 kN/min	5
12	Force	35	5 kN/min	25
13	Force	40	5 kN/min	25
14	Force	45	5 kN/min	25
15	Force	55	5 kN/min	25
16	Force	65	5 kN/min	25
17	Displacement	75.40	1.5 mm/min	25
18	Displacement	88.45	1.5 mm/min	25



Fig. 105: Fracture - Test 18 - Collapse (Max. Load: 88.45 kN)



Fig. 106: Fracture detail - Test 18 - Collapse (Max. Load: 88.45 kN)

4.3.10 Crack pattern

During the bending tests with different loads applied, I take note of cracks development in the beam and here below there are drawings representing the progressive cracked transversal sections, as they appear from East side. Before that the first starts, a shrinkage-induced crack is noticed next to the middle of the beam; then this becomes a real crack due to bending when the load is applied.

Cracking of this reinforced concrete element starts firstly at the middle span, where the bending moment is maximum; the cracks start to appear at the bottom of the section, where the concrete is under tension and then they run vertically, while the tensile stresses are intensifying and the neutral axis is moving higher.

The formation of cracks happens symmetrically in relation to the centre of the beam and they occur in correspondence with stirrups' position. At the end of final bending test, the failure is reached and a big fracture appears; this should stand theoretically at the middle span, because the beam has a symmetrical geometry and it is symmetrically loaded. Actually the fracture is shifted to the left and this could be due to the fact that left part is a little weaker than the right one.

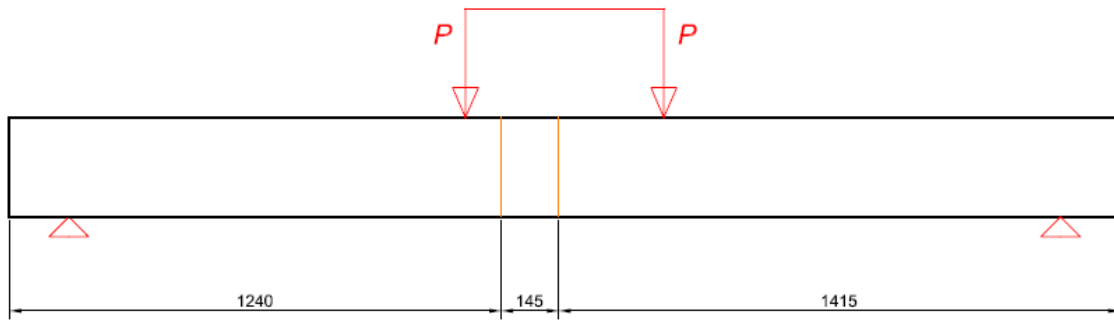


Fig. 107: Crack pattern - Test 5 (Max. Load: 18 kN)

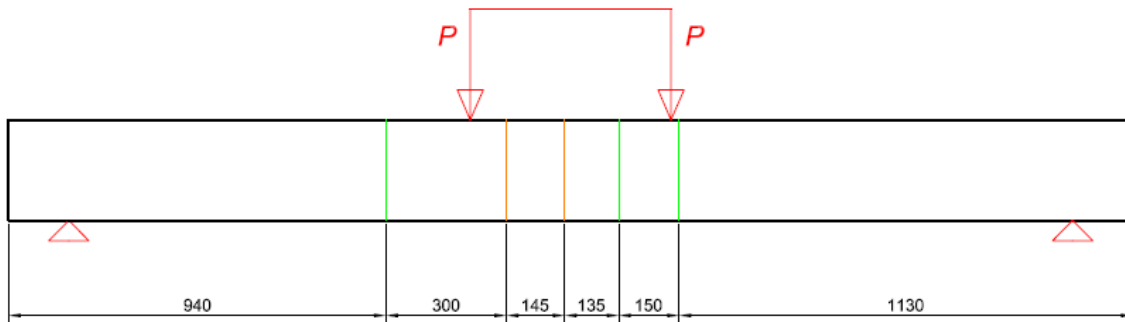


Fig. 108: Crack pattern - Test 8 (Max. Load: 25 kN)

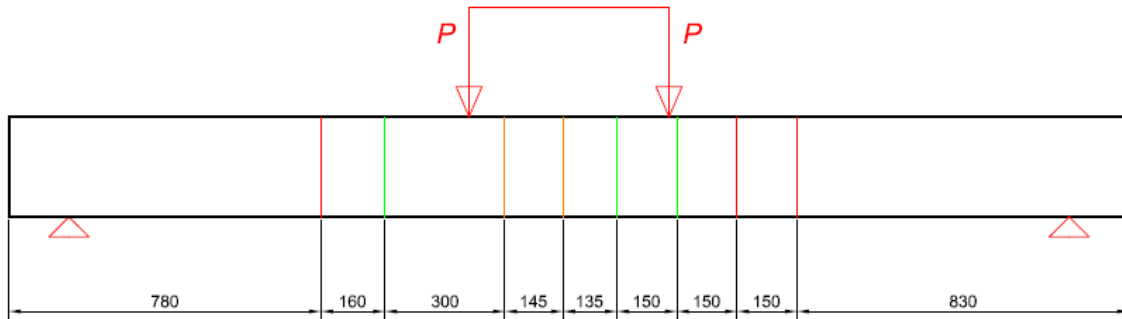


Fig. 109: Crack pattern - Test 12 (Max. Load: 35 kN)

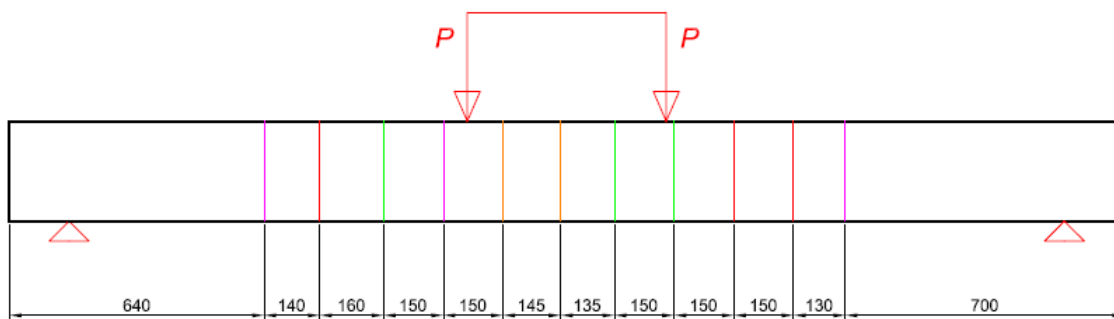


Fig. 110: Crack pattern - Test 14 (Max. Load: 45 kN)

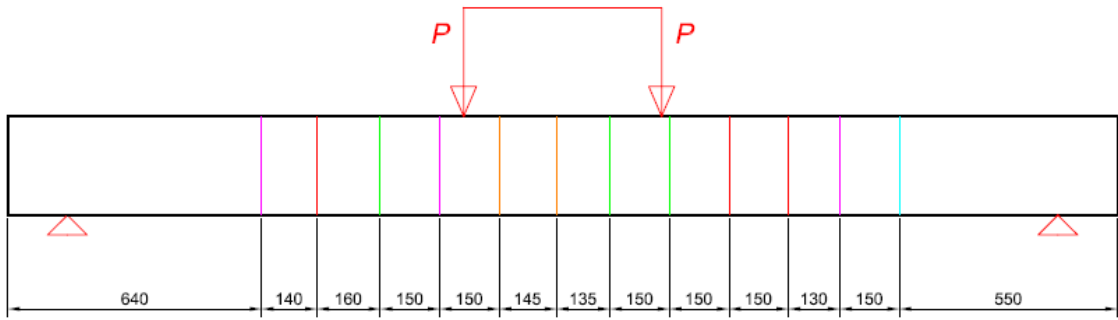


Fig. 111: Crack pattern - Test 15 (Max. Load: 55 kN)

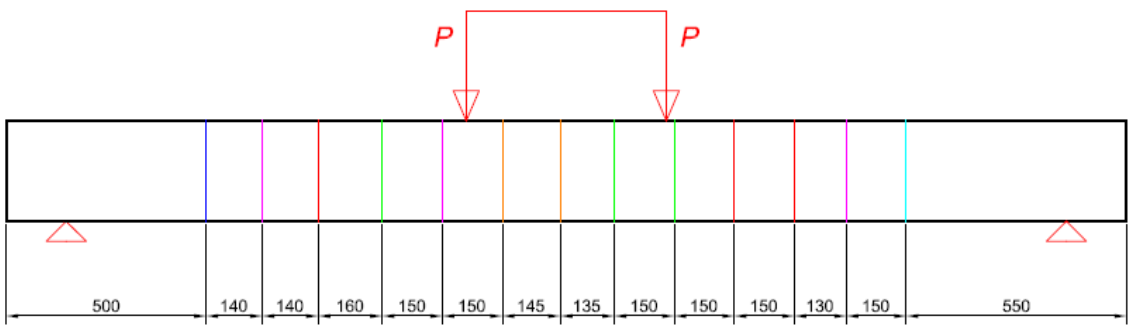


Fig. 112: Crack pattern - Test 16 (Max. Load: 65 kN)

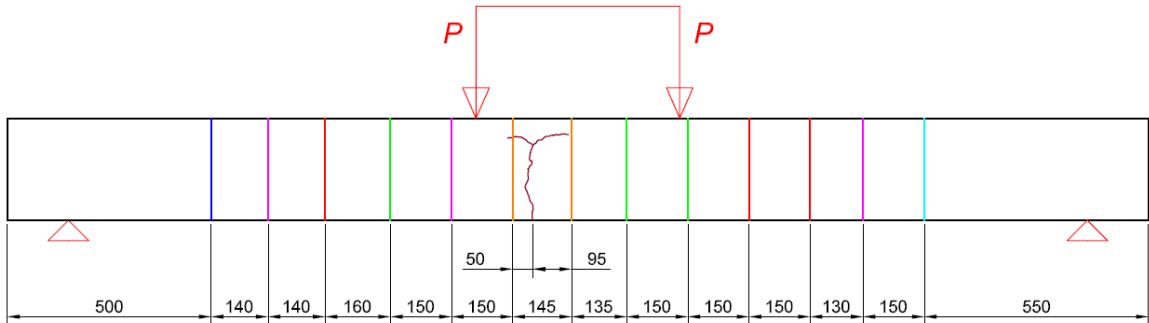


Fig. 113: Crack pattern - Test 18 - Collapse (Max. Load: 88.45 kN)

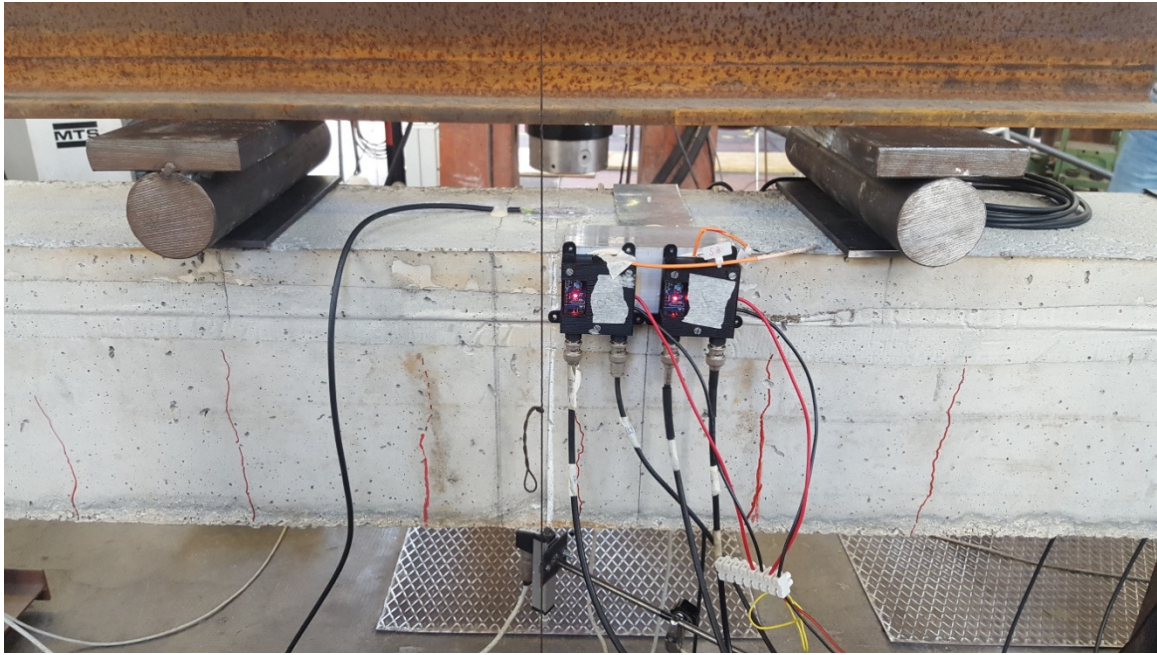


Fig. 114: Crack pattern picture - Test 8 (Max. Load: 25 kN)



Fig. 115: Crack pattern picture - Test 9 (Max. Load: 25 kN)



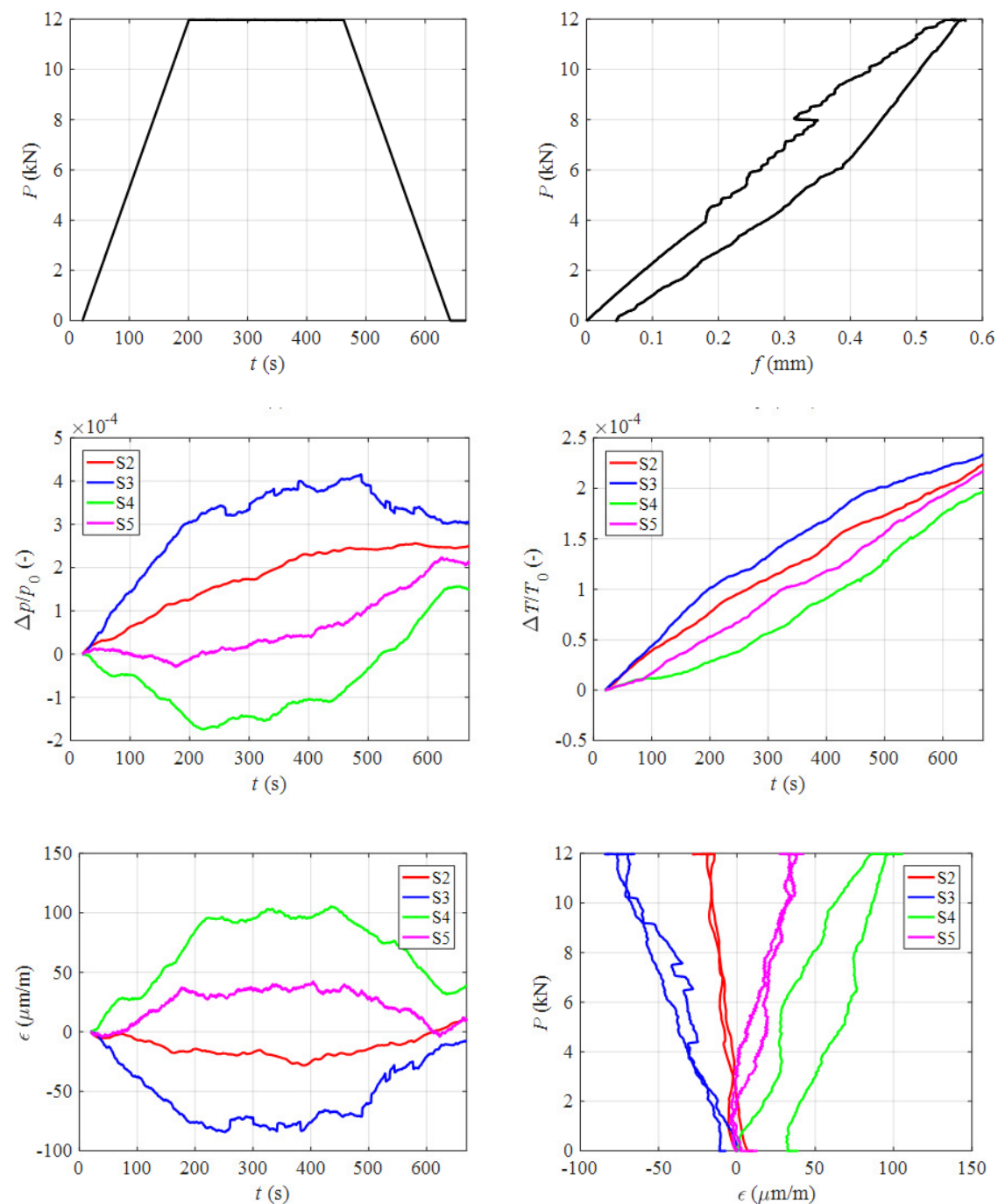
Fig. 116: Crack pattern picture - Test 15 (Max. Load: 55 kN)

4.3.11 Results and discussion

The results of load cycle tests n° 02 - 12 - 17 are respectively presented in the following figures, to exemplify the cases of low, medium and high load levels. Denoting by P the applied load on the beam and by f the deflection measured at the mid-span of the beam (subtracted the average deflections at the bearings), each figure orderly reports: (a) the time history of applied load, (b) the beam load-deflection curve, (c) the time history of S3 system's measured pressure, (d) the time history of S3 system's measured temperature, (e) the time history of S3 system's estimated strain, (f) the S3 system's estimated load-strain curves, (g) the time history of strain gauges' measured strain, (h) the strain gauges' measured load-strain curves. For better clarity, in all figures deflections and strains are reset to zero at the beginning of each new cycle. Also, in all figures the co-located pairs of S3 system and G (strain gauge) sensors are plotted in the same colour. Only exception are sensors $S3$ and $G03$, both plotted in red although located in different beam sections. Observing the three figures, a satisfactory performance of the S3 sensors is apparent, demonstrated by the acceptable matching between the S3 estimations and G measurements at all load levels.

Test 02: at the lower load level ($12 \text{ kN} + 0.78 \text{ kN} + \text{beam's self-weight}$), S3 sensors appear to be disturbed by noise, which makes their strain estimations less stable than the strain measurements acquired by the G sensors. However, the trends are clearly the same, and also the absolute values are in close agreement,

especially considering that the S3 estimated ϵ is conventionally referred to the bar gross section and therefore is certainly underestimated with respect to the strain occurring at the cavity location. The maximum strain, stress and force variations in the inferior bar around mid-span are approximately: $\epsilon = 100 \mu\text{m/m}$; $\sigma = 20 \text{ MPa}$; $F = 6.3 \text{ kN}$. At this low load level (in which every bar is still within the linear elastic range) the noise in S3 measurements is anyway not a significant drawback. Despite this low load level, both S3 and G clearly show the cyclic hysteresis of the load-strain curves at *S4* and *G05* (inferior bar - next to mid-span section), due to incipient cracking.



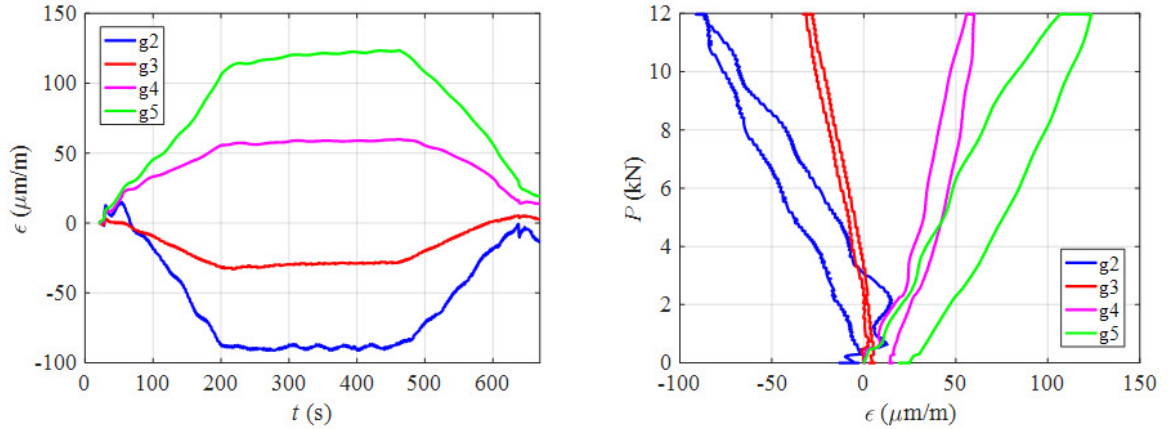
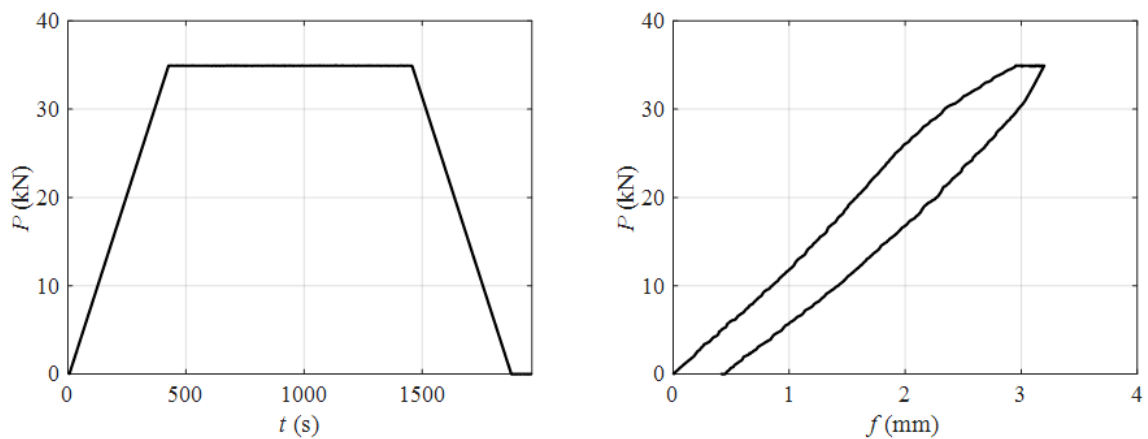


Fig. 117: Load cycle 02: (a) applied load; (b) load-deflection curve; (c) S3 measured pressure; (d) S3 measured temperature; (e) S3 strain; (f) S3 load-strain curves; (g) G strain; (h) G load-strain curves. (Tondolo, 2018)

Test 12: at the medium load level ($35 \text{ kN} + 0.78 \text{ kN} + \text{beam's self-weight}$) the effects of noise on S3 strain estimations is nearly negligible. A good matching is again observed between S3 and G results. The maximum strain, stress and force variations in the inferior bar around mid-span are approximately: $\epsilon = 620 \text{ } \mu\text{m/m}$; $\sigma = 124 \text{ MPa}$; $F = 39 \text{ kN}$. These values still correspond to a bar in its fully elastic range. A significant hysteresis is again observed at the location of *S4* and *G05* (inferior bar - next to mid-span section), but even greater is the hysteresis observed at the location of *S5* and *G04* (inferior bar - aside), due to cracking propagation towards the bearings. Indeed, the cracking opening around *S5* is clearly visible in figure below at approximately $t = 400 \text{ s}$.



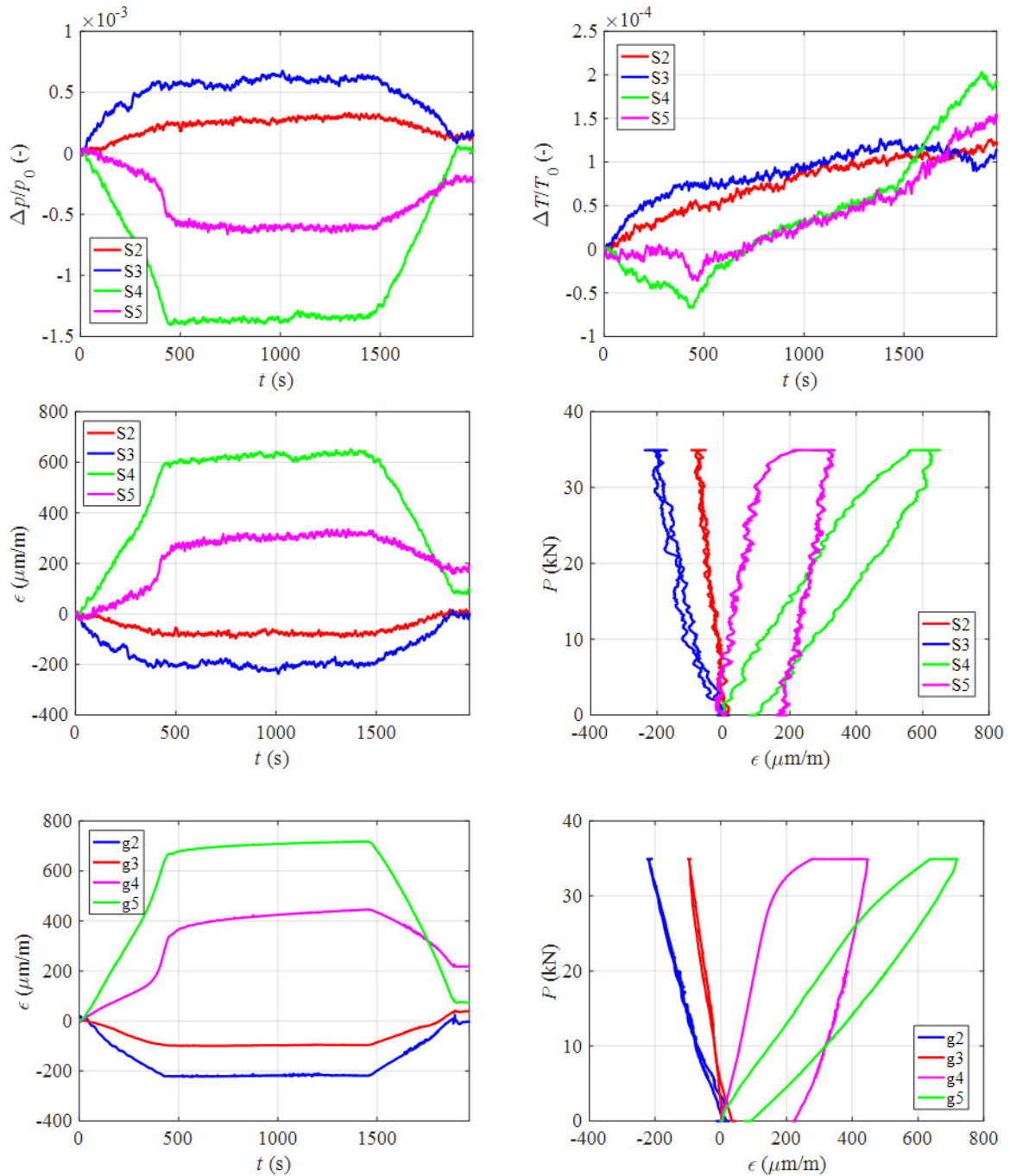
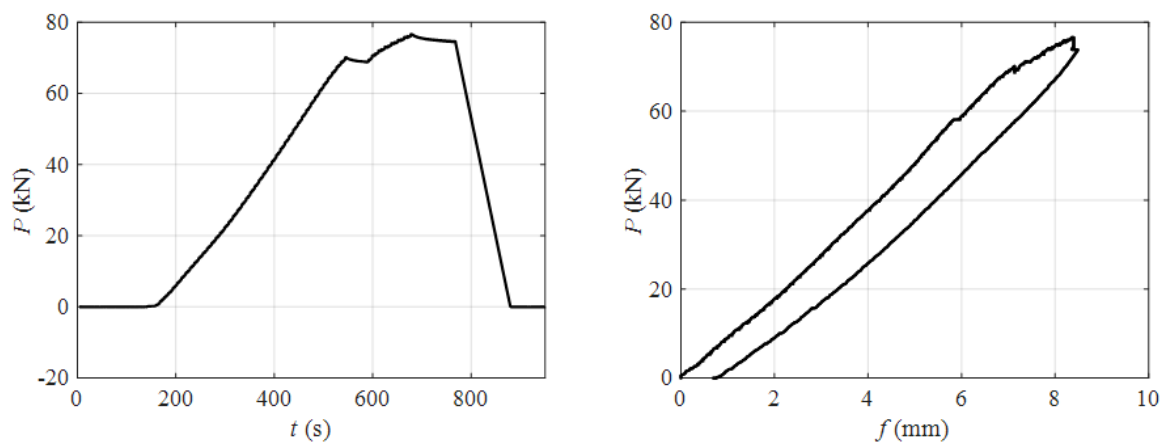


Fig. 118: Load cycle 12: (a) applied load; (b) load-deflection curve; (c) S3 measured pressure; (d) S3 measured temperature; (e) S3 strain; (f) S3 load-strain curves; (g) G strain; (h) G load-strain curves. (Tondolo, 2018)

Test 17: at the higher load level (75.4 kN + 1.05 kN + beam's self-weight), the effects of noise on S3 strain estimations are decisively negligible. The maximum strain variation estimated by $S4$ is around 12700 $\mu\text{m}/\text{m}$. If the bar were locally in its linear elastic range, this would correspond to $\sigma = 2540$ MPa and $F = 798$ kN. These disproportionately high values of stress and force indicate that the bar around the cavity has undergone large plastic deformations. This is also clearly shown in figures (f) and (h), where the load-strain curves of both $S4$ and $G05$

show a significant hysteresis. Noticeably, however, the strains estimated by *S4* are much larger than those measured by G05. This indicates that the plastic deformations occurring around the cavity have a much larger influence on the cavity volume variation than on the strains measured at the bar surface on a reference length of 8 mm; it's also important to notice that two electrical strain gauges - one for both the sides of the bar - should be provided to determine an averaged value of strain, which could be more correct to describe the effective deformation in the holed section.

Clearly, in the presence of so large plastic deformations, the same concept of equivalent strains around the cavity loses any practical meaning. At the location of *S5* and *G4* (inferior bar - aside), the maximum strain variation estimated by *S5* is around 1120 $\mu\text{m}/\text{m}$. If the bar were locally in its linear elastic range, this would correspond to $\sigma = 224 \text{ MPa}$ and $F = 70 \text{ kN}$. In the previous study (Tondolo, 2018), the divergence from linearity for a bar equipped with S3 sensors was observed around 50 kN. It can be concluded that during this load cycle some limited local plastic deformations are likely to have occurred around the *S5* cavity as well. Their hysteretic effect on the load-strain curves in figures (f) and (h) is however limited. The overall effect of the plastic deformation around the *S4* cavity on the beam load-deflection curve (b) is not very significant, because of their local character. The local weakness of the instrumented bar evidently results in a scarce ductility of the bar itself and finally of the beam. An additional rib will be necessary to reduce this effect.



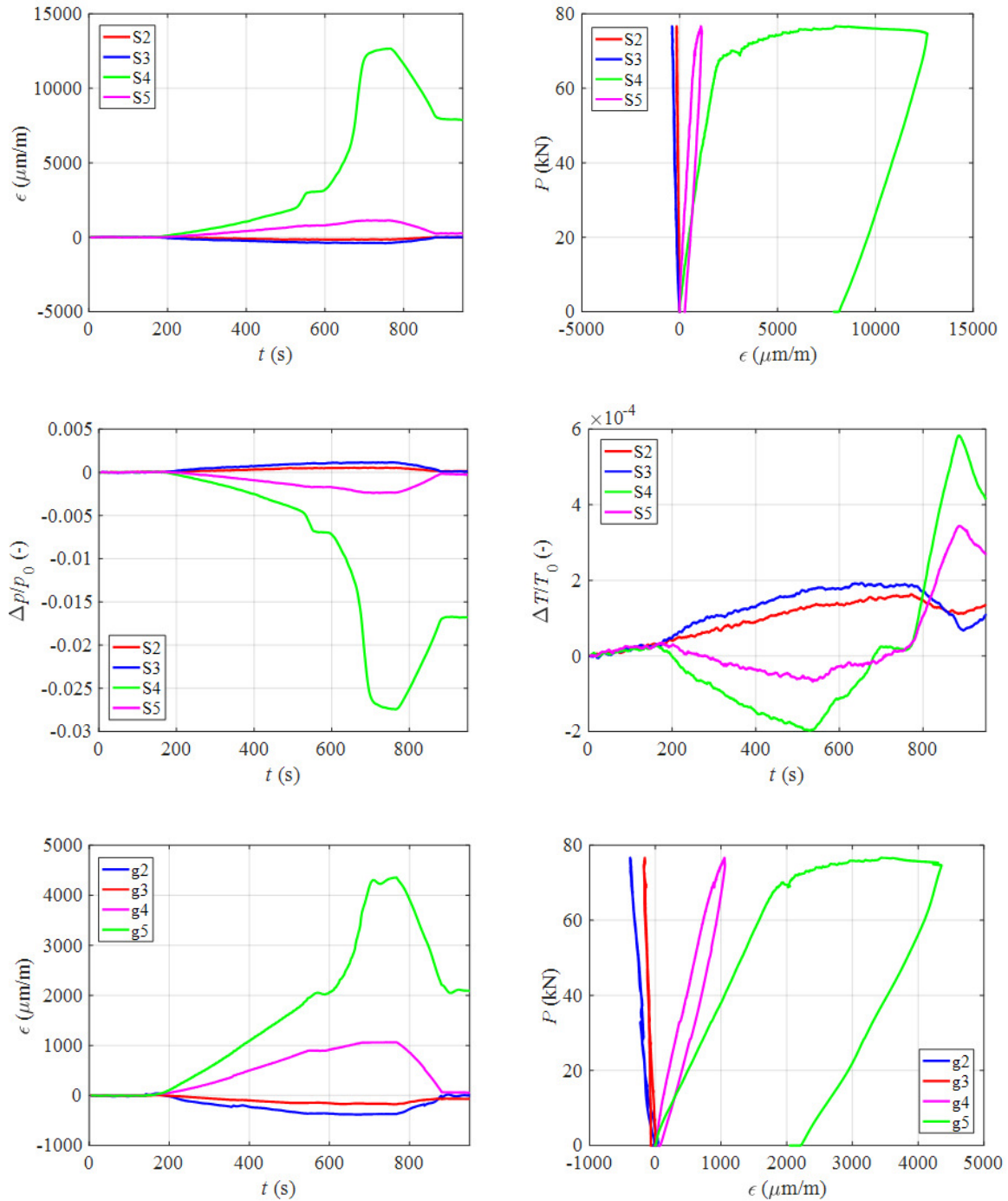


Fig. 119: Load cycle 17: (a) applied load; (b) load-deflection curve; (c) S3 measured pressure; (d) S3 measured temperature; (e) S3 strain; (f) S3 load-strain curves; (g) G strain; (h) G load-strain curves.(Tondolo, 2018)

Test 18: the results of the last load cycle test are here presented. This is the load cycle, conducted under displacement control, which leads to the beam collapse. Figures (a) and (b) show the applied load times history and the beam load-deflection curve. The P - f relation appears nearly linear until P reaches the maximum value of the previous cycle (at approximately $t = 425$ s), then an approximately linear strain hardening branch begins, which leads to the ultimate

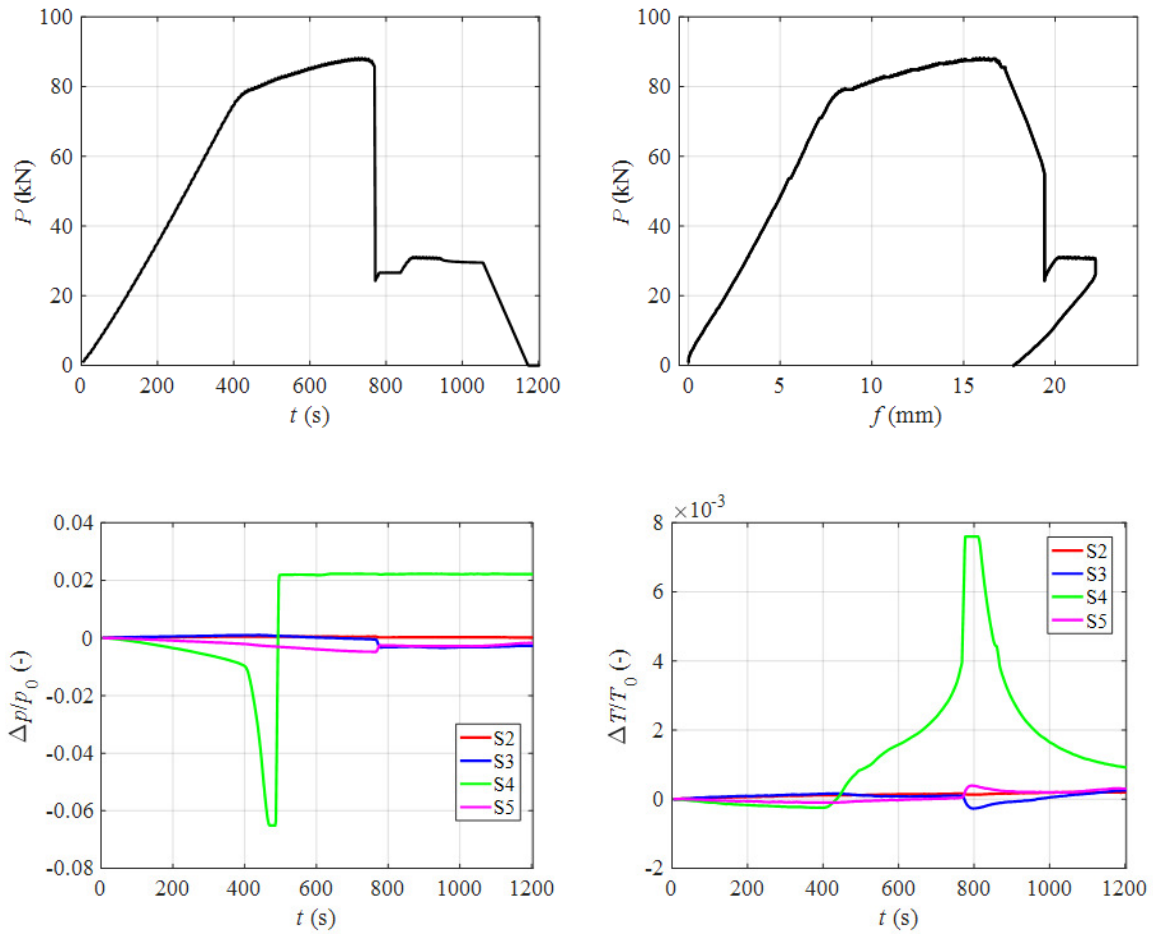
load $P_u = 88.45$ kN and, after a short post-peak branch, to the sudden collapse of the instrumented bar, occurring at $t = 770$ s. This collapse instantaneously reduces the load bearing capacity of the beam to 24.3 kN, i.e. in a nearly exact proportion to the reduction of the total effective area of the transversal section of the steel bars in tension. The subsequent hardening branch testifies the residual strength capacity of the two $\Phi 8$ bars in the tension. The load is finally removed before reaching the collapse of these bars too.

Observing the evolution of p and T variations in the S3 sensors (figures c and d) and the corresponding estimations of ε (figures e to h), the following observations can be done. The $S4$ sensor opens (i.e. the cavity ceases to be hermetically closed, as it clearly appears from the p time history in figure a) at $t = 492$ s, before the bar collapse, because of the large plastic strains accumulated around the hole. From this instant on, although the $S4$ sensor still works, its strain estimations have no physical meaning (dashed lines in figures e and f). $S4$ opening is preceded by very large ε estimations (figure e), due to the large inelastic behaviour of the steel around the cavity (figure f). This is particularly evident after $t = 425$ s (figure e), that is when ε coincides with the maximum value reached in the previous load cycle. After $t = 400$ s, the energy dissipation produced by the large plastic deformations around the cavity is also responsible for a rapid temperature increase of the cavity (figure d), which will continue even after the cavity opening and until the bar collapse ($t = 770$ s).

The other three S3 system sensors are effective all through the test. Before the bar collapse, $S5$ has already experienced local plastic deformations, particularly after $t = 425$ s (strain level of the previous load cycle), while $S2$ and $S3$ are still in the elastic range. Interestingly, after $t = 420$ s, the $S3$ sensor, initially compressed, experiences a progressive strain increase (in sign) until working in tension. This occurs because, as cracking in the mid beam section increases, the neutral axis progressively rises and eventually exceeds the position of the superior bar where the $S3$ sensor is embedded. At collapse ($t = 770$ s), $S5$ and $S2$ sense the stress drop due to the sudden load reduction, while $S3$ further increases its tension as the neutral axis further rises.

The same qualitative trends can be recognized in the strain measurements provided by the G sensors (figures i and j). In quantitative terms, as already observed when commenting the previous load cycle, the G strains tend to appear smaller than the S3 strains when large local plastic deformation occur, but this

seems not to be the case for the pair *S3-g2*. Significantly, two of the four G sensors fail during loading (dashed linear in figures i and j): *G5* fails at $t = 425$ s, even before the failure of the co-located *S4* sensor; and *G3* fails at the bar collapse ($t = 770$ s). It can be concluded that, of the six strain gages initially installed on the bars, only two are still working at the end of the experimental campaign, while only one of all the four *S3* system sensors reaches failure, because of excessive stress.



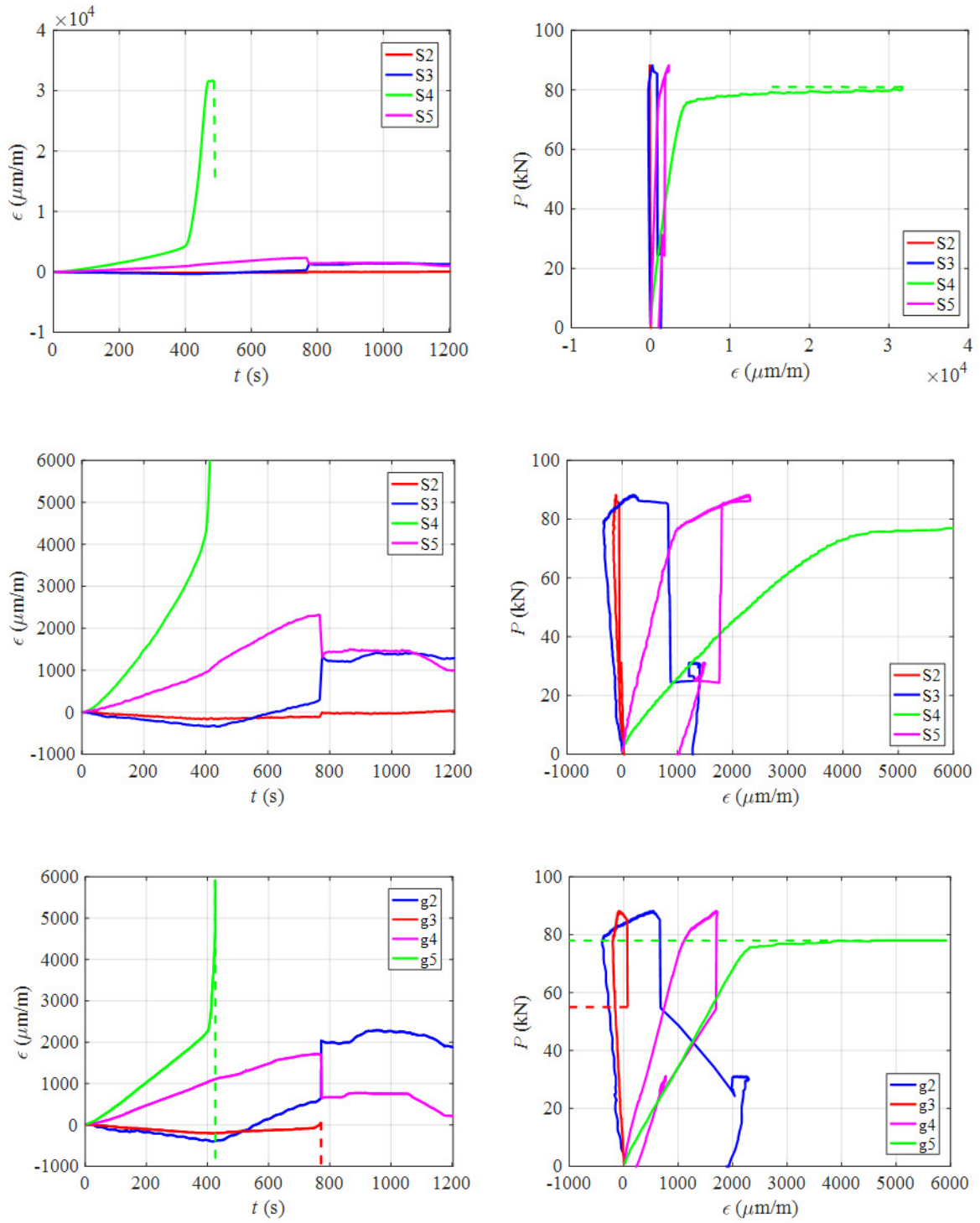


Fig. 120: Load cycle 18: (a) applied load; (b) load-deflection curve; (c) S3 measured pressure; (d) S3 measured temperature; (e) S3 strain (full view); (f) S3 load-strain curves (full view); (g) S3 strain (zoomed view); (h) S3 load-strain curves (zoomed view); (i) G strain; (j) G load-strain curves. (Tondolo, 2018)

Conclusions

"S3 system" appears to be a valid *strain sensing smart technology*, which could be used for Structural Health Monitoring applications in the next future. In this paper, numerical studies and experimental tests are carried out in order to step forward in its development. Here some conclusive thoughts are briefly expressed.

After having realised a satisfying FEM model of the smart steel bar, a sensitivity analysis is performed by defining some different constitutive laws. The results show that the numerical model is capable to describe in a good way the elastic behaviour and the yielding of a smart steel bar, as shown in the force-displacement graph. On the other side, the whole plastic branch is not detected and it means that the model reaches failure before it should actually do. The constitutive law describes a global behaviour, but probably it is not effective in the description of the local behaviour. A solution to this issue is the definition of higher maximum strains, as done in sensitivity analysis. Under this hypothesis, FEM analysis stops at larger strain levels, even though there are still differences in the slope of the plastic branch.

Moreover, the numerical model needs to be improved in order to simulate properly strain sensing in air cavity by means of pressure variations readings. The current model provides a correct shape of the curve in the force-deformation graph, but the elastic slope is still higher than experimental one. It is also possible to correct volumetric deformations through a coefficient, which allows to take into account the presence of additional non-deformable material inside the cavity: this brings to reduce the slope, obtaining numerical results more similar to reality.

Then, a first application of S3 system is performed in a typical civil engineering situation, a RC beam subject to bending. A good matching between smart and traditional strain measurements is highlighted until the bar under tension works completely with an elastic behaviour: this is a very important result, which confirms the validity of this innovative technology for SHM purposes, at least within elastic range of steel. Furthermore, noise affecting measurements at low load level becomes negligible for higher load levels.

The smart steel bars are previously tested under axial tension within their elastic range in order to realise a mechanical characterisation. The force passing through the bar can be determined thanks to the linear relation with the calculated volumetric deformation of air cavity: this is not possible anymore, when steel begins to yield. At the high load test, sensor *S4* reads a big increase of volumetric deformation in correspondence with the plasticisation of the zone around the cavity and since then the results are meaningless, because they are not able to describe effectively the state of strain inside the bar.

Sensor *S4* reaches failure only during the last bending test at very high load levels applied, when the sealing breaks and MEMS transducer is not sensing anymore the pressure variations of air contained inside the cavity. This is the only sensor which didn't survive to the bending test, while all the other three S3 system still work after beam's failure, even if zone around *S5* cavity is plasticized too. Strain gauges instead are not so durable, because only two of the initial six instruments still work at the end of the experimental campaign. Therefore S3 systems is not only a low cost technology, but it also seems to be robust.

At the end, we can state that S3 system is a smart technology which needs certainly some further developments, but it has the potential to become in all respects an important tool for Structural Health Monitoring applications, thanks to features like strain sensing, ease of installation, durability and low cost.

Bibliography

Abdo Mohamed Abdel-Basset Structural Health Monitoring, History, Applications and Future. A Review Book [Book]. - 2014.

Chen Lao Sensitivity modelling of a strain-sensing antenna [Journal]. - 2017.

DeRosa Danielle Fiber Optic Sensors and Digital Image Correlation for Measuring Deformations in Reinforced Concrete Beams [Journal]. - 2013.

FBGS <https://www.fbgs.com/technology/fbg-principle/> [Online]. - 2018.

Galindez-Jamiy C. A. Brillouin Distributed Fiber Sensors: An Overview and Applications [Journal]. - 2012.

Güemes Alfredo Fiber Distributed Sensing - Physical Principles and Applications [Journal]. - 2010.

López-Higuera J.M. Fiber optics in Structural Health Monitoring [Journal]. - 2014.

Loupos Konstantinos Structural health monitoring system for bridges based on skin-like sensor [Journal]. - 2017.

Marr Allen Cambridge Centre for Smart Infrastructure and Construction Distinguished Lecture [Conference]. - 2017.

National Instruments <http://www.ni.com/white-paper/3642/en/> [Online]. - 2018.

Park Jinwoo Dynamic fiber Bragg grating strain sensor interrogation with real-time measurement [Journal]. - 2017.

Pepakayala Venkatram Passive Wireless Strain Sensors using Microfabricated Magnetoelastic Beam Elements [Journal]. - 2014.

Rocha Pinto Portela Nunes Marina Fatigue Behaviour of Steel Reinforcement Bars at Very High Number of Cycles [Journal]. - 2014.

Soga Kenichi Understanding the real performance of geotechnical structures using an innovative fibre optic distributed strain measurement technology [Journal]. - 2014.

Spencer B. F. Development of high-sensitivity wireless strain sensor for structural health monitoring [Journal]. - 2013.

Spencer B. F. Next Generation Wireless Smart Sensors Toward Sustainable Civil Infrastructure [Journal]. - 2016.

Tondolo Francesco Embedded system for measurements of strain/stress in one-dimensional elements [Patent]. - 2016.

Tondolo Francesco Experimental test on an RC beam equipped with embedded barometric pressure sensors for strains measurement [Journal]. - 2018.

Tondolo Francesco Smart reinforcement steel bars with low-cost MEMS sensors for the structural health monitoring of RC structures [Journal]. - 2018.

Windl Roman Passive wireless strain measurement based upon the Villari effect and giant magnetoresistance [Journal]. - 2016.

Zhang Hailiang Highly sensitive strain sensor based on helical structure combined with Mach-Zehnder interferometer in multicore fiber [Journal]. - 2017.